Univerzita Karlova v Praze
Matematicko-fyzikální fakulta

DIPLOMOVÁ PRÁCE

Lucie Szabová

"Ab initio" studium rozhraní Cu-Ce-O

Katedra fyziky povrchů a plazmatu

Vedoucí diplomové práce: Prof. RNDr. Vladimír Matolín, DrSc.
Konzultant: Dr. Stefano Fabris

Studijní program: Fyzika povrchů a ionizovaných prostředí

2009

First of all I am very gratefull to my advisor **Dr. Stefano Fabris** for the effort he gave to teach me to work with pwscf code and understand the results, for his patience with my frequent questions, for willingness to help me whenever I needed and for allowing me to work with him in Trieste.

I want to thank my supervisor **Prof. RNDr. Vladimír Matolín, DrSc.** for a great opportunity he gave me and for helping with any problems.

I also want to thank to Dr. Matteo Farnesi who helped me much during my stays in Italy both with computation and understanding many issues.

I also want to thank my friends, among who I would like to name Pavol Jusko, who helped me with work in unix environment, Tatiana Zahoranová, who helped me understand many things in the field of experiments and Ľubica Valentová who gave me many helpful advice on various topics.

I appreciate my parents' support during my studies and I thank to my sister Lenka Szabová, who helped me with many graphical issues in this thesis.

The start of this work would have been much harder if it wasn't for support from the Project HPC-EUROPA (RII3-CT-2003-506079), with the support of the European Community - Research Infrastructure Action under the FP6 "Structuring the European Research Area" Programme. I would also like to thank to the physical department of UJEP for letting me use the computer cluster Enputron for calculations. Additional computer time was provided by the International School for Advanced Studies and DEMOCRITOS National Simulation Center in Italy.

Prohlašuji, že jsem svou bakalářskou práci napsala samostatně a výhradně s použitím citovaných pramenů. Souhlasím se zapůjčováním práce a jejím zveřejňováním.

V Praze dne 25. 8. 2009 Lucie Szabová

Contents

Název práce: "Ab initio" studium rozhraní Cu-Ce-O
Autor: Lucie Szabová
Katedra (ústav): Katedra fyziky povrchů a plazmatu
Vedoucí bakalářské práce: Prof. RNDr. Vladimír Matolín, DrSc.
e-mail vedoucího: matolin@mbox.troja.mff.cuni.cz

Abstrakt: Předložená práce zkoumá prostřednictvím metody DFT+U strukturální a elektronické vlastnosti modelového systému Cu/CeO_2, důležitého pro heterogenní katalýzu. Zejména je zkoumána interakce mezi měděnými nanočásticemi na površích CeO_2. Systémy jsou modelované pomocí rozhraní $Cu(111)/CeO_2(111)$ a adsorpce měděného atomu na povrchu CeO_2. V práci je ukázáno, že v přítomnosti mědi ať už v podobě adatomu, tenké vrstvy nebo tlusté vrstvy dochází v důsledku přenosu náboje z kovu do oxidu k redukci cerových iontů. Redukce oxidů ceru hraje při katalýze významnou roli, proto z předpovědi redukce očekáváme, že Cu/CeO_2 systémy budou mít důležité aplikace v katalytických technologiích.
Klíčová slova: DFT, heterogenní katalýza, rozhraní kov/oxid, elektronová struktura, fyzika povrchů

Title: "Ab initio" study of interface Cu-Ce-O
Author: Lucie Szabová
Department: Department of Surface and Plasma Science
Supervisor: Prof. RNDr. Vladimír Matolín, DrSc.
Supervisor's e-mail address: matolin@mbox.troja.mff.cuni.cz

Abstract: The present work is a theoretical analysis based on the numerical DFT+U simulations investigating the structural and electronic properties of Cu/CeO_2 model systems, which have important applications as heterogeneous catalysts for environment protection and energy sources. We provide a detailed insight into the cohesion of the interface between metal Cu nanoparticles supported on CeO_2 substrates. This issue is analyzed both in context of small supported Cu clusters as well as for the extended interface underneath Cu nanoparticles on ceria surfaces. These cases were modelled with a $Cu(111)/CeO_2(111)$ interface and with a Cu adatom adsorbed at the oxidized and reduced $CeO_2(111)$ surface, respectively. The thesis provides a direct correlation between the cohesive and electronic properties mediated by the charge transfer process.

The reduction of surface cerium atoms in the presence of copper either in form of adatom, thin copper layer or a slab of copper is predicted to result from charge transferred from the metal. Since cerium reduction is suggested to play an important role into the catalytic activity of ceria-based catalysts, by predicting the reduction of cerium ions in the presence of copper it can be expected that Cu/CeO_2 systems will have important applications in catalytic technology.
Keywords: DFT, heterogeneous catalysts, metal/oxide interface, surface science, electronic structure

Chapter 1

Introduction

In the present time, the protection of the environment and finding new sources of energy are of the most importance. Both of these problems are connected with development of new and better catalysts. Catalysts are chemical substances usually added to some reaction in order to modify the rate of the reaction. The increase of the rate often occurs via providing an alternative mechanism for the reaction combined with a different transition state having a smaller activation energy. Another important fact is the stability of the catalyst that should not be consumed during the reaction, neither lose its activity. Catalysed reactions are important in many aspects of environmental science as for example in catalytic converters for exhausts in automobiles, gas sensors or dynamics of the ozone hole. In general, most frequently used catalysts are transition metals and transition metal compounds, zeolites, platinum metals or H^+.

Catalysis occurs in two types: homogeneous catalysis, where the catalyst and the reactants are in the same phase, and the heterogeneous catalysis, where the catalyst is in a different phase than the reactants. Some of the most efficient catalysts are of the heterogeneous type, composed of metal particles deposited on oxide supports. The activity of the catalyst can be influenced by the choice of the support and the metal as well as the size of the metal clusters or the morphology of the support. This complexity is reflected in the difficulty in achieving a controlled synthesis of these systems, as well as in getting a detailed understanding at the atomic level.

In the present work we focus on the heterogeneous catalysts composed of Cu supported by cerium oxide (CeO_2, or ceria) surfaces. The general goal is revealing the most relevant structural and electronic properties of these systems which control their reactivity. We will do this by the means of state-of-the-art ab-initio computer modeling of materials.

1.1 The scientific background

Experiment

Ceria (CeO_2) is well known for its useful properties such as high refractive index, good transmission and adhesion and high stability [1]. It is important in silicon-on-insulator structures, small stable capacitor devices (RAM), fuel cells

or in oxygen sensors. With its significant oxygen storage and release capability ceria proves usefully as a catalyst for several reactions such as CO oxidation or NO reduction. In the present day the question of environment protection is very important, so the application of ceria as automotive exhaust catalyst to reduce air pollution is desirable [2, 1].

Experiments and calculations show, that the most stable surface of ceria is $CeO_2(111)$. Catalytic ability of ceria can be enhanced by adding metal dopants. Model systems consisting of thin films of CeO_2 and various metals were used to study their catalytic properties. Amongst others ceria on Pt(111) [3, 4], Re(0001) [1], Au(111) [5] or Cu(111) [6, 7, 8, 9] systems were examined. It was found, that just a small amount of Cu significantly increases catalytic properties of ceria [10, 11, 12, 13, 14, 15, 16]. Several experiments were conducted to investigate the mechanism of the reaction between copper and ceria.

In particular in Ref. [7] the valence band states of copper loaded ceria powder consisting of submicrometer ceria particles covered with thin copper film were studied by the means of XPS and SRPES in order to determine its catalytic properties. The inverse model system consisting of 2 monolayers of ceria grown on copper crystal with (111) plane on top was used to study the interactions at the interface. It was shown, that in the presence of copper, ceria powder is partially reduced [17]. In Ref. [18] partial reduction of CeO_2 (111) surface was shown as well. As a result of the conducted experiments the following explanation was suggested, requiring confirmation by the future theoretical calculations: the existence of the covalent Cu-Ce bond at the interface was proposed to explain the observed metallic states, the creation of the oxygen terminated Cu/CeO_2 interface after annealing of the system was suggested accompanied by the formation of the Cu-Ce-O mixed oxide, and finally the discovered enhancement of the catalytic ability on the CO oxidation of ceria system after adding copper was proposed to be induced by the presence of the Ce^{3+} states which originated by ceria donating oxygen to the formation of copper oxides.

Theory and simulation

In order to correctly calculate systems containing ceria, it is important to consider its special electronic properties. The cerium atom in Ce^{3+} valency contains one more electron compared to Ce^{4+} and during the reduction a localization of this electron into a 4f band of Ce^{3+} cation occurs. The strong spatial localization of the Ce 4f states undermines the predictive power of most of the energy functionals available for DFT calculations. The problem lies in the limited ability of the standard functionals in correctly capturing the self-interaction correction.

Different approaches for calculation of cerium were proposed in Ref. [19, 20, 21, 22, 23, 24], such as the core-state model for Ce^{4+} and valence-band model for Ce^{3+}. Another approach to compensate for strong on-site Coulomb repulsion and to deal with localization of electrons in cerium atom is to add Hubbard-U term to LDA or GGA functional, which significantly increases stability of physical solution of DFT calculation [25, 19, 26].

Many theoretical calculations were performed on both bulk copper and ceria. Lattice parameter and bulk modulus of ceria were calculated by the means of DFT

(density functional) approach with local density approximation (LDA) or generalized gradient approximation (GGA) [27, 28, 20]. PAW (projector augmented-wave) approach within DFT was used in calculations as well as molecular dynamics [21] or many others [29, 30, 31, 32, 23, 33, 34, 35, 20, 36, 37]. Several theoretical calculations were carried on ceria surfaces, for example force field calculations of surface energy and surface relaxation of CeO_2(111),(100) and (110) [38, 39, 40, 41, 42], two-dimensionally periodic Hartree-Fock calculations [22] and DFT+U calculations of surface energy and relaxation [43]. The calculations concerning copper include calculation of lattice parameter, bulk modulus, surface energies and relaxations of different copper surfaces and interactions of different adsorbates on copper surfaces [44, 45, 46, 47, 48, 49, 50, 51, 52].

The oxygen storage and buffering capacity of ceria is related to the presence and formation of the oxygen vacancies leading to the surface reduction [19, 1, 53, 54]. It corresponds to the change of valency $Ce^{4+} <- > Ce^{3+}$ of the exposed surfaces.

Several papers were published concerning calculations of systems containing either ceria or copper, or similar systems with different components. Studies were reported on adsorption of various metals on ceria surfaces. Adsorption of Pt and Pd adatoms on reduced and unreduced ceria surfaces was studied by the means of DFT in GGA+U approximation. The bonding of Pd and Pt adatoms on the reduced ceria surfaces was determined stronger than the bonding on the stoichiometric surface. The influence of Pd and Pt adsorption on the increase of oxygen storage capacity of ceria was discovered and reported in [55, 56], more details are provided in the Section **4.1**.

The adsorption of gold on ceria surfaces is currently among the major scientific issues in the field. The most stable adsorption site for gold adatom on stoichiometric ceria surface is reported as the bridge site between two surface oxygen atoms. The oxidation of the gold adatom is suggested and occupation of Ce 4f states was discovered upon adsorption. The ionic bonding was found out between the gold adatom and cerium atom while adsorbing on reduced ceria surface with oxygen vacancy [57, 58, 59]. The mechanisms of CO oxidation on Au/CeO_2 systems and the influence of gold on the catalytic activity of the system were recently revealed [59].

In Ref. [60] the systems composed of metals as Pd or Pt on ceramics as CeO_2 or ZrO_2 were explored. The system of α-Al_2O_3(0001)/Ni(111) was examined in Ref. [61, 62, 63] α alumina being frequently used as an inert support was a subject of studies in Ref. [64] with Nb and in Ref. [65] with Ag. The behaviour of the Cu/α-Al_2O_3 was studied in several publications such as Ref. [66, 67, 68, 69, 70, 71]. More details of the reported calculations are provided in the Section **5.1**.

1.2 Work plan

The present work is a theoretical analysis based on the numerical DFT+U simulations by which we investigate the structural and electronic properties of several Cu/CeO_2 model systems. This system has important applications as an heterogeneous catalyst for CO oxidation and the recent experiments performed on this sys-

tem require theoretical support. In particular we provide insight into the cohesion of the interface between metal Cu nanoparticles supported on CeO_2 substrates. We analyze this issue both in the context of small supported clusters of Cu (Chapter 4) as well as of the extended interface underneath Cu nanoparticles on ceria surfaces (Chapter 5). To this end we focus on the model $Cu(111)/CeO_2(111)$ interface and to the adsorption of Cu adatom at the oxidized and reduced $CeO_2(111)$ surface. Our study provides a direct correlation between the cohesive and electronic properties mediated by the charge transfer process. The different systems examined in the thesis are displayed in Fig. 1.1.

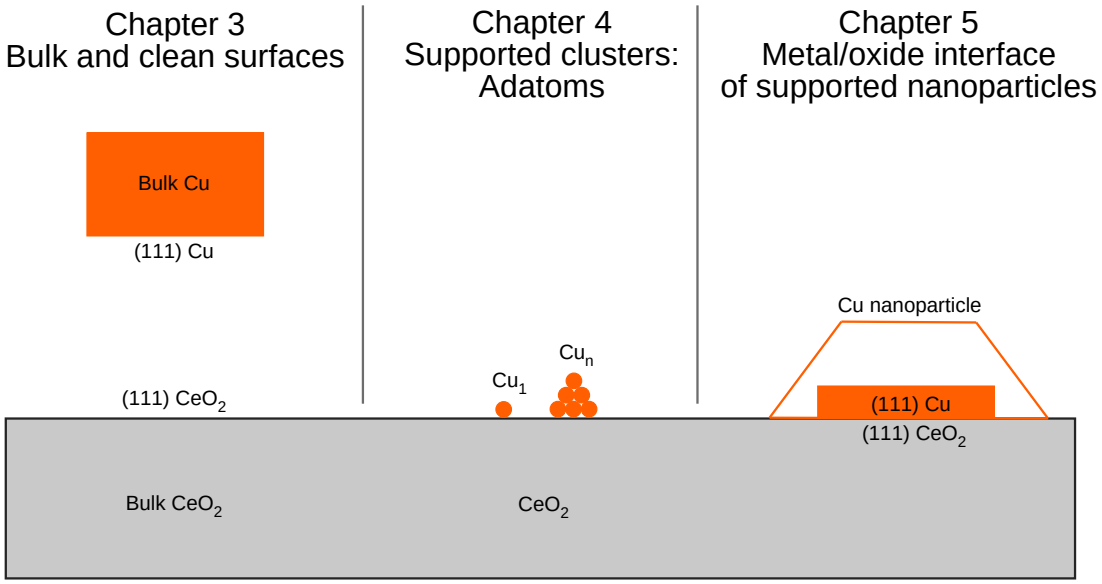

Figure 1.1: **Graphical summary of the thesis:** The different Cu/CeO_2 systems examined in the present thesis are displayed together with the Chapter in which the system is explored.

The thesis is organized as follows.

In the second Chapter we briefly describe the theoretical methods used to model the Cu/CeO_2 systems. We introduce the Density Functional Theory together with the approximations necessary for its practical use. We show also the changes implemented on the DFT for use on the strong correlated systems such as the systems containing cerium oxides.

In the third Chapter we calculate some basic bulk and surface properties of the individual components of the studied system, copper and ceria. We also perform convergence tests in order to estimate precision of the reached results. We concentrate on the convergence of the bulk modulus, lattice parameter and total energy with respect to the calculation parameters controlling the accuracy of the results.

In the fourth Chapter we focus on the systems composed of copper adatoms adsorbed on oxidized and reduced ceria surfaces. We calculate the energetics, as well as the electronic and structural bonding properties of the fore-mentioned adatom on both types of the surface. We find the bonding properties of the adatom on the reduced surface different from the bonding properties on the stoichiomet-

ric unreduced surface, where two possible configurations with similar bonding properties are discovered.

In the fifth Chapter we study the $Cu(111)/CeO_2(111)$ interface. We determine the local structure of the interface and the character of the bonding at the interface. We explore the decay of the interface effects into the deeper bulk regions and also the type of bonding of an ultra thin copper layer on the cerium surface.

In the last Chapter we summarise the main findings and conclusions.

Chapter 2

Density Functional Theory

In this Chapter I will focus on the theoretical methods used to model the Cu/CeO_2 systems. I will introduce the Density Functional Theory and summarize the approximations leading to the practical use of DFT in calculations. The specific implementations of the numerical tools allowing for DFT calculations such as wave-function basis set and pseudopotentials will also be presented.

2.1 DFT

The theoretical understanding of the function of the heterogeneous catalysts, which is of most importance in the present time, requires accurate and precise quantum mechanic calculations. Exploring electronic properties and predicting chemical behaviour of the chemical compounds requires solving the Schrödinger equation. The *time independent Schrödinger equation* is

$$\hat{H}\Psi = E\Psi, \tag{2.1}$$

where $\hat{H}$ is the *Hamiltonian* operator and the Ψ is the wave function describing the state of the system and is a function of all the concerned objects. In case of compounds, the system is composed of nuclei and electrons. Therefore the Ψ is a function of position of each electron and nucleus and the Hamiltonian operator has following form presented in Ref. [72]

$$\hat{H} = -\frac{\hbar^2}{2m_e}\sum_i \nabla_i^2 - \sum_{i,I}\frac{Z_I e^2}{|\vec{r_i} - \vec{R_I}|} + \frac{1}{2}\sum_{i\neq j}\frac{e^2}{|\vec{r_i} - \vec{r_j}|} - \tag{2.2}$$
$$-\frac{\hbar^2}{2M_I}\sum_I \nabla_I^2 + \frac{1}{2}\sum_{I\neq J}\frac{Z_I Z_J e^2}{|\vec{R_I} - \vec{R_J}|}$$

,

where the lower case letters represent the quantities for the electrons and the upper case letters represent the nuclei. The m and M are the masses of the electrons and nuclei respectively, Z stands for the charge of the nuclei. The first term in this many body Hamiltonian is the kinetic energy of the electrons, while the fourth term represents the kinetic energy of the nuclei. The second, third and fifth term express the electron-nuclei, electron-electron and nuclei-nuclei interactions respectively.

Born-Oppenheimer approximation

This very complicated problem can be simplified by realizing that the masses of electrons and ions are of a different order by the factor of almost 2000 [73]. Since the electrons are much lighter than the nuclei and the electronic motion is much faster than the nuclei motion, the *adiabatic* or *Born-Oppenheimer* approximation can be introduced based on treating the electrons and nuclei separately. When studying the electronic state of some compound, the nuclei can be considered at rest and the calculation can be focused on electrons in the potential of the nuclei. The total wave function of the system thus can be rewritten in terms of dividing to the two separate wave functions for electrons and nuclei as presented 2.3

$$\Psi(\vec{R},\vec{r}) = \phi(\vec{R})\psi(\vec{r}). \tag{2.3}$$

The Hamiltonian for system of electrons is thus reduced by neglecting the fourth term in the equation 2.2 and effectively, the ionic coordinates enter the equation as parameters.

Density Functional

The description of the system of electrons by the wave function is still very complicated since for N electrons, the electron wave function is a function of 3N spatial coordinates and N spin variables. It was proved by *Hohenberg* and *Kohn* in Ref. [74], proof is given in Ref. [72], that the ground state properties of a real system are uniquely determined by (are functionals of) the ground state electron density, which is a function of only one set of coordinates. It was also shown that the external potential acting on the electrons determines this electron density. This simplification was one of the most important steps into the practical use of DFT and led to the Nobel prize in Chemistry for W. Kohn.

Hohenberg and Kohn also showed, that a unique and universal functional of the electron density $F[n(\vec{r})]$ exists, that is present in variational principle of a total energy functional $E[n(\vec{r})]$

$$E[n(\vec{r})] = F[n(\vec{r})] + \int V_{ext}(\vec{r})n(\vec{r})d\vec{r}, \tag{2.4}$$

where $F[n(\vec{r})]$ contains the kinetic energy and the mutual Coulomb interaction of the electrons and the $V_{ext}(\vec{r})$ is external potential acting on the electrons.

Kohn-Sham equations

The next very important step towards the practical applications of DFT was the substitution of the problem concerning electrons interacting with each other by an auxiliary problem of non-interacting particles with the same electron density that had the interacting problem. The legitimacy of such substitution was shown by *Kohn* and *Sham* in Ref. [75], again the proof is given in Ref. [72] as well. Because of this approach, the functional $F[n(\vec{r})]$ formerly complicated by containing the interaction effects of the electron could be simplified to be composed of the functionals of the kinetic energy of the non-interacting electrons, their Coulomb interaction treated as a mean field and the exchange-correlation energy E_{xc} which

accounts for all the other many-body interaction effects. It also allows to overcome the many-particle problem by solving one-particle equations as will be described in following.

As a result of the simplifications described above, solving of the Schrödinger equation 2.1 with a Hamiltonian 2.2 for a complete system reduces to solving the *Kohn-Sham one particle equations*

$$\hat{H}_{KS}\psi_i(\vec{r}) = [-\frac{\hbar^2\nabla^2}{2m} + V_{KS}(\vec{r})]\psi_i(\vec{r}) = e_i\psi_i(\vec{r}), \tag{2.5}$$

where the $\psi_i(\vec{r})$ are one-particle wave functions and $V_{KS}(\vec{r})$ is the *Kohn-Sham potential* defined as

$$V_{KS}(\vec{r}) = V_{ext} + e^2 \int \frac{n(\vec{r'})}{|\vec{r} - \vec{r'}|} d\vec{r'} + v_{xc}(\vec{r}). \tag{2.6}$$

The Kohn-Sham potential was derived from the properties of the functional $F[n(\vec{r})]$ for example in Ref. [76] or [72]. The second term in the formulation for the Kohn-Sham potential is the contribution from the Coulomb interaction of the electrons and the third term $v_{xc}(\vec{r})$ is the exchange-correlation potential defined as

$$v_{xc}(\vec{r}) = \frac{\delta E_{xc}[n]}{\delta n(\vec{r})}. \tag{2.7}$$

The Kohn-Sham equations are an effective way of acquiring properties of materials, but since the electron density is a result of solving the equations as well as it enters the equation through the Kohn-Sham potential, the solution has to be reached iteratively.

Exchange-correlation functionals

Every quantity present in the Kohn-Sham equations is exact and well defined. However the exchange-correlation energy has a very complicated expression, which is not known explicitly. This is the reason to introduce an approximation to the theory in form of simplifying the exchange-correlation energy.

The most simple approximation is called *LDA*, the *Local Density Approximation*. In LDA, the exchange-correlation energy is expressed in terms of exchange-correlation potential of the uniform electron gas, that can be calculated with great accuracy

$$E_{xc}^{LDA}[n] = \int \epsilon_{xc}^{hom}(n(\vec{r}))n(\vec{r})d\vec{r}, \tag{2.8}$$

where $\epsilon_{xc}^{hom}(n(\vec{r}))$ is the exchange-correlation density of the uniform electron gas.

The idea is to apply this function also to inhomogeneous systems, for which the value of the exchange-correlation energy is calculated point-by-point as a function of the local density with the exchange-correlation potential derived for uniform electron gas having that density.

According to Ref. [76] the LDA can be used to calculate systems such as simple metals, intrinsic semiconductors or even non homogeneous systems as covalently bonded materials and some transition metals. It usually predicts structural and vibrational properties of those materials well but it tends to underestimate the equilibrium bond lengths and overestimate the bonding energies compared to experiments.

Some of the drawbacks of the LDA approximation can be overcome by introducing a more complicated approximation for the exchange-correlation energy – the *GGA*, *Generalized Gradient Approximation*. This approximation include also the influence of the local inhomogeneities of the electron density. The general expression of the exchange-correlation energy in the GGA approximation is

$$E_{xc}^{GGA}[n] = \int \epsilon_{xc}^{GGA}(n(\vec{r}), |\nabla n(\vec{r})|) n(\vec{r}) d\vec{r}, \tag{2.9}$$

where the $\epsilon_{xc}^{GGA}(n(\vec{r}), |\nabla n(\vec{r})|)$ is different for different concrete formulation of the GGA exchange-correlation energy. In this work we use the formulation of Perdew-Burke-Ernzherof (PBE) reported in Ref. [77].

In order to model materials with magnetic properties, it is useful to have the exchange-correlation energy functional directly dependent on the two spins. Therefore more complicated *Local Spin Density Approximation* (*LSDA*) and also *spin polarised GGA* were formulated.

Periodic systems

The calculation of the bulk materials are based on the assumption, that the system is periodic with respect to the position of atoms, thus the external potential $V_{ext}(\vec{r})$ acting on the electrons is periodic with the periodicity of the lattice of the crystal. This periodicity can be expressed as

$$V_{ext}(\vec{r} + \vec{R}) = V_{ext}(\vec{r}), \tag{2.10}$$

where $\vec{R}$ is vector in the crystal created as integer linear combination of the crystal lattice vectors.

Not only the external potential is periodic, but also the electronic Hamiltonian operator and the physical quantities describing the system are also periodical with the same periodicity. The *Bloch theorem* can be applied expressing the single particle electronic wave function as

$$\psi_{\vec{k}v}(\vec{r}) = e^{i\vec{k}\cdot\vec{r}} u_{\vec{k}v}(\vec{r}), \tag{2.11}$$

where $u_{\vec{k}v}(\vec{r})$ is a function with the same periodicity as the crystal, the v is a discrete band index and $\vec{k}$ is the crystal momentum of the electrons defined within the first Brillouine Zone in the reciprocal space. The reciprocal space is in the relation with the real space via the expression

$$\vec{b}_i \cdot \vec{u}_j = 2\pi\delta_{ij}, \tag{2.12}$$

where the $\vec{b}_i$ are lattice vectors of the reciprocal space, $\vec{u}_j$ are lattice vectors of the real space and the indexes i and j are considered equal to 1, 2, 3.

Because of the translational invariance, the k-points can be treated independently. The sums over the electronic states figuring in expressions for many physical quantities correspond to the integrations in the Brillouine Zone and sums over the band index v. The symmetry of the crystal allows to substantially reduce the number of k-point used for the integration and the reduction can be increased by using special points techniques such Monkhorst-Pack technique reported in Ref. [78]. The number of k-points used in the calculation influence the accuracy of obtained results, so the convergence of the results with respect to the number of k-points has to be checked. To the systems which are not naturally periodic such as surfaces or interfaces the periodicity has to be artificially added for example by using a supercell method. The use of the supercell method will be shown in following Chapters.

The application of the special point technique on the metals has difficulties because of relatively small k-point sampling of the area around the Fermi level with respect to the sensitivity of metallic properties in this area. This can be solved by either using the tetrahedron method as reported in Ref. [79] or by introducing a smearing to smooth the weight of the states. The different smearing techniques depend on the function used for the smearing as for example the finite temperature Fermi distribution, the Lorentzian, the Gaussian [80], cold smearing factors [81] or the Methfessel and Paxton smearing technique [82].

The plain wave pseudopotential method

In order to perform practical calculations, the continuous problem has to be transformed to the more algebraic one. To this end the electronic wave functions are expanded to the basis set, in this work the *Plane Wave* basis set was used. This representation profits from Fourier transformation, for which efficient algorithms are available.

The Bloch electronic wave functions in this representation are

$$\psi_{\vec{k}v}(\vec{r}) = \frac{1}{(N\Omega)^{\frac{1}{2}}} \sum_{\vec{G}} e^{i(\vec{k}+\vec{G})\cdot\vec{r}} c_v(\vec{k}+\vec{G}), \tag{2.13}$$

where the Ω is the volume of the unit cell, the $\vec{G}$ are reciprocal lattice vectors and the $c_v(\vec{k}+\vec{G})$ are normalized Fourier coefficients.

The absolute precision of the result can be achieved by use of infinite number of vectors $\vec{G}$, which is not possible in the numerical calculations. Therefore only plain waves contained in the sphere of maximum kinetic energy E_{wfc}^{cut} are used in the real calculations:

$$\frac{\hbar}{2m}|\vec{k}+\vec{G}|^2 < E_{wfc}^{cut}. \tag{2.14}$$

The number of plain waves used influences the accuracy of the solutions, therefore the E_{wfc}^{cut} parameter has to be chosen carefully. More on this subject is explained in the following Chapter.

Describing the wave functions of core electrons would require a prohibitively large number of plane waves, because of the strong localization of the wave function. This can be partially avoided by using the *Pseudopotential method*. This

technique is based on the fact that the studied chemical and physical properties of the system are determined by the behaviour of the electrons in the valence bands. The electrons near to the core can be perceived as integrated to the core forming an ionic core. The pseudopotential is calculated as the external potential of those ionic cores acting on the valence electrons. The calculations then can be applied only on the valence electrons which increase the applicability of the calculations by lowering the complexity of the problem. In this thesis the ultrasoft potential as described in Ref. [83] was used.

2.2 DFT+U

In the case of materials with valence electrons localised closer to the core, many-body effects become more and more important and better approximations than LDA or GGA are necessary [76]. One of the possibilities that has been proposed for modeling strongly-correlated materials is the "so called" DFT+U method. In this method a *Hubbard U term* is added to the LDA or GGA energy functional.

The new, corrected functional is formulated as

$$E_{xc}^{LDA/GGA} = E_{xc}^{LDA/GGA} + \frac{U}{2}\sum_{I} Tr[\mathbf{n}^I(1-\mathbf{n}^I)], \tag{2.15}$$

where $\mathbf{n}^I$ represent the $M \times M$ matrices and projections of the one-electron density matrix $\hat{\rho}$ over the f manifold localized at lattice site I

$$\langle \phi^I_{m\sigma} | \hat{\rho} | \phi^I_{m'\sigma'} \rangle = n^{I\sigma}_{\sigma\sigma'}. \tag{2.16}$$

M stands for the degeneracy of the localized atomic orbital (14 in the case of f orbitals).

In the case of calculation of the systems containing ceria in the present thesis, the Hubbard U term is chosen 4.5 eV, which is in agreement with reported calculations performed by the same method [26, 84].

Chapter 3

Simulating Cu and CeO_2 materials

Before analyzing the properties of the Cu/CeO_2 contact at surfaces and interfaces, which are the main subject of this thesis, in this Chapter I perform a preliminary study of the individual constituents, namely the bulk copper, the bulk ceria and the (111) surfaces of both substances. The calculation of the bulk and surface properties of these systems, which I will report in this Chapter, provide us with a benchmark for determining the accuracy of the predicted results described in the following Chapters.

In this Chapter I describe and discuss the preliminary test that were performed to explore the convergence of the calculated results. To this end, I will focus on the dependency of the total energy, bulk modulus, and equilibrium lattice parameter on several technical parameters. In particular, I will focus on the basis-set size and on the k-point grid used for integrating the Brillouin Zone. In our plane-waves pseudo-potential formulation the three main parameters controlling these quantities are the energy cutoffs for the basis function and density representation (E_{wfc}^{cut} and E_{rho}^{cut}, respectively) and the k-point mesh. E_{wfc}^{cut} determines the size of the basis set used to describe the electronic pseudo wave function. As a side effect, it also controls the cost of the calculation in terms of computational time and memory usage. The basis set includes all plane waves whose wave number $\vec{k}+\vec{G}$ verify the condition 2.14.

The other parameter analyzed is E_{rho}^{cut} that control the density representation and that, for the case of ultrasoft pseudopotentials, should be larger than the value of 4*E_{wfc}^{cut} so as to properly account for the augmentation charge. Finally the integrals in the Brillouin Zone are calculated numerically using a finite grid of k points, chosen according to the Monkhorst-Pack grid [78] using the Methfessel-Paxton scheme [82] toghether with an energy broadening of 0.01 eV.

All calculations were based on Density Functional Theory using GGA approximation for the exchange-correlation functional in the formulation of Pedrew-Burke-Ernzerhof [77]. The plain wave pseudopotential method were used as implemented in the PWscf code of the Quantum ESPRESSO distribution [85]. To describe electron-ion interactions, we use Vanderbilt ultrasoft pseudopotential [83]. The structures were visualised by XCrysDen visualisation program [86].

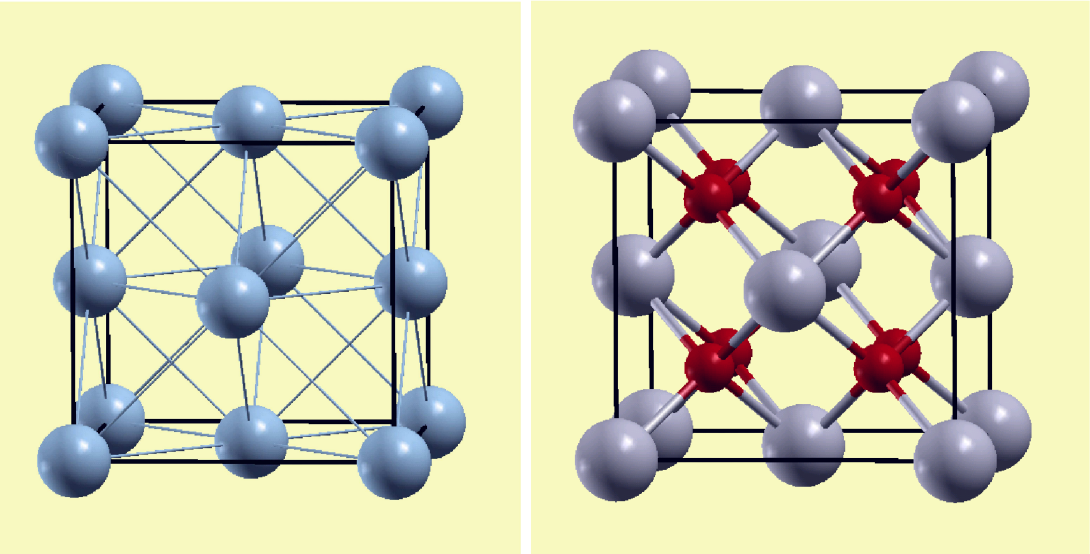

Figure 3.1: **Crystal structure of copper and ceria.** The unit cell of copper has a fcc symmetry (left) and the unit cell of ceria with cubic fluorite lattice corresponds to spatial group Fm3m (right).

3.1 Bulk copper

First we studied the main properties of the bulk copper. Copper is a transition metal that crystallize in the face-centered cubic structure displayed in Fig. 3.1 (left).

First we explored the lattice parameter of the bulk copper. To this end, self consistent calculations for different lattice parameters were performed fixing E_{wfc}^{cut} to 25 Ry and E_{rho}^{cut} 300 Ry, and using a k-point mesh of (8×8×8) consisting of 29 inequivalent k-points in the Brillouine Zone. The Murnaghan equation of state was fitted to the energies resulting from the calculations and the minimal lattice parameter of 3.639 Å was thus estimated. The results of the calculations together with the fitted curve are displayed at the area around the equilibrium in Fig. 3.2.

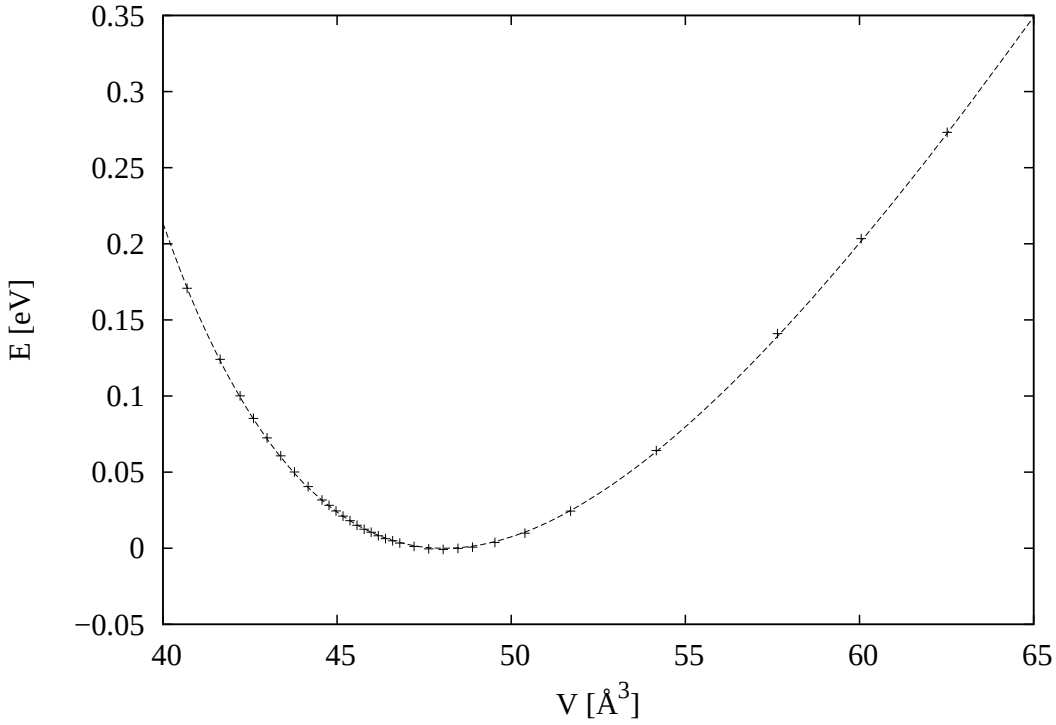

Figure 3.2: **Calculated energy-volume curve for bulk copper.** Volume is displayed in Å^3. The data were fitted with Murnaghan equation of state. Zero energy is set to the minimum of the fit.

We took eleven values of lattice parameter around the minimum acquired from the previous calculation and used them for the convergence tests. The tests were performed in the range 10-70 Ry for E_{wfc}^{cut}, 100-700 Ry for E_{rho}^{cut} and (5×5×5) - (15×15×15) for the k-point meshes by performing self consistent calculations at the eleven values for lattice parameter. For each combination of the parameters, the Murnaghan equation of state was fitted on the data and the minimal lattice parameter, bulk modulus and the total energy for one set lattice parameter were calculated. The complete results are presented in the CD attached to the thesis. The most important data sets are summarized in Fig. 3.3 and 3.4.

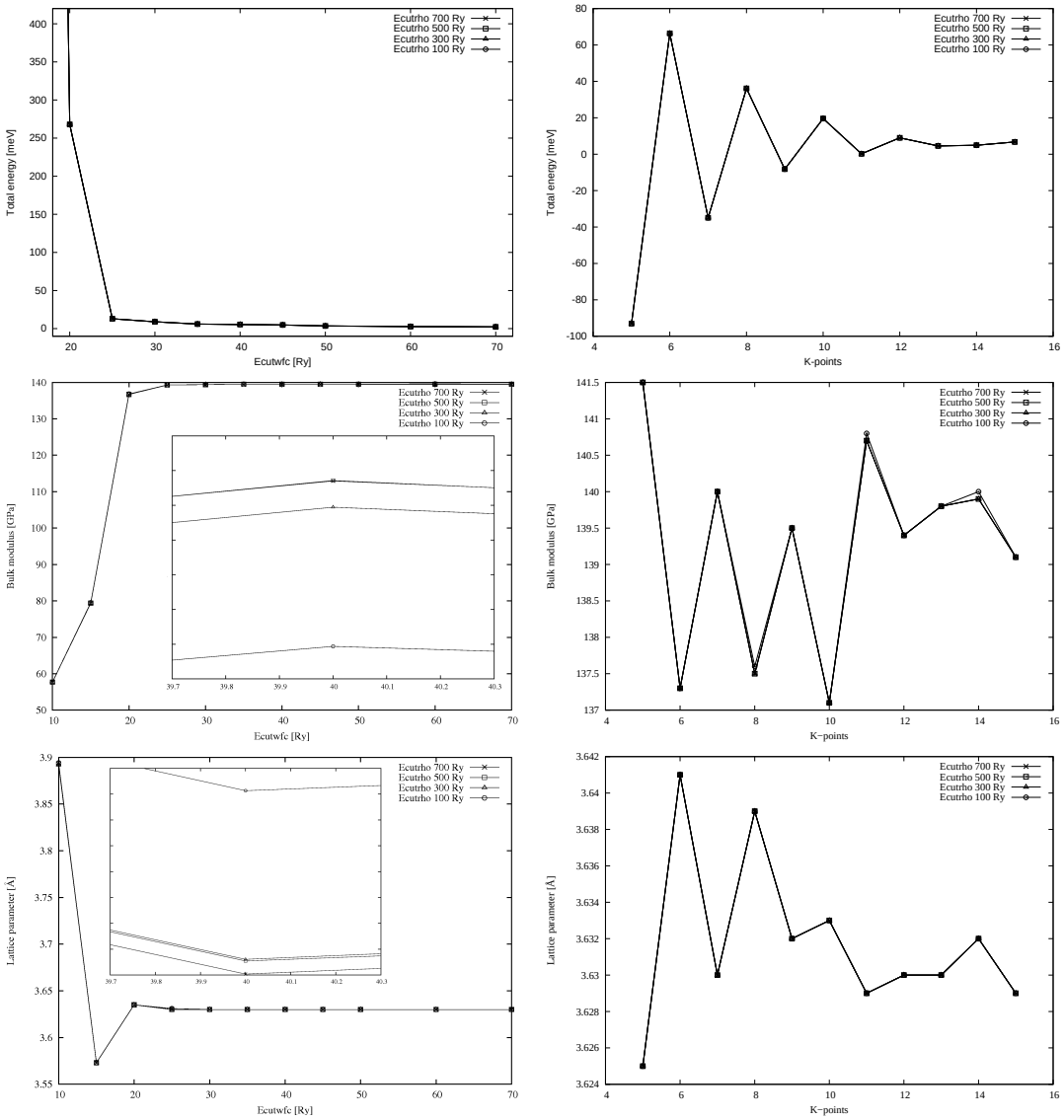

Figure 3.3: **Summary of the data set used for the convergence tests – parameter $\mathbf{E}_{rho}^{cut}$.** The equilibrium lattice parameter (bottom), the bulk modulus (middle) and the total energy with respect to the converged value (up) are displayed as a function of the k-point mesh with fixed E_{wfc}^{cut} 30 Ry (right) and E_{wfc}^{cut} with fixed k-point mesh (12×12×12) (left) for four values of parameter E_{rho}^{cut} (100, 300, 500 and 700 Ry). Where necessary, a zoom at one of the points is presented as inset in the corresponding panel.

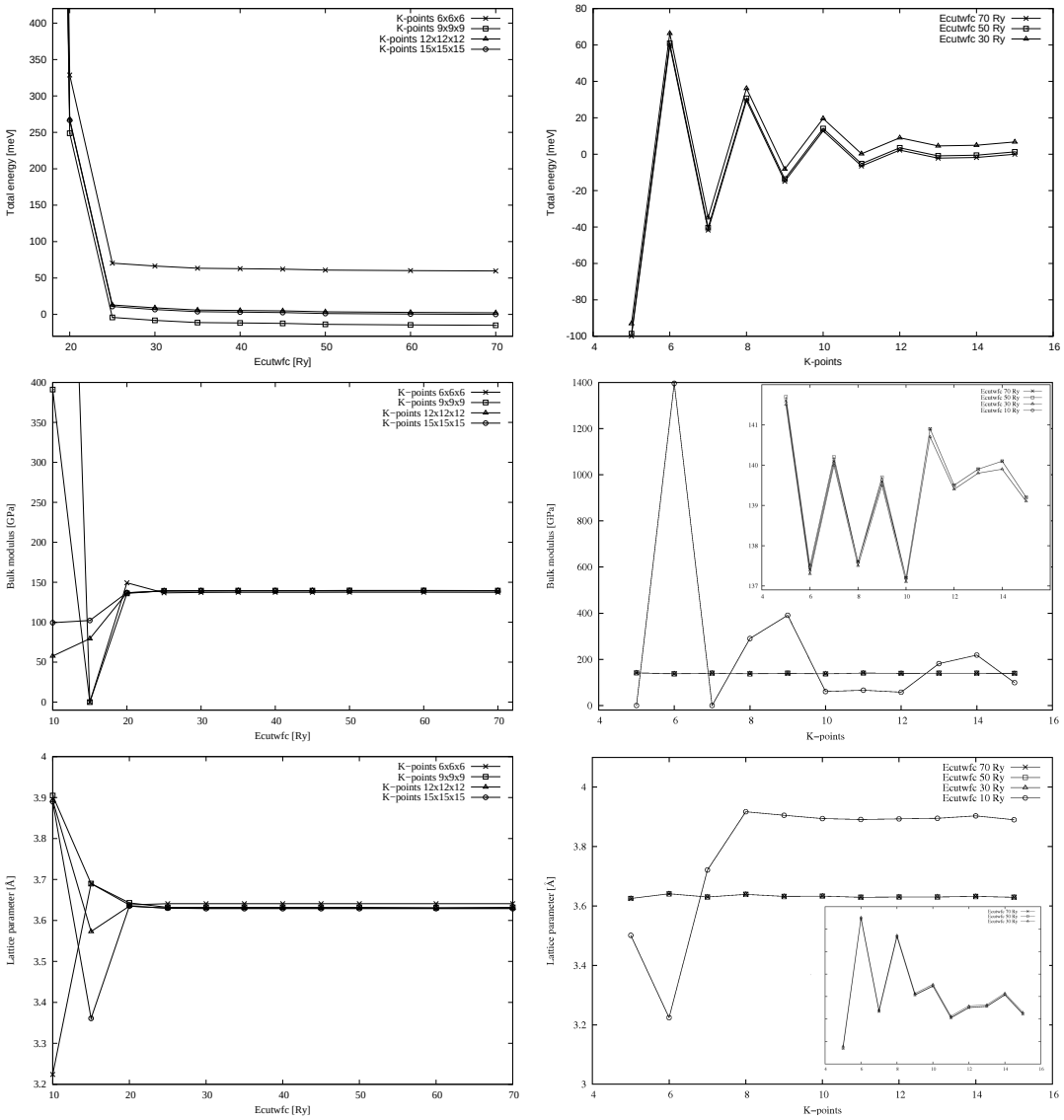

Figure 3.4: **Summary of the data set used for the convergence tests – fixed E_{rho}^{cut}.** The equilibrium lattice parameter (bottom), the bulk modulus (middle) and the total energy with respect to the converged value (up) are displayed as a function of the k-point mesh (right) and E_{wfc}^{cut} (left) both with fixed parameter E_{rho}^{cut} 400 Ry. The four curves in the left sub-figures represent k point meshes (3×3×3), (9×9×9), (12×12×12) and (15×15×15), while the curves in the right sub-figures show different E_{wfc}^{cut} parameters 10, 30, 50 and 70 Ry. Where necessary, a zoom at one of the points is presented as inset in the corresponding panel.

Figures 3.3 and 3.4 display the bulk modulus, total energy and minimal lattice parameter as a function of E_{rho}^{cut}, E_{wfc}^{cut} and number of k-points. The displayed values for total energy were calculated at the value of the lattice parameter of 3.639 Å corresponding to the minimum energy predicted by the preliminary calculation displayed in Fig. 3.2. In these figures, the zero energy is set at the value calculated with the best set of parameters, E_{wfc}^{cut} 70 Ry, E_{rho}^{cut} 700 Ry and k-point mesh (15×15×15).

The results presented in Fig. 3.3 allow us to conclude that the results are well

converged for values of E_{rho}^{cut} larger than 100 Ry. For larger values, the curves fall within 0.01 GPa for bulk modulus and 0.04 mÅ for minimal lattice parameter difference. The convergence in the total energy is even better, since the difference of the curves is less than 0.1 meV.

The convergence tests displayed in Fig. 3.4 calculated at a fixed value of E_{rho}^{cut}=400 Ry show that the results are well converged for E_{wfc}^{cut} larger than 25 Ry. For these values the total energy remains within 11 meV, the bulk modulus within 0.4 GPa and the equilibrium lattice parameter within 0.3 mÅ. Convergence on the number of k points used to integrate the BZ was achieved for k-point mesh larger than (11×11×11). For these, the calculated total energies lie within 6 meV, the bulk modulus within 10 GPa and the minimal lattice parameter within 3 mÅ. In order to perform the calculations with precision of 3 mÅ for the calculated lengths and 6 meV for the total energy, we chose the parameters 30 eV for E_{wfc}^{cut}, 300 eV for E_{rho}^{cut} and (12×12×12) k-point mesh consisting of 72 inequivalent k-points.

In conclusion, after having optimized the most relevant computational parameter, we can safely predict the structural and electronic properties of bulk Cu. The calculated minimum lattice parameter and the corresponding bulk modulus were found out to be 3.63 Å and 139 GPa respectively, which are in good agreement with values from different reported theoretical calculations with GGA approximation 3.66 Å[44], 3.64 Å[45] [52], 141 GPa [45] and 140 GPa [51] as well as with experimental lattice parameter 3.61 Å and experimental bulk modulus 137 GPa [87].

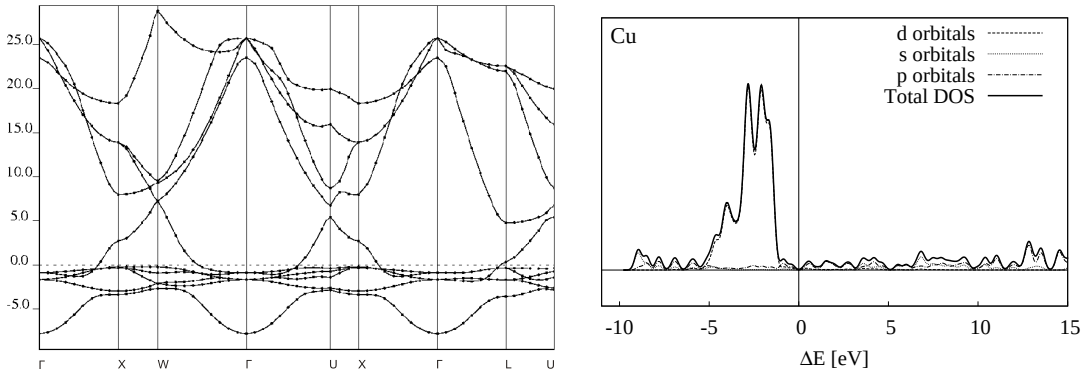

Figure 3.5: **Electronic properties of bulk copper:** Density of states of a bulk copper atom (right) and calculated band structure for copper along high-symmetry directions in Brillouin Zone (left) are presented. Zero energy is set at the Fermi level.

The electronic band structure of bulk Cu calculated with the parameters determined above is displayed in Fig 3.5 (left). The electronic eigenvalues are plotted along the ΓXWΓUXΓLU directions in the 1st Brillouin Zone. The corresponding total density of electronic states (DOS) is displayed in Fig 3.5 (right). The DOS analysis was performed with (24×24×24) k-point mesh. In both cases, the energies are plotted with respect to the Fermi level. From Fig. 3.5 (left) it is apparent, that the dense d bands located below the Fermi level are completely filled and create a sharp peak at the DOS curve clearly shown in the right panel of Fig. 3.5

(right). The Fermi energy intersects the large s bands, which therefore confers the metallic character to Cu.

3.2 Cu (111) surface

The (111) copper surface was modeled with a (1×1) supercell by using the quantities determined in the study of Cu bulk, particularly the lattice parameter and the energy cutoffs for the wavefunctions and the charge density. The supercell consisted of several layers of copper atoms separated by a layer of vacuum 14.35 Å thick in the z direction. Several single point calculations were performed with number of layers ranging from two to eleven. Then we explored the structural modifications induced by the surface by relaxing the atomic coordinates according to the calculated Helmann-Feynman forces. We performed two set of relaxations: in the first one, all atoms were relaxed, in the second one, only the atoms in the upper half of the supercell were relaxed, while the other half were constrained to their equilibrium bulk positions. The criterion for the convergence was both on the total energy and on the forces: difference in total energy between consecutive iterations smaller than 0.001 eV, and forces acting on the atoms less than 0.02 eV/Å.

$$E_{surf} = (E_{slab}^{TOT} - nE_{bulk}^{TOT})/2A \tag{3.1}$$

The surface energy for all the supercells was calculated according to the formula 3.1, where the E_{surf} is the surface energy, the E_{slab}^{TOT} is the calculated total energy of the system with vacuum layer, E_{bulk}^{TOT} is the total energy of one bulk atom, n is the number of atoms in the slab and A is the area of one surface in the supercell. The changes of the distances of the layers are displayed in Table 3.1 together with the surface energies before and after the relaxation. The surface energies are in J/m^2, while the changes of the distances are presented in Å, the positive values represent the decrease of the distance of the layers, the negative values show the increase.

The relaxation resulted in decrease of the inter-atomic distances between the surface and subsurface layer by 0.02-0.04 Å which are larger values than 0.014 Å reported in Ref. [44] and 0.019 Å in Ref. [45] and in better agreement with result reported in Ref. [46, 47] 0.035 Å. The difference was probably caused by the fact, that we relaxed all the atoms, but in the references, only the surface layer was relaxed. Our best estimated value of surface energy is 1.67 J/m^2, slightly lower than 1.8 J/m^2 reported in Ref. [46] but still in good agreement with the experimental value 1.83 J/m^2 in Ref. [49], while higher than the value 1.34 J/m^2 reported in Ref. [45] and 1.28 J/m^2 Ref. [44]. The relaxation lowered the surface energy in most cases by approximately 0.01 J/m^2.

Supported by the Ref. [48, 50, 46], where the adsorption calculations were performed on the 3-layers thick slab of copper and where it was shown that the 3 layers provide enough convergent results to this type of calculations, the 4-atoms thick slab was chosen to be sufficient in the surface and interface calculations in the presented work.

Table 3.1: **Surface energies and relaxations**

	2	3	4	5	6	7	8	9	10	11
Cu(1)-Cu(2) [Å]	-0.01	0.04	0.04	0.03	0.04	0.02	0.03	0.02	0.02	0.02
Cu(2)-Cu(3) [Å]			0.02	0.03	0.03	0.01	0.03	0.03	0.02	0.02
Cu(3)-Cu(4) [Å]					0.01	0.00	0.03	0.02	0.00	0.01
Cu(4)-Cu(5) [Å]							0.01	0.01	-0.01	-0.01
E_{surf}^{scf} [J/m^2]	1.629	1.695	1.612	1.650	1.648	1.622	1.673	1.585	1.650	1.643
E_{surf}^{relax} [J/m^2]	1.628	1.685	1.599	1.637	1.632	1.617	1.659	1.573	1.645	1.636

	4 – 2 fixed	6 – 3 fixed	8 – 4 fixed
Cu(1)-Cu(2) [Å]	0.04	0.04	0.02
Cu(2)-Cu(3) [Å]	0.04	0.03	0.02
Cu(3)-Cu(4) [Å]		0.03	0.01
Cu(4)-Cu(5) [Å]			-0.01
E_{surf}^{relax} [J/m^2]	1.603	1.639	1.668

The following calculations were performed on two types of supercell, both consisting of four layers of copper and 14.35 Å thick layer of vacuum in z direction and (1×1 or 3×3) atoms in xy plane (the latter displayed in Fig. 3.6 left). The layer of vacuum was determined to be thick enough to prevent surfaces from interacting with each other by another scf calculation with the system with the vacuum layer increased to 15.35 Å, which provided the result differing from the previous result for 0.003 meV. The k-point mesh was chosen (12×12×1) for (1×1) supercell and (4×4×1) for (3×3) supercell.

The slab was relaxed with the two bottom copper layers fixed in position until the force acting on each relaxed atom was less than 0.02 eV/Å. The density of states analysis of atoms in different layers of the slab was performed (displayed in Fig. 3.6, right). For comparison we added to the bottom of the figure also the previously calculated DOS of bulk copper from Fig. 3.5.

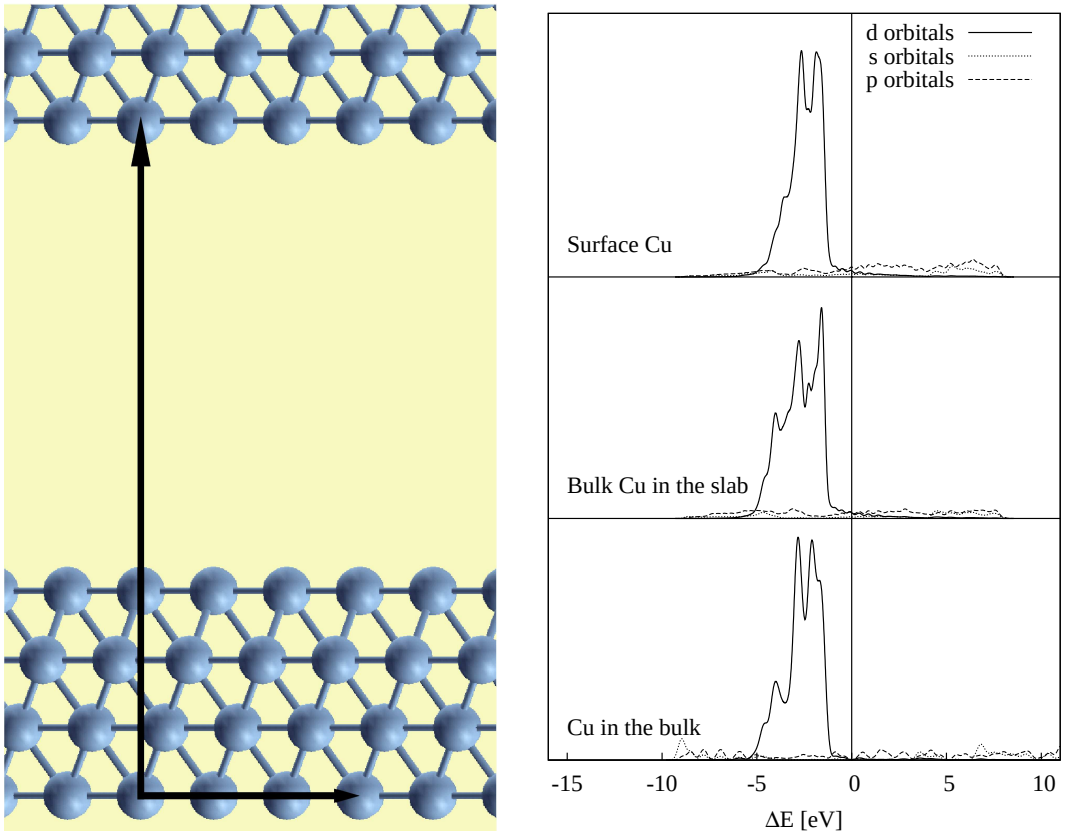

Figure 3.6: **Copper surface:** (3×3) supercell used in the calculations of copper surface (left) and density of states of a copper atoms (right) are presented. The figure contains a DOS of bulk copper (down), DOS of bulk-like copper from the inner layer of the slab (middle) and DOS of copper at the surface of the slab (up). Fermi energy is set at the Fermi level.

3.3 Bulk cerium oxides

Cerium is a rare-earth metal which exists in two main oxidation states Ce^{3+} and Ce^{4+} corresponding to two different oxides, reduced cerium oxide Ce_2O_3 and ceria CeO_2 respectively. The electron configuration of cerium is $1s^2$ $2s^2$ $2p^6$ $3s^2$ $3p^6$ $3d^{10}$ $4s^2$ $4p^6$ $5s^2$ $4d^{10}$ $5p^6$ $4f^2$ $6s^2$. Bulk ceria has a face-centered cubic symmetry with one cerium and two oxygen atoms in a unit cell forming space group Fm3m as shown in Fig. 3.1 (right), while the bulk reduced Ce_2O_3 with two cerium and three oxygen atoms in the unit cell form a space group P-3m1 [88] as shown in Fig. 3.11 (left).

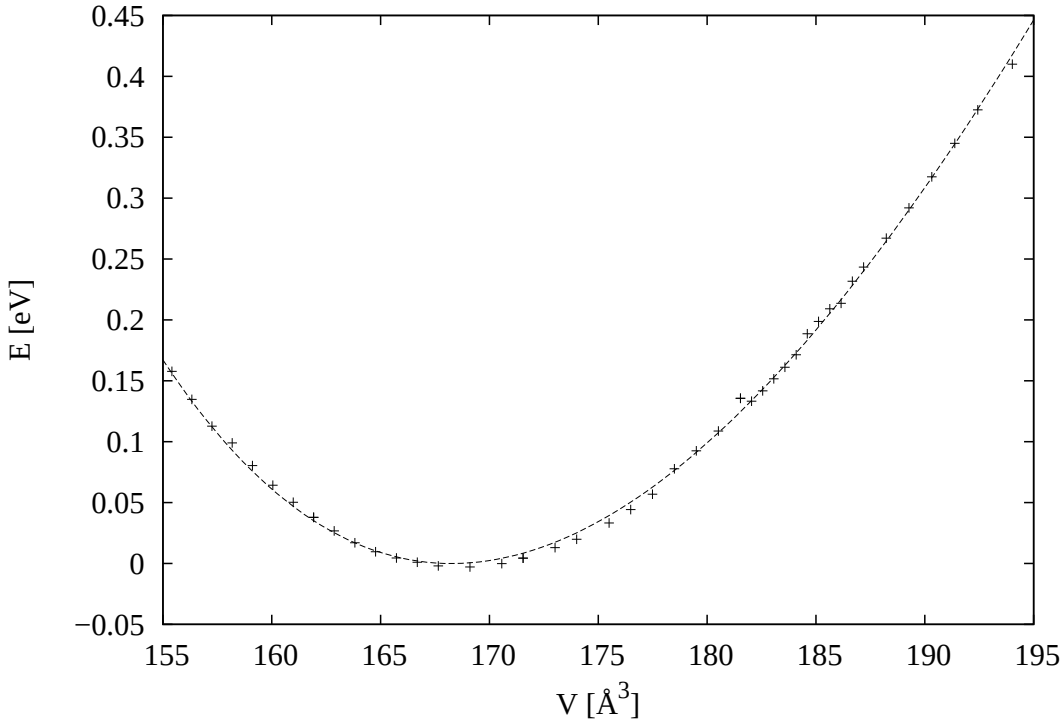

Figure 3.7: **Calculated energy-volume curve for bulk ceria.** Volume is displayed in Å^3. The data were fitted with Murnaghan equation of state. Zero energy is set to the minimum of the fit.

The convergence tests were performed for ceria bulk in the same way as for copper. Again first the lattice parameter was explored in detail with E_{wfc}^{cut} 40 Ry, E_{rho}^{cut} 400 Ry and with k-point mesh (12×12×12) consisting of 144 inequivalent points in the Brillouin zone. The Murnaghan equation of state was fitted to the energy-volume curve acquired from the calculation and the minimal lattice parameter was estimated. The complete results with the fitted curve are presented in Fig. 3.7.

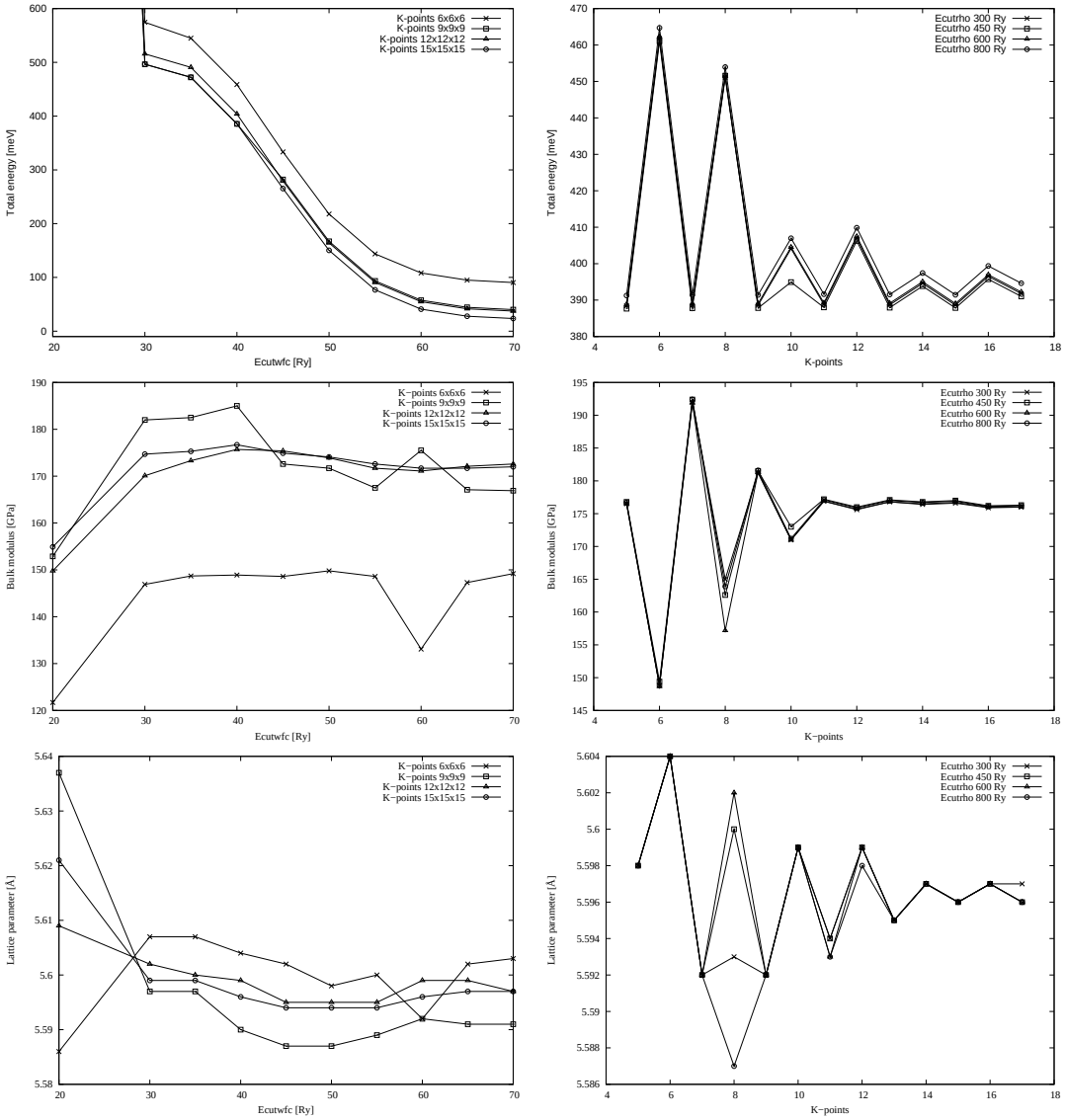

Figure 3.8: **Summary of the dataset used for the convergence tests – A.** The equilibrium lattice parameter (bottom), the bulk modulus (middle) and the total energy with respect to the converged value (up) are displayed as a function of the E_{wfc}^{cut} with E_{rho}^{cut} fixed at 400 Ry for four values of k-point mesh ((6×6×6), (9×9×9), (12×12×12) and (15×15×15)) on the left and as a function of k-point mesh with the E_{wfc}^{cut} parameter fixed at 40 Ry for four values of E_{rho}^{cut} (300, 450, 600 and 800 Ry) on the right. Where necessary, a zoom at one of the points is presented as inset in the corresponding panel.

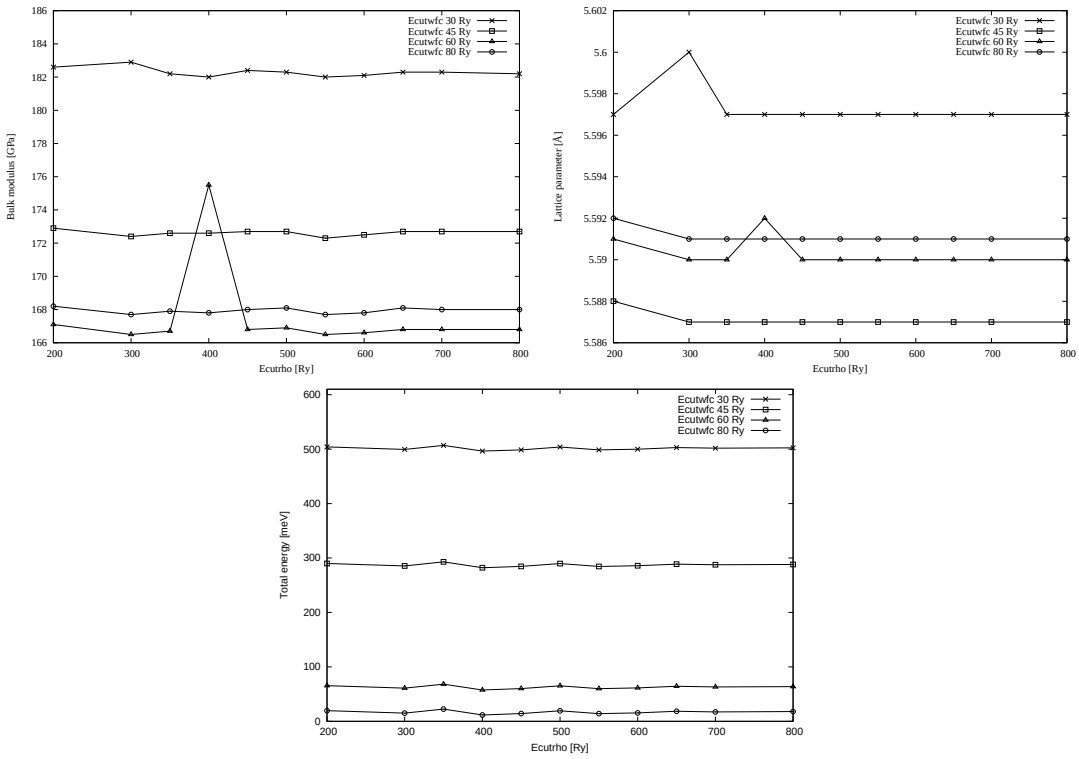

Figure 3.9: **Summary of the dataset used for the convergence tests – B.** The equilibrium lattice parameter (bottom), the bulk modulus (middle) and the total energy with respect to the converged value (up) are displayed as a function of the E_{rho}^{cut} with k-point mesh fixed at (9×9×9) for four values of E_{wfc}^{cut} (30, 45, 60 and 80 Ry) on the right. Where necessary, a zoom at one of the points is presented as inset in the corresponding panel.

Similarly to the case of copper, eleven values of the lattice parameter around the minimum were chosen and used to perform the convergence tests. The tests were conducted with the energy cutoff for wavefunctions in the range 30-80 Ry, the energy cutoff for charge density 300-800 Ry and with k-point meshes from (5×5×5) to (17×17×17). The Murnaghan equation of states was fitted to the results of every combination of input parameters and the minimal lattice parameter, bulk modulus and the total energy for one fixed lattice parameter were established.

The complete results of the convergence tests are presented in the CD attached to the thesis and the most relevant conclusions are summarized in Figures 3.8 and 3.9. The figures display the evolution of the bulk modulus, total energy and minimal lattice parameter as a function of E_{rho}^{cut}, E_{wfc}^{cut} and k-point mesh. The displayed values for total energy were calculated at the value of the lattice parameter of 5.521 Å corresponding to the minimum energy predicted by the preliminary calculation displayed in Fig. 3.2.

Fig. 3.8 shows the change of the total energy, equilibrium lattice parameter and bulk modulus as a function of the energy cutoff for the wavefunctions and of the k-point meshes (6×6×6), (9×9×9), (12×12×12) and (15×15×15) on the left and on the right the changes of the values with the number of k-points for the

values of energy cutoff for charge density 300, 450, 600 and 800 Ry. Fig. 3.9 then displays the evolution of the values with the energy cutoff for the charge density for the four values of energy cutoff for the wavefunctions 30, 45, 60 and 80 Ry.

From the convergence tests we can conclude that the values of the wavefunctions cutoff equal or larger to 30 Ry, values of the density cutoff larger than 300 Ry and a k-point mesh of (8×8×8), allow to predict the bulk modulus in within 20 GPa, the equilibrium lattice parameter within 0.005 Å and the total energy converged up to 0.5 eV. The simulation of the combined Cu/CeO2 systems were thus performed with the parameters determined for the isolated constituents. In this particular case, it is the oxide that limits and determines the basis set size, while the metal control the number of k-point to be used in the BZ integrals.

These computational parameters allow us to predict a calculated equilibrium lattice parameter of 5.525 Å and the bulk modulus of 175 GPa, which is higher than the experimental values for the lattice parameter 5.41 Å [33], 5.411 Å [29, 31] and 5.406 Å [30] and lower than the experimental values for the bulk modulus 230 GPa [31], 236 GPa [30], 204 GPa [34] and the XRD result 220 GPA [29]. Several computed values were reported as well from which we concentrate mostly on those calculated with GGA, 5.39 Å and 215 GPa [20], the results from the Hartree-Fock method 5.385 Å and 357 GPa [32], 5.4105 Å and 263 GPa [35], 5.45 Å and 194 GPa [23], 5.384 Å and 176.9 GPa [29], 5.48 Å and 187.7 GPa [20], 5.47 Å and 172 GPa [37], 5.47 Å [21] and 5.335 Å [36]. The reported equilibrium lattice parameters are lower than our calculated value, whereas the calculated bulk modulus is lower than some of the reported values and in good agreement with the last three mentioned.

The electronic band structure of the bulk ceria was calculated and the eigenvalues are displayed in Fig 3.10 (left) along the ΓXWΓUXΓLU directions in the first Brillouin Zone in 60 k-points along the line. The corresponding total density of state together with the density of states projected on each of the atoms in unit cell is presented in the Fig 3.10 (left). The DOS was calculated with increased k-point mesh (36×36×36). The zero energy is set at the Fermi level in both subfigures. Fig 3.10 (left) clearly show the oxygen p states located below the Fermi level and also the dense cerium f states above the Fermi level corresponding to the sharp peak of unoccupied states in the total DOS curve. The band gap apparent at the DOS figure is responsible for the insulating character of ceria.

For comparison we calculated the density of states of reduced cerium oxide Ce_2O_3 as well. While in ceria the valence Ce states are empty, in reduced Ce_2O_3, one electron of each Ce ion occupies 4f cerium band. In order to provide the correct insulating description of Ce_2O_3, it is necessary to go beyond the standard LDA or GGA approximation. One possibility to do so is by the addition of the Hubbard-U term to the exchange-correlation functional in calculations containing cerium. The Hubbard-U term deals in correct way with the electronic correlation due to the strong localisation of the f states in reduced cerium oxides. In this way it is possible to properly describe both reduced and unreduced cerium atoms. A Hubbard-U term equal to 4.5 eV was chosen to represent the structures in the spin polarized calculations of both CeO_2 and Ce_2O_3.

The DOS is displayed in Fig. 3.11 (right). The calculation was performed with experimental lattice parameter 3.937 Å and with E^{cut}_{rho} 400 Ry, E^{cut}_{wfc} 40 Ry

and k-point mesh (6×6×4) for scf calculation and (12×12×8) in subsequent nscf calculation. Compared to the DOS of ceria, the f states of the cerium atoms in Ce_2O_3 exhibit a peak below the Fermi level present only in one spin. This localisation of the occupation of the f states is a sign of the reduction of the cerium atom from Ce^{4+} state to Ce^{3+} state. The band gap around the Fermi level shows that the reduced cerium oxide has also insulating character.

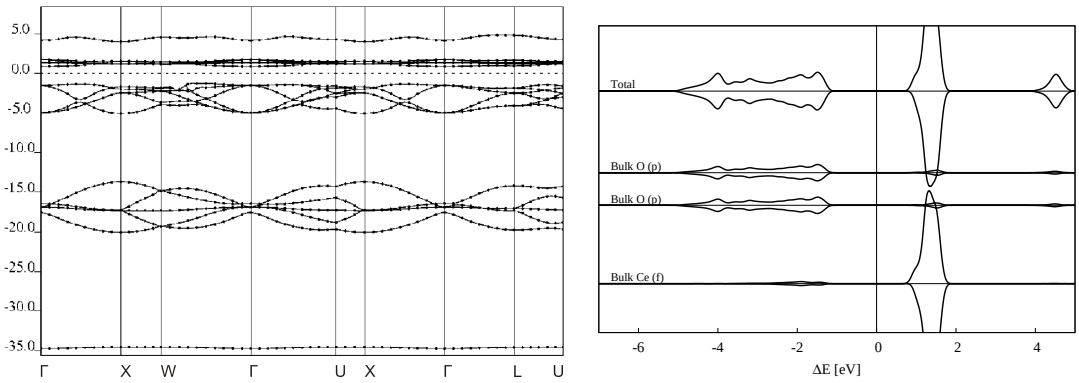

Figure 3.10: **Electronic properties of bulk ceria:** Density of states of a bulk ceria (right) and calculated band structure for ceria along high symmetry directions in Brillouin Zone (left) are presented. Zero energy is set at the Fermi level.

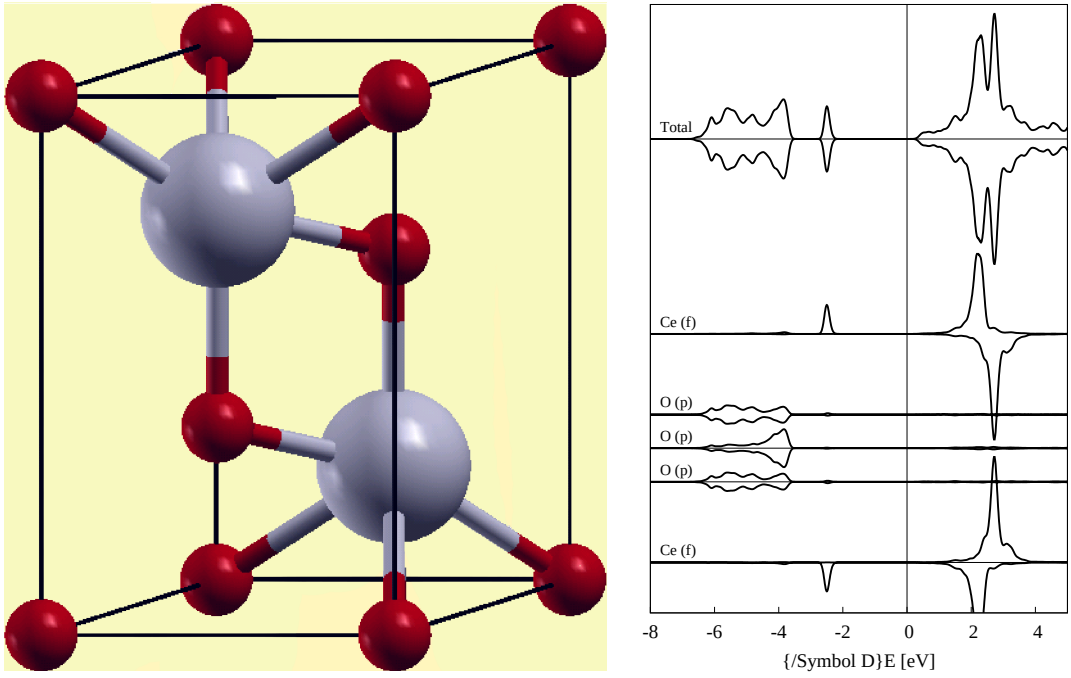

Figure 3.11: **Bulk Ce_2O_3:** The unit cell of the Ce_2O_3 with P-3m1 symmetry is displayed left, the density of states of the Ce_2O_3 molecule is shown right. Zero energy is set at the Fermi level.

3.4 CeO_2 (111) surface

Table 3.2: **Surface energies and relaxations**

	2	3	4	5	6	7
O(1) [Å]	0.03	0.04	0.02	0.02	0.02	0.02
Ce(2) [Å]	0.02	0.02	0.01	0.01	0.01	0.01
O(3) [Å]	0.04	0.03	0.02	0.02	0.02	0.02
O(4) [Å]		-0.01	-0.02	-0.02	-0.03	-0.02
Ce(5) [Å]			-0.01	-0.01	-0.01	-0.01
O(6) [Å]			-0.01	-0.01	-0.01	-0.01
E_{surf}^{scf} [J/m^2]	0.845	0.844	0.843	0.844	0.843	0.844
E_{surf}^{relax} [J/m^2]	0.832	0.836	0.837	0.837	0.836	0.837

We modeled ceria (111) surface with (1×1) supercell, using the lattice parameter and the energy cutoffs for wavefunctions and charge density acquired in previous calculations of a bulk ceria. The supercell consisted of several trilayers of ceria creating two oxygen terminated surfaces separated by 12.1 Å thick layer of vacuum. For the calculations we used supercells with number of trilayers from two to seven.

We studied the effect of surface on the relaxation of the system by relaxing the atoms according to the Helmann-Feynman forces. The relaxation was performed by a set of scf calculations maintained until the force acting on each atom was less than 0.026 eV/Å and the difference between the total energies of the subsequent scf calculations was less than 0.001 eV.

The surface energies were calculated for the systems before and after the relaxation according to the Formula 3.1 and are presented in Table 3.2 together with atomic displacements of the atoms close to the surface (O(1) represents the surface oxygen atom, Ce(2) a cerium atom from the first subsurface layer and so on). The positive values of the displacement represent the shift into the bulk, while the negative values show a movement towards the surface.

The relaxation resulted in shift of the surface ceria trilayer into the bulk, while the subsurface ceria layer moved slightly towards the surface thus decreasing the distance between the surface and subsurface ceria trilayer. The calculated shifts of the surface oxygen 0.02-0.04 Å are in good agreement with reported values 0.02-0.03 Å [43]. The relaxation effects are also similar to those reported in [21]. The calculated surface energies 0.844 J/m^2 for unrelaxed surface and 0.837 J/m^2 for relaxed surface are higher than the results presented in [21, 37]: 0.69 J/m^2 unrelaxed and 0.68 J/m^2 relaxed and also higher than value calculated with GGA in [43] 0.72 J/m^2.

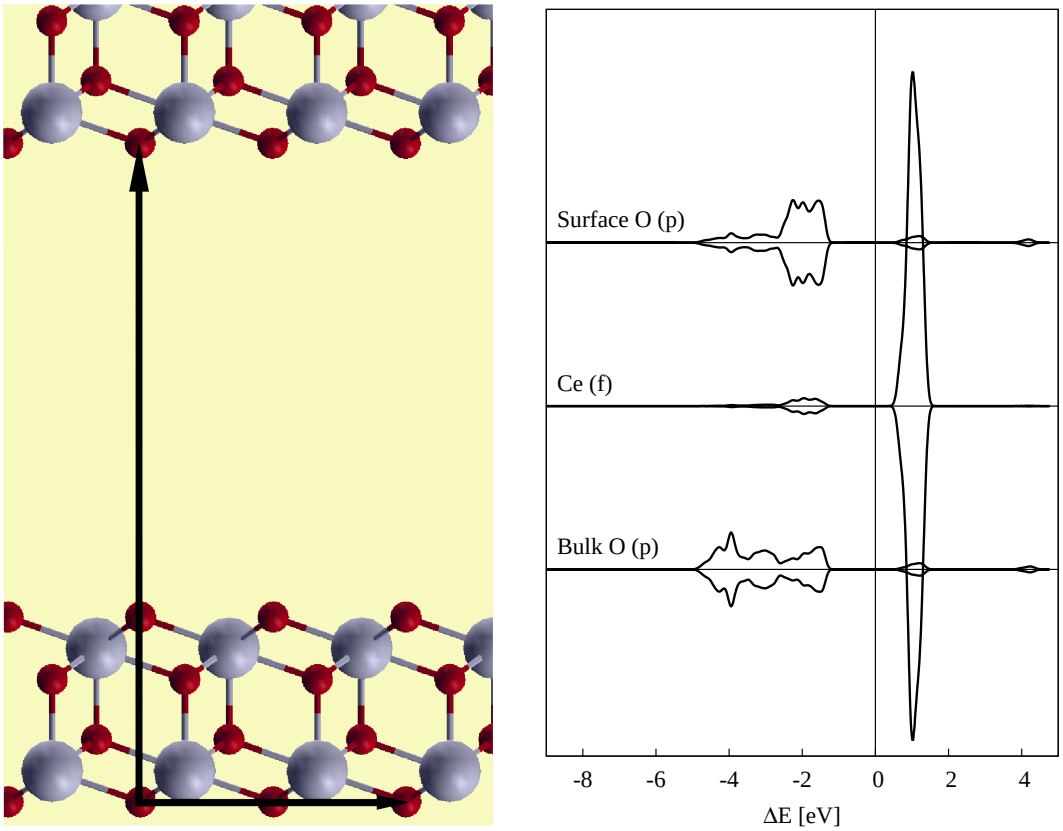

Figure 3.12: **Ceria surface:** (2×2) supercell used in the calculations of ceria surface (left) and the density of states calculated for different ceria atoms (right) are presented. The DOS of the oxygen atom from the surface layer is displayed at the top, the DOS of the cerium atom from the following layer in the middle and the DOS of the oxygen atom from the third layer at the bottom.

For the calculations two types of slab were chosen, slabs with two and three ceria trilayers, in order to maintain reasonable hardware and time computational requirements. The DOS properties of ceria surface were calculated on two types of supercell differing in number of atoms in xy plane. The first type of the supercell had one atom in the xy plane whereas the xy plane in the second supercell was created from (2×2) atoms. The (2×2) supercell is displayed in Fig. 3.12 on the left. In z direction both types of supercell consisted of two layers of ceria molecules and 12.1 Å thick vacuum layer. The sufficiency of the thickness of the vacuum layer was confirmed by a scf calculation of a system with vacuum layer increased to 13.1 Å which resulted in the total energy within 0.001 eV from the previous result.

The k-point mesh was chosen (6×6×1) and (3×3×1) for (1×1) and (2×2) supercell respectively. The system was relaxed with one ceria layer fixed in position and the other relaxing until the force acting on each relaxing atom was less than 0.026 eV/Å. The density of states was calculated with k-point mesh (12×12×1) and is displayed in Fig. 3.12 on the right. For the DOS graph we chose to show the DOS of one oxygen atom from the surface layer (up), the DOS of the cerium atom in the following layer and the DOS of the oxygen in the middle layer (down).

Chapter 4

Cu adatoms supported on CeO_2 (111)

In this Chapter I will focus on the bonding of copper adatoms on oxidized and reduced (111) ceria surfaces. In particular, I will explore the structural and electronic modifications induced at the metal/oxide contact, where opposite charge transfer effects are predicted depending on the stoichiometry of the support. When the Cu adatom is supported by the O-terminated clean (111) CeO_2 surface, two possible configurations are identified. These are very close in energy and display slightly different bonding properties. In any case, for both of them the calculations predict a net charge transfer from the metal to the oxide surface, resulting in a supported Cu cation.

On the opposite, when the Cu atom adsorbs on the reduced (111) CeO_2 surface (which we model by including an O vacancy in the simulation supercell) only one very stable configuration is predicted and the charge is transferred from the oxide to the metal atom, creating a supported Cu anion. In addition, the adsorption of a Cu adatom on the (111) CeO_2 surface always involves the presence of a reduced Ce^{3+} ion in the neighborhood of the adatom, both when the Cu is a cation and an anion.

4.1 Previous studies

Some of the most efficient catalysts are composed of metal particles deposited on oxide supports. The activity of the catalyst can be influenced by the choice of the support and the metal as well as the size of the metal clusters. Several experiments were carried out with different substrates such as MgO, TiO_2, and CeO_2 in combination with different supported metals as Au, Pd or Pt. Calculations were conducted on such systems as well[57, 58, 59, 56, 55], often in combination with the above mentioned experimental studies. Among the substrates ceria surface is highly valued because of its oxygen storage capacity.

Yang and coworkers investigated the properties of Pd and Pt[55, 56] adatoms on ceria surfaces as well as their influence on the oxygen storage capacity by the means of DFT calculations. In [55] the DFT+U study of palladium adatoms on ceria surface was reported. Different adsorption features were found on reduced

and unreduced ceria surfaces.

As a most preferable adsorption site of Pd adatoms on unreduced stoichiometric ceria surface the bridge-like site between two oxygen atoms was stated. The electronic-structure changes for these systems with adsorbed Pd adatom were reported including metal induced gap states. These were identified by comparing the DOS of the metal/oxide system with the DOS of the non-interacting systems, namely the clean ceria surface and the bulk Pd. Those states were discovered to arise from contribution of Pd 4d, O 2p and Ce 4f states, the former two accounting for Pd-O bonding. The oxygen 2p gap states induced by Pd adsorption increase the activity of the system. This study also report the charge transfer from the Pd adatom to the surface. In the process, the excess charge localizes near the adsorption site.

The vacancy formation after the Pd adsorption was studied as well as the adsorption of Pd adatoms on the reduced surface with oxygen vacancies. The stronger bonding between Pd adatom and the reduced ceria surface was discovered in comparison to the bonding of Pd and unreduced ceria surface. The energetics revealed that, in the presence of an adsorbed Pd adatom, the oxygen vacancy formation energy is reduced by 0.4-0.6 eV with respect to the oxidized surface value. It is shown that the metal induced gap states of the system with Pd adatom on the reduced ceria surface are sharper and partially occupied, which causes them to be able to accept electrons and increase oxygen storage capacity of ceria surface.

A similar DFT+U study analyzes the case of platinum adatom on the reduced and unreduced ceria surfaces, as reported in [56]. In this system, the most stable adsorption site of Pt adatom was found in the proximity of the bridge between two oxygen atoms. The predicted ground state for the Pt adsorbed on the oxidized ceria surface is spin unpolarized. The study reports the appearance of metal induced gap states in DOS of the system upon Pt adsorption. The extra gap states arise from the Pt 5d, O 2p and Ce 4f states. In addition, the work also consider the activity of the Pt/ceria system, which is reported to be increased with respect to the pure ceria surface. The charge density redistribution analysis revealed bonding between Pt adatom and two bridge oxygen atoms and between Pt and the nearest neighbour cerium atom. The charge transfer from Pt adatom to the surface was observed as well.

The properties of the Pt adatoms supported on a reduced ceria surface were studied as well. Also in this case the authors reported the formation of a stronger bond between the Pt adatom and the reduced surface compared with the Pt adsorption on stoichiometric ceria surface. Most importantly, the work shows the effect that supported Pt adatoms have on decreasing the oxygen vacancy formation energy. This has clearly important catalytic implications via amplification of the oxygen storage capacity of ceria surface.

Zhang and coworkers were studying effects of gold adsorption on ceria surfaces [57, 58]. Density functional theory was used in the calculation within the GGA+U approximation. The adsorption of Au adatoms on different adsorption sites was studied focusing on gold adatom on top of surface oxygen atom and gold adatom in the bridge position between two surface oxygen atoms. The differences between the bonding were described as follows.

The bonding of the Au adatom on top of the oxygen on stoichiometric ceria surface was determined as a result of an overlap between the oxygen p orbitals with the gold d orbitals. The occupation of originally empty cerium 4f states below the Fermi energy was discovered. The Au oxidation is suggested as well as localisation of 4f electrons on the cerium atom in the nearest neighbour position of the Au adatom thus causing its reduction.

The bridge site is predicted to be the the most stable adsorption site also for the case of Au adatoms. The energy level of the filled 4f Ce states in the bridge configuration were discovered to be at the lower energy than in the top adsorption site. The f electron is reported to localize on the third nearest neighbour cerium atom with respect to the adsorbed gold atom. The bonding of the gold adatom is a result of an overlap of oxygen p states with gold d states similarly like for the top configuration, but mostly with broader overlap which suggests stronger bonding. The oxidation of the Au adatom to the larger degree in the bridge site than in the top site is reported.

The most stable adsorption position of Au adatom on reduced ceria surface with oxygen vacancies is presented as the position on top of the vacancy. The bonding of the gold adatom at the vacancy location includes transfer from one of the two cerium atoms reduced due to the oxygen removal to the gold adatom s states showing opposite behaviour in comparison with gold adsorption on stoichiometric ceria surface. A strong ionic bond was discovered between the gold adatom and the surrounding cerium atoms. The calculations suggest that gold adatoms do not substantially modify the energy for O vacancy formation on ceria surface.

The adsorption of gold atom in the place of cerium vacancy at the cerium surface was studied as well. In this case, the calculations did not predict any reduction of the cerium atom in the supercell. The adsorption energy of gold atom at Ce vacancy was found out to be larger than adsorption energies for reduced and stoichiometric surfaces. Although when taking vacancy formation in account, the gold adsorption on stoichiometric surface proved to be most favorable followed by adsorption at the Ce vacancy.

These results were confirmed by the calculations reported in [59]. In addition, this work address the reaction mechanisms for CO oxidation activated by gold adatoms and clusters supported on ceria surfaces, as well as by AuCeOx solid solutions.

4.2 Calculation details

The ceria surface was modeled by a hexagonal (2×2) computational supercell comprising tree CeO_2 tri-layers in the following sequence O-Ce-O-O-Ce-O-O-Ce-O. This results in an oxygen terminated surface. As discussed in the previous Chapter we have analyzed in dept the structural properties of the surface performing atomic relaxations according to several methods. A first set of calculations in which all atoms were relaxed except from the center ceria trilayer fixed at the bulk position. In a second set of calculations we checked this model by relaxing all atoms except those in the bottom half of the supercell, which were

constrained at their bulk-like position.

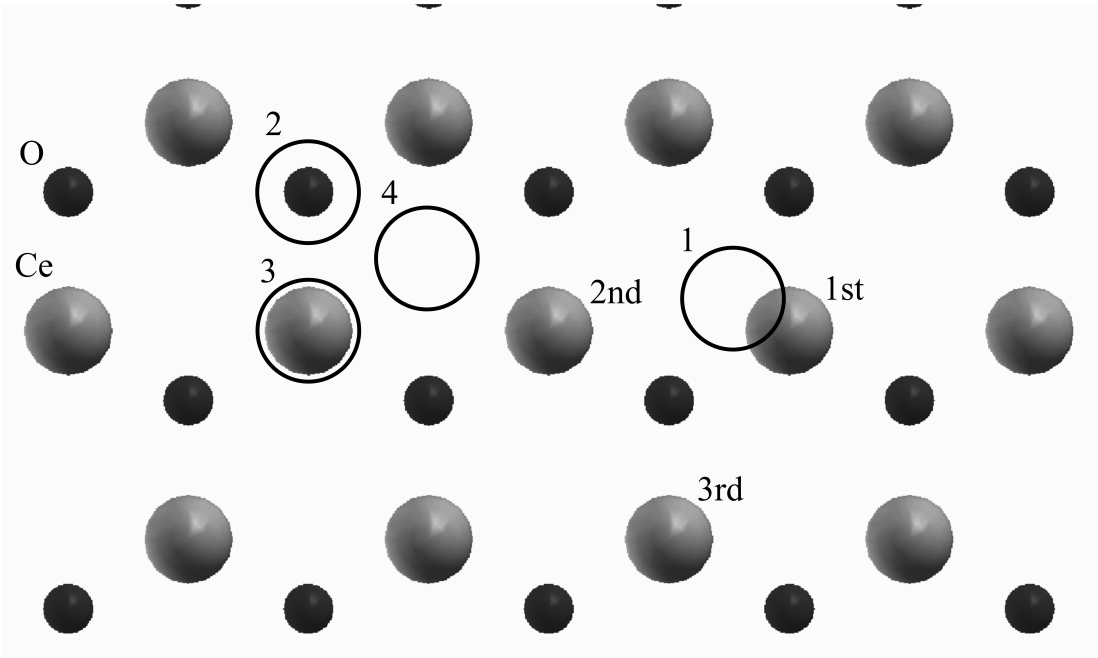

Figure 4.1: **Adsorption sites of a copper adatom on (111) ceria surface.** The small red full circles represent first layer of oxygen atoms and the bigger grey full circles stand for the underlying layer of cerium atoms, whereas the black empty circles show main adsorption sites of the copper adatom on ceria surface. The site labeled "1" is a bridge position between two oxygen atoms, while the position with copper adatom on top of one of the oxygen atoms is labeled as "2". The other two positions represent different possibilities of the copper adatom in the hollow site of three oxygen atoms. The labels "1st", "2nd" and "3rd" show out different positions of reduced cerium atom with respect to the bridge adsorption site.

A copper adatom was placed on different adsorption sites on the relaxed ceria surface. These positions are displayed in Fig. 4.1, "1" represents copper in a bridge position between two oxygen atoms, "2" stands for copper on top of oxygen atom and "3" and "4" are the two different positions where copper is placed in the hollow site of three oxygen atoms.

Next the system with the copper atom in an oxygen vacancy was examined. The system was prepared by removing one of the surface oxygen atoms from ceria slab thus simulating a reduced ceria surface and placing the copper atom at the exact coordinates of the removed oxygen atom.

The structural relaxations were performed for all the systems described above, that is for all the possible configurations of the Cu adatom in the high-symmetry adsorption sites , as well as for the system with the copper atom in the oxygen vacancy. The bottom O-Ce-O-O- layers were fixed in position during relaxation. The relaxation and all the following calculations were performed with E_{rho}^{cut} and E_{wfc}^{cut} 300 and 30 Ry respectively. Hubbard U term of 4.5 eV was used in calculations of cerium atoms, and all calculations in this Section were spin polarized.

The k-point mesh was fixed to (2×2×1) Monkhorst-Pack grid containing 8 independent k-points for the relaxation and self consistent calculations while for the post-processing calculation performed to calculate the DOS properties of the system the k-point mesh 8x8x1 consisting of 68 independent k-points was used. properties therefore the curves in one DOS figure are not proportional.

The adsorption energies of the above-mentioned Cu/CeO_2 systems were calculated in terms of the total energies of the individual interacting and non-interacting systems. These were obtained from the scf calculations of *i*) the complete system (the Cu adatom adsorbed on ceria surface), *ii*) of a single Cu atom isolated in vacuum, and *iii*) of the clean surface corresponding to the complete system (reduced or oxidized). This is summarized in the following equation 4.1, where E_{ads} is the adsorption energy, $E^{TOT}_{CeO_2/Cu}$ is the total energy of the system of the copper atom adsorbed on ceria surface, $E^{TOT}_{CeO_2}$ is the total energy of ceria surface and E^{TOT}_{Cu} is the total energy of a single copper atom.

$$E_{ads} = E^{TOT}_{CeO_2/Cu} - (E^{TOT}_{CeO_2} + E^{TOT}_{Cu}) \tag{4.1}$$

The bonding charge density analysis was calculated with the same spirit, namely by determining the charge difference between the charge density of the complete system with copper adatom on ceria surface ($\rho_{CeO_2/Cu}$), and the combined density of the the isolated non-interacting systems of copper (ρ_{Cu}) and ceria surface (ρ_{CeO_2}). This is defined in the following expression 4.2.

$$\Delta\rho = \rho_{CeO_2/Cu} - (\rho_{CeO_2} + \rho_{Cu}) \tag{4.2}$$

4.3 Results

Table 4.1: **Adsorption energy**

	BRIDGE	TOP
E_{ads} [eV]	-2.97	-2.21
ΔE [eV]	-	0.76

The relaxation of the four configurations of the system revealed one stable and one metastable configuration of the copper atom on ceria surface, the bridge (position "1" in Fig. 4.1) and the top (position "2" in Fig. 4.1) respectively. The remaining two hollow positions relaxed to the previous positions: the hollow "3" to the top site, while the hollow "4" to the bridge site. In the following Sections we describe each metastable system separately. Then in the last Chapter we examine the bonding properties of the relaxed system with the copper atom in the oxygen vacancy.

4.3.1 Bridge

The most stable system was predicted to be the one with copper in the bridge site since it is 0.76 eV lower in energy than the system with copper in the top

Table 4.2: **Changes in bondlengths during the relaxation.**

	BRIDGE		TOP	
	unrelaxed	relaxed	unrelaxed	relaxed
Cu-O [Å]	2.2	1.91	1.8	1.76
Cu-Ce [Å]	2.9	2.73	3.5	3.68

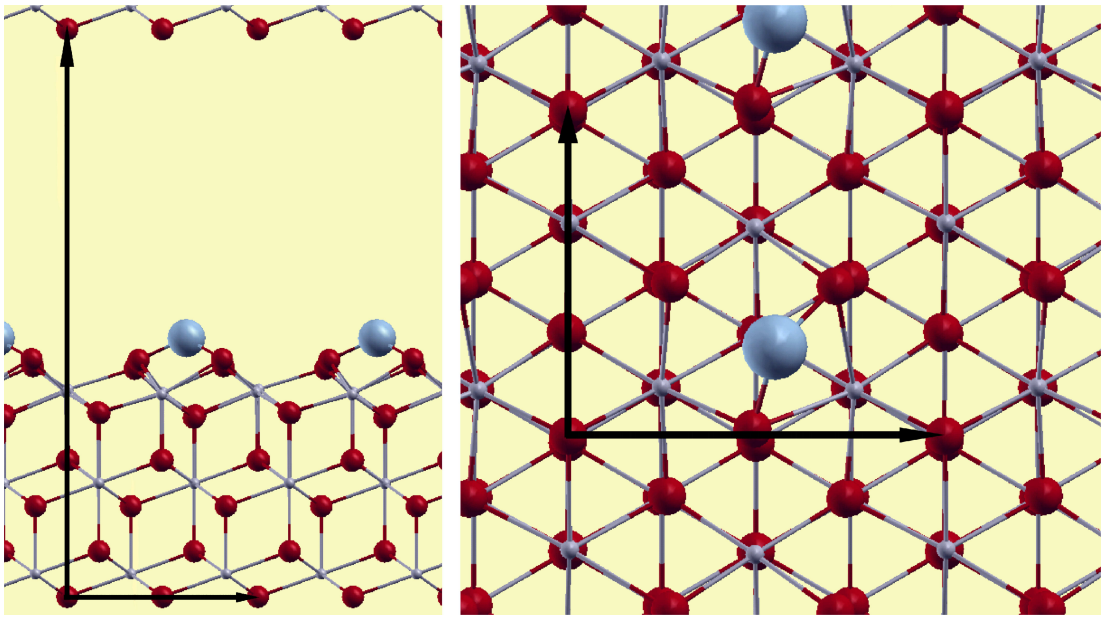

Figure 4.2: **The supercell of a system with the copper adatom in the bridge adsorption site of ceria surface.** A side view (left) and a top view (right) of the supercell used in the calculations concerning the system with the copper atom in the bridge adsorption site is displayed after the relaxation. The red (dark) circles represent the oxygen atoms, the big grey circles are the copper adatoms and the little grey circles show the positions of the cerium atoms.

site. The adsorption energy of a copper adatom at the bridge site was calculated as 2.97 eV.

For the bridge configuration we started by placing the copper adatom to the bridge adsorption site of two oxygen atoms to the distance 2.2 Å from both, which is slightly more than the length of Cu-O bond length in copper oxide Cu_2O [89]. The distance of the copper adatom and the nearest cerium atom before the relaxation was 2.9 Å. During the relaxation both the Cu-O bond lengths decreased to 1.91 Å as a result of two effects, firstly the copper adatom moved towards the surface for 0.17 Å and secondly both the oxygen atoms creating the bridge shifted towards the copper adatom thus elevating from the first oxygen layer for 0.3 Å. As the result of the first effect Cu-Ce distance decreased to 2.7 Å as well. The relaxed supercell used in the calculations is displayed in Fig. 4.2.

The bonding charge analysis was performed and the results are presented in Fig. 4.3. Fig. 4.3 (right) displays a side view to the system, the charge density difference is drawn in equipotential for an isovalue of $|0.02|$ $e^-/Å^3$. Red color represents accumulation of the charge density, blue color stands for depletion of

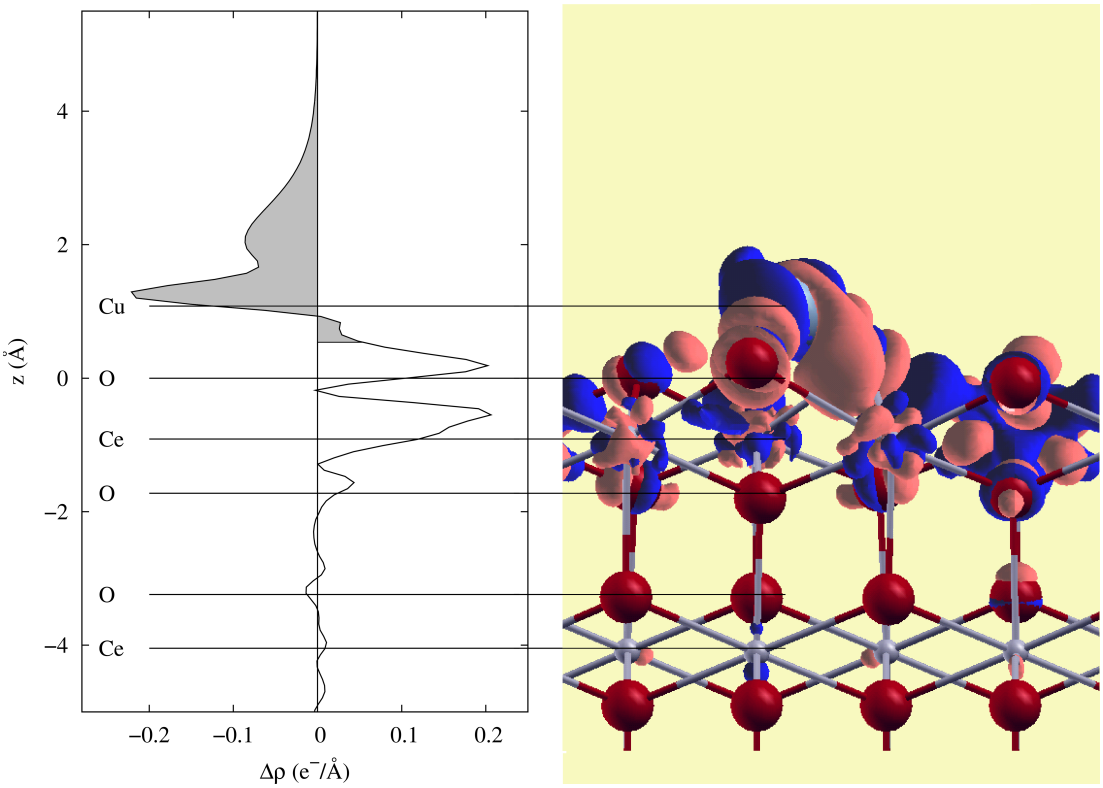

Figure 4.3: **Bonding charge of the copper adatom in the bridge adsorption site of ceria surface.** A side view at the system with a charge density difference in equipotential planes at the value $|0.02|$ $e^-/Å^3$ is displayed on the right. The red color represents gain and the blue color loss in charge density. On the left the charge density difference is integrated at the xy planes and plotted along the z direction.

the charge density.

The values were integrated over planes parallel to the surface - this is shown in graph on the left side of Fig. 4.3. This independent analysis clearly shows the charge depletion around the copper site and the charge accumulation both in the bonding region and at the first layer of cerium atoms, which suggests that a charge transfer occurs from copper adatom to ceria surface creating positively charged copper ion and reducing one of the cerium atoms. Further integration along z direction in the range from the middle of Cu-O bond to the middle of the vacuum layer provided the value of 0.2 e^- which provides a relative measure (it is not an absolute value) of the charge transferred from Cu adatom to ceria substrate, and will be used for comparison with other systems.

From Fig 4.3 (right) it appears that the charge transferred from the copper adatom localizes partly on the reducing cerium ion and partly on the two bridging surface oxygen atoms that are bound to the Cu adatom. The bonds are visible mostly between the copper and the oxygen atoms, but also some changes in the charge density can be observed along the shortest Cu-Ce bond.

The reduction of the one particular cerium atom was verified by charge population analysis displayed in Table 4.3, where it is apparent that in comparison

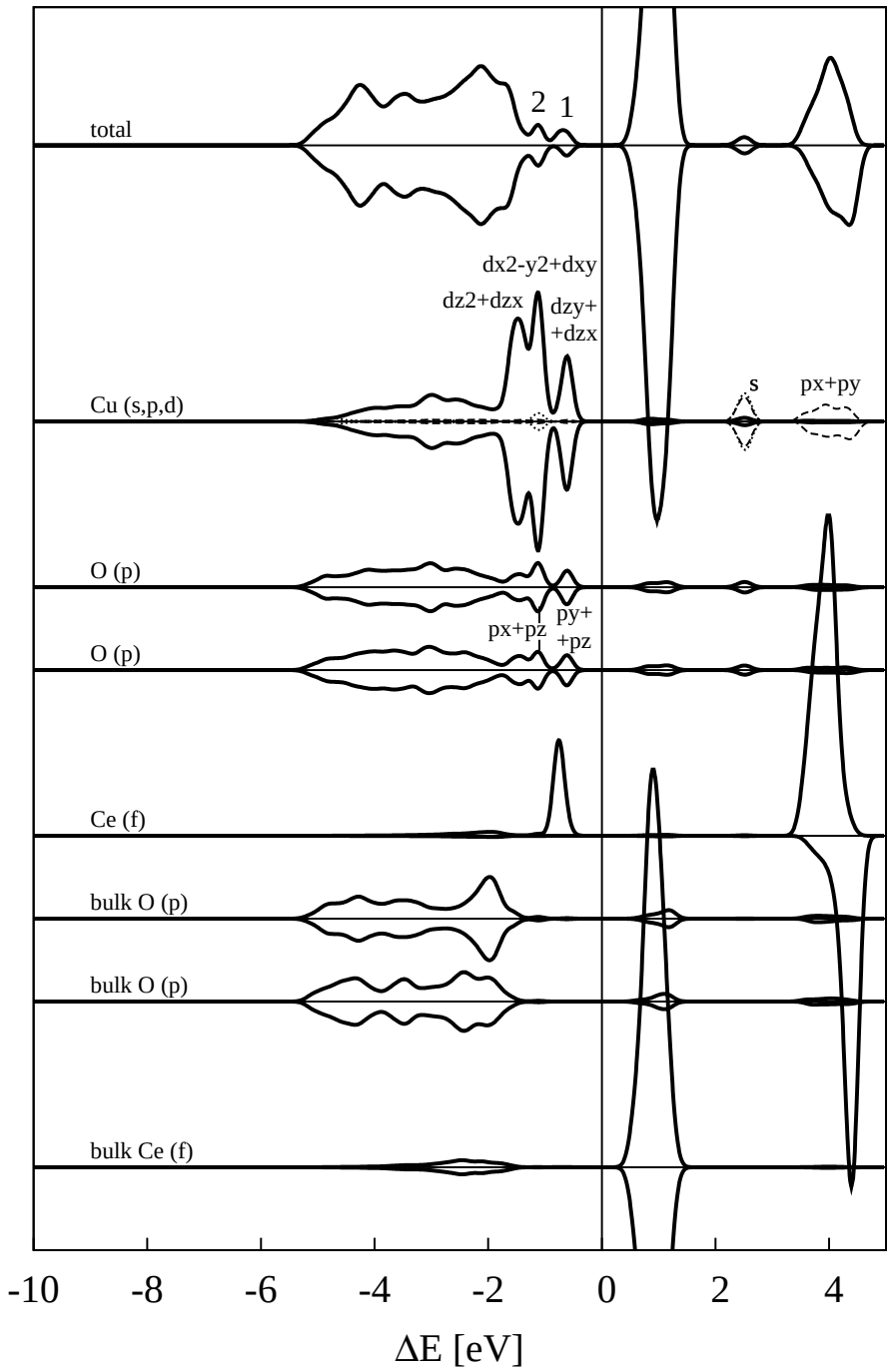

Figure 4.4: **The density of states of the system with copper adatom in the bridge adsorption site of ceria surface.** The density of states was projected on different atoms in the system. The total DOS is displayed at the top of the figure. Folowing curves represent orbitals of copper adatom, two bridging oxygen atoms in surface layer of ceria slab, cerium atom from the underlying layer, oxygen atoms from the third and fourth layer and cerium atom from the fifth layer, describing from the upper curve to the bottom.

Table 4.3: **Charge population analysis of the system with the copper adatom at the bridge adsorption site.** We display the charge population analysis for the atoms involved in the bonding of the copper adatom on the surface as well as some of the other for comparison.

	Total	s	p	d	f
Ce reduced	10.8180	2.2544	5.9565	1.4863	1.1207 (1.0572-0.0635)
Ce unreduced	10.8190	2.2719	5.9538	1.8633	0.7299 (0.3650-0.3649)
O bridge	6.5789	1.7202	4.8587	–	–
O bridge	6.5852	1.7201	4.8651	–	–
O other	6.5457	1.7085	4.8372	–	–
Cu	10.9078	0.5223	0.7181	9.6675	–

with one of the unreduced cerium atoms, in the reduced one the f states are more occupied. Most importantly the occupation of the 14 f states of the one particular cerium atom is divided between the spin up and down unevenly unlike the case of all of the other cerium atoms in the slab. One of the spins has occupation equal to one electron while all other 13 states are almost unoccupied, which causes spin polarisation of one electron and confirms the reduction of the cerium atom.

In Table 4.3 the charge population analysis of both oxygen atoms creating the bridge are displayed as well as one of the other oxygen atoms for comparison. At the s and p states of the bridge oxygen atoms a indication of increase of population appears, suggesting the localisation of a part of charge transferred from the copper adatom. The low charge population of the copper s states confirms the positive charging of the copper adatom. The excess p states were caused by an effect of oxygen p states which are larger in comparison to the narrow copper states.

Tests were performed to force the discovered reduction on different cerium atoms. We were able to reach self consistent solution for reduced Ce^{3+} atom localized as the first, second or third nearest neighbour, where the last case proved to be the system with lowest energy. The other reached solutions differed in energy for 0.39 and 0.19 eV respectively. The first, second and third nearest neighbour cerium positions for the system with the copper adatom in bridge position are labeled in Fig. 4.1 as "1st", "2nd" and "3rd".

The density of states for different atoms in the system is displayed in Fig. 4.4. In contrast with density of states calculated for isolated ceria surface or isolated bulk copper atom, the density of states for the complete system show out two extra features below the Fermi level (labeled "1" and "2" in the figure). The projected density of states analysis revealed that the bonding of an adatom on the substrate originates from the bonds between copper and the two bridging oxygens. The bonding, whose energy levels are responsible for the features "1" and "2", is a result of an overlap of copper d orbitals (in particular dzy and dzx orbitals) with p orbitals of both bridging oxygens (px and py). This hybridization confers a partial covalent character to the bonding in addition to the electrostatic contribution due to the charge transfer. In the same energy region of feature "1" lies the peak at the cerium DOS curve originated from a localisation of an electron on the f orbital of cerium during the reduction of Ce^{4+} ion to Ce^{3+} ion, which also confirms previous findings acquired from the bonding charge analysis and

the charge population analysis.

The overlapping of quite low and flat orbitals suggests, that the Cu-O bonding has mostly covalent character with a ionic contribution of sharp cerium f orbital.

The magnetisation of the system was determined as 1.15 μ_B which corresponds to the one unpaired electron in Ce f state.

4.3.2 Top

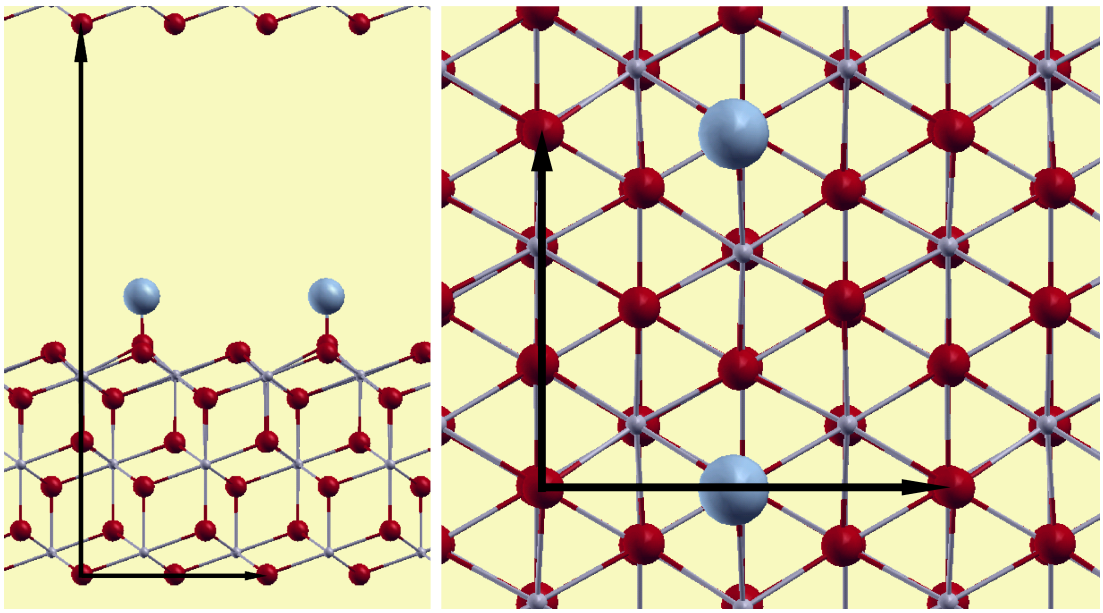

Figure 4.5: **The supercell of the system with the copper adatom in the top adsorption site of ceria surface.** A side view (left) and a top view (right) of the supercell used in the calculations concerning the system with the copper atom in the top adsorption site is displayed after the relaxation. The red (dark) circles represent the oxygen atoms, the big grey circles are the copper adatoms and the little grey circles show the positions of the cerium atoms.

The adsorption energy of a Cu atom in the top metastable site is 2.21 eV, 0.76 eV higher than the adsorption energy of the system with copper at the bridge adsorption site.

The relaxation of the system, where the copper adatom was put on top of the surface oxygen atom to a distance 1.84 Å, caused the shift of the copper adatom in the direction away from the surface for 0.25 Å. However the relaxation effects on ceria surface involve also the movement of the oxygen atom closest to the copper adatom apart from the first oxygen layer for 0.3 Å, thus the Cu-O bond length decreased from 1.84 Å to 1.75 Å. The distance of the copper adatom from the three nearest cerium atoms increased from 3.5 Å to 3.7 Å. The supercell used in the calculations of the system with the copper adatom in a bridge adsorption site is displayed in Fig. 4.5.

The bonding charge was calculated as described in Section **4.2** and is displayed in Fig. 4.6. The integration over the xy planes was performed and plotted to the

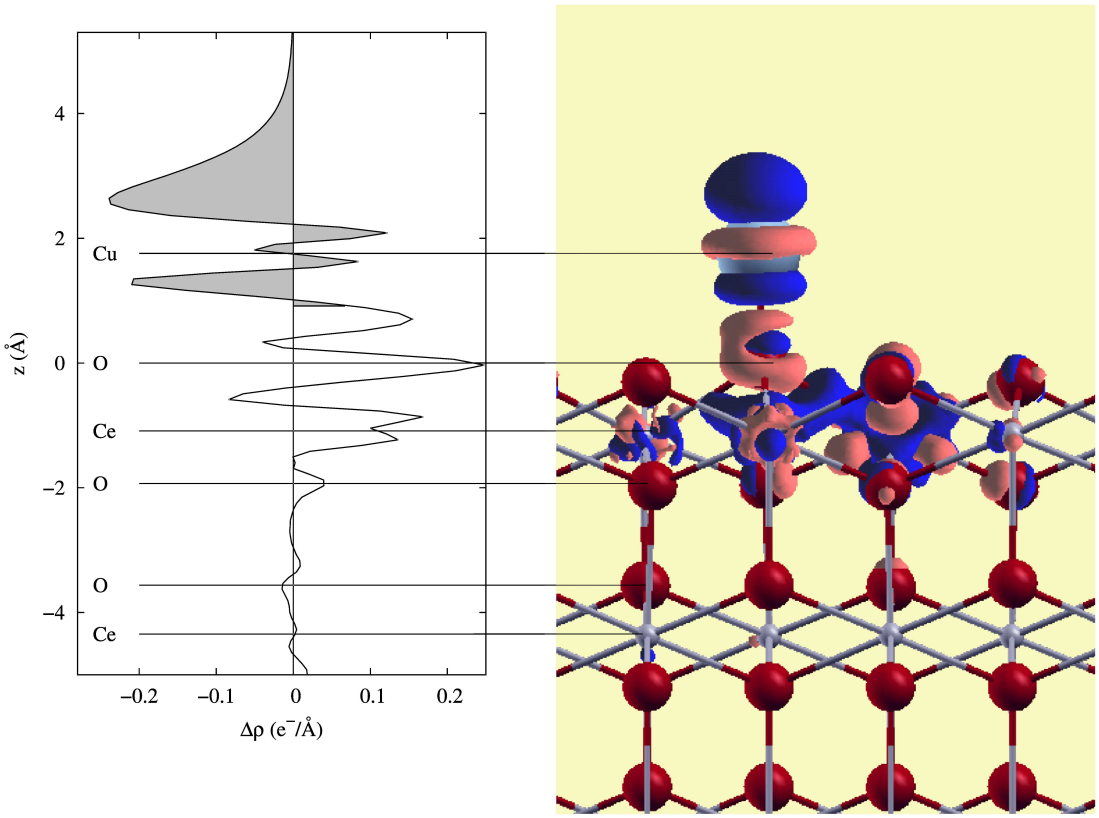

Figure 4.6: **Bonding charge of the copper adatom in the top adsorption site of ceria surface.** A side view at the system with a charge density difference in equipotential planes at the value $|0.02|$ $e^-/Å^3$ is displayed on the right. The red color represents gain and the blue color loss in charge density. On the left the charge density difference is integrated at the xy planes and plotted along the z direction.

left side of the figure. Overall it reveals that the same physics govern the formation of the Cu-O bonding namely charge transfer to the nearest O atoms and to one Ce site, but involving different orbitals, mostly oriented along the z direction

In the direct proximity of copper adatom there is not so strong charge depletion as in previous case. Although by the integration along the z direction from the middle of Cu-O bond to the middle of the vacuum layer, the value of 0.27 e^- was obtained, which is higher than in the system with copper in the bridge adsorption site. This result confirms that in this configuration the charge transfer from copper adatom to ceria surface occurs and the positively charged copper ion is created.

The charge accumulation is apparent at the level of the first oxygen atoms as well as at the next cerium layer. This accumulation and the right side of Fig. 4.6 suggests reduction of cerium Ce^{4+} ion to Ce^{3+}. The charge transferred from copper to ceria localize on this reduced cerium ion and on the oxygen creating the bond with copper. The changes in the charge density around this copper, oxygen and the cerium atom as well as around the Cu-O bond are also visible at the right side of the Fig. 4.6.

The charge population analysis displayed in Table 4.4 confirm the positive

Table 4.4: **Charge population analysis of the system with the copper adatom at the top adsorption site.** We display the charge population analysis for the atoms involved in the bonding of the copper adatom on the surface as well as some of the other for comparison.

	Total	s	p	d	f
Ce reduced	10.8701	2.2542	5.9562	1.5460	1.1137 (1.0462-0.0675)
Ce unreduced	10.8211	2.2738	5.9537	1.8657	0.7280 (0.3641-0.3638)
O bonded	6.5598	1.7015	4.8583	–	–
O other	6.5147	1.7094	4.8053	–	–
Cu	10.8017	0.6952	0.3769	9.7296	–

charging of the copper adatom and the reduction of cerium ion. The analysis specifies that the charge transferred from copper adatom visible as low occupation of the copper s state localizes particularly on p states of the oxygen and the up spin of the f state of the reduced Ce^{3+} ion similarly as in previous case.

The density of states analysis of this case turned out to be more straightforward than the previous case, although here as well as in the previous case two new features appear. The bonding between copper and the oxygen atom is composed of covalent and ionic components. The overlap of copper dzx and dzy orbitals with oxygen px and py orbitals and the overlap of the copper dz2 and oxygen pz orbitals both contribute to the covalent part of the bond. The latter create the feature "2" located at the bottom of the valence band. The sharp peak of copper dxy and dx2-y2 orbitals and the Ce f peak near the Fermi level represent the ionic part of the bond. The Ce f orbital resulted from localisation of an electron during cerium reduction and caused arising of a feature "1". The orbital is located at lower energy than the corresponding peak in the bridge system.

The one unpaired electron in the Ce f orbital is responsible for the magnetisation of system determined as 1.20 μ_B.

4.4 Copper at surface O vacancy

We have studied the Cu/CeO2 system in which, differently from the previous systems, a surface oxygen atom is missing, thus simulating a reduced ceria surface. The self-consistent calculation performed on the reduced ceria surface after the removal of one surface oxygen atom showed reduction of two cerium atoms surrounding the vacancy. The copper atom was placed at the exact coordinates of the removed oxygen atom and the system was relaxed and explored with regard to the bonding properties. The supercell of the system is displayed in Fig. 4.8. The adsorption energy of this system is -1.88 eV, which is 1.09 eV less favorable than the most stable bridge adsorption site.

The relaxation of the system resulted in outward displacement of the copper atom above the surface oxygen layer, reaching a distance of 1.22 Å. The shortest Cu-O bonds do not include the oxygen atoms in the first surface but they involve the oxygen atoms in the third atomic layer of ceria slab. The bonds increased by 0.7 Å to 3.3 and 3.5 Å which was caused by the elevation of the copper atom.

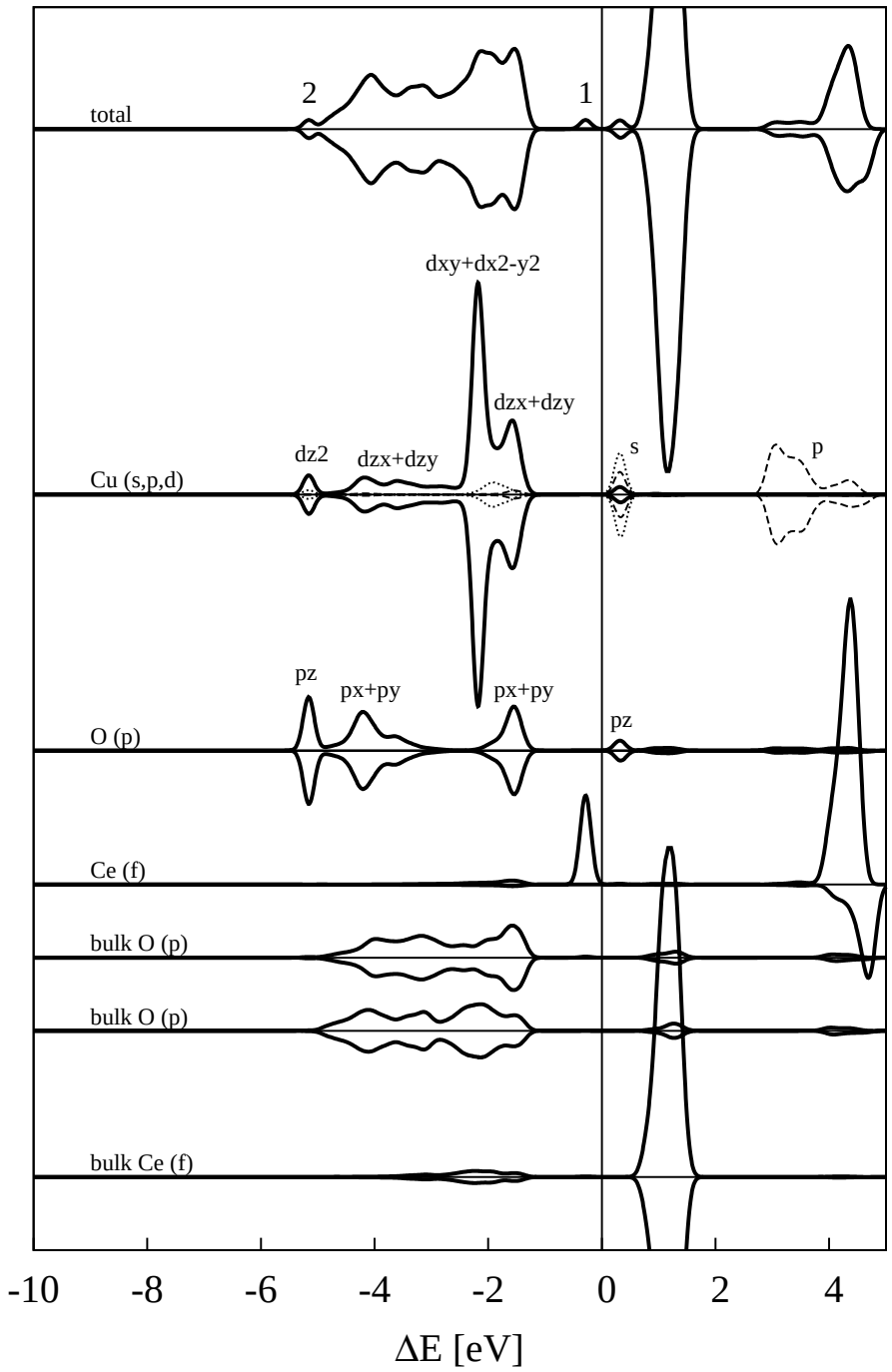

Figure 4.7: **The density of states of the system with copper adatom in the top adsorption site of ceria surface.** The density of states was projected on different atoms in the system. The total DOS is displayed at the top of the figure. Following curves represent orbitals of copper adatom, oxygen atom in surface layer of ceria slab creating the bond with copper, cerium atom from the underlying layer, oxygen atoms from the third and fourth layer and cerium atom from the fifth layer, describing from the upper curve to the bottom.

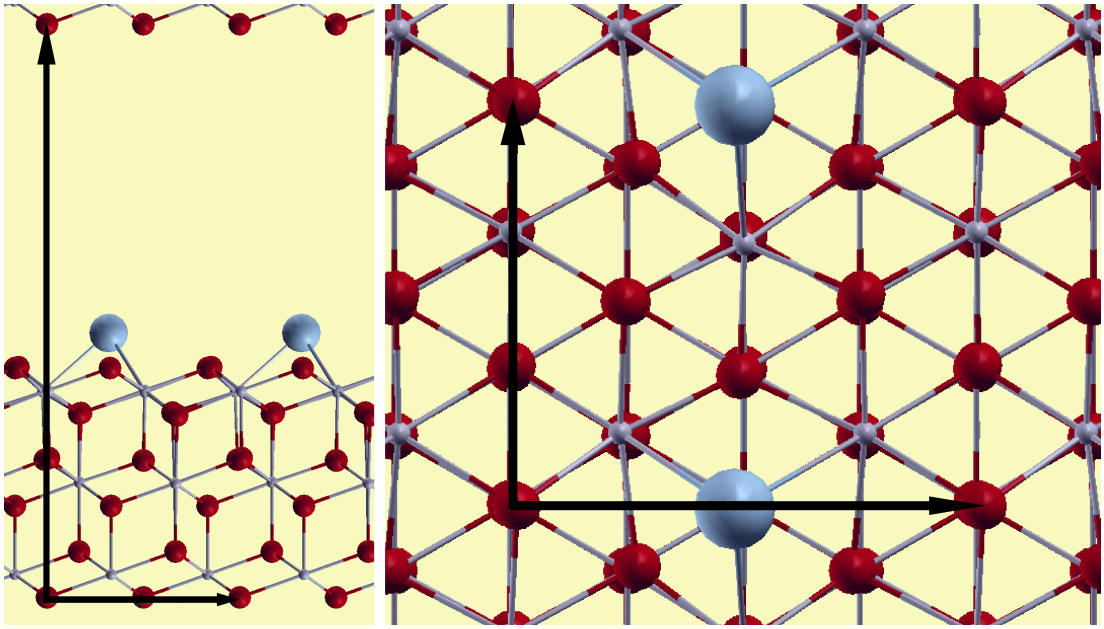

Figure 4.8: **The supercell of the system with the copper adatom in the oxygen vacancy of the reduced ceria surface.** A side view (left) and a top view (right) of the supercell used in the calculations concerning the system with the copper atom in the oxygen vacancy is displayed after the relaxation. The red (dark) circles represent the oxygen atoms, the big grey circles are the copper adatoms and the little grey circles show the positions of the cerium atoms.

The oxygen atoms from the previously mentioned shortest Cu-O bonds shifted towards the copper atom both in the z direction and the x-y plane, the former occurred by elevation of the oxygen atoms for 0.07 Å. On the contrary the cerium atoms moved only in x-y plane away from the copper atom. The Ce-Cu distances increased during the relaxation for 0.8 Å to 3.1 and 3.2 Å. Also the surface oxygen atoms showed slight movement towards the copper atom.

The bonding charge analysis was performed as described in the Section **4.2**. Fig. 4.9 (right) displays the side view to the system with the bonding charge drawn in equipotential planes at the value $|0.04|$ $e^-/Å^3$. On the left side of Fig. 4.9 the curve displaying the redistribution of the charge density along the z axis is shown.

In contrast with the previous cases of adsorption on the unreduced stoichiometric ceria surface, the adsorption on the reduced ceria surface with oxygen vacancies presented different bonding properties. At the integrated curve in Fig. 4.9 (left) the charge accumulation appeared near the copper atom between the copper atom and ceria surface. This accumulated charge was transferred from the cerium layer, where the charge depletion is apparent. The amount of charge transferred from the cerium atoms towards copper 0.26 e^- was acquired by integrating the curve from the level of the oxygen layer to the middle of the vacuum layer. This suggests the creation of a negatively charged copper ion and positive charging of the atoms at the cerium level which is supported by the bonding charge analysis in the right sub-figure of Fig. 4.9. In the figure, the changes in the

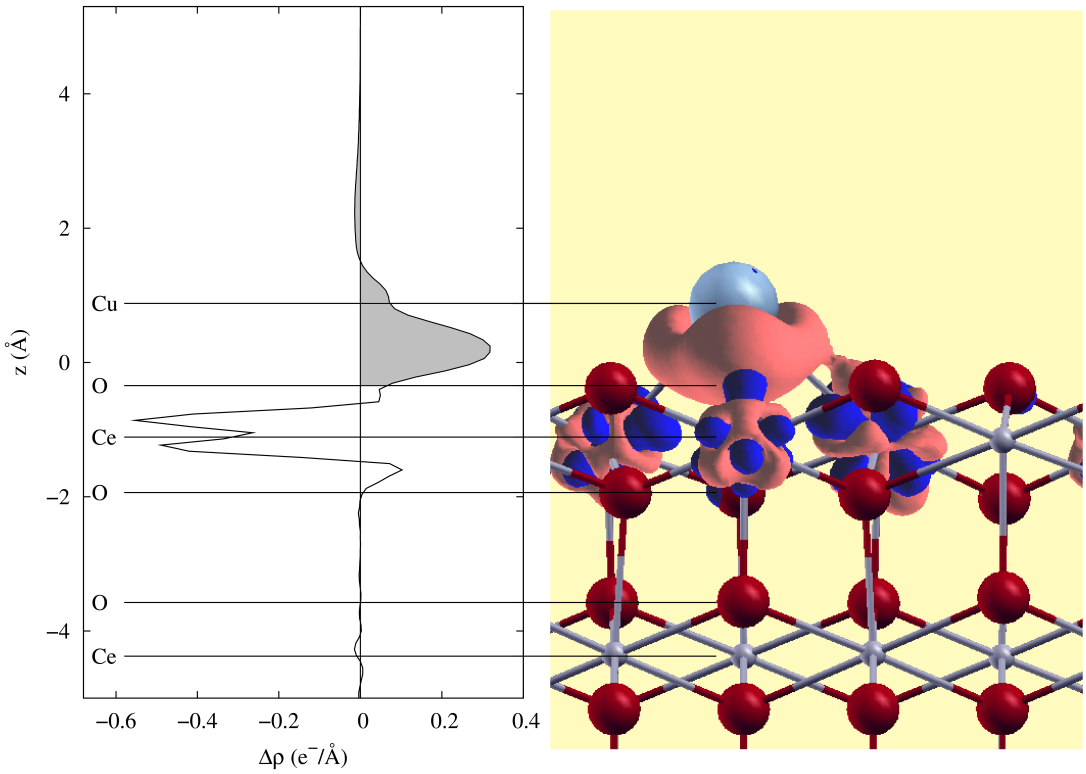

Figure 4.9: **Bonding charge of the copper atom in the oxygen vacancy.** A side view at the system with a charge density difference in equipotential planes at the value $|0.04|$ $e^-/Å^3$ is displayed on the right. The red color represents gain and the blue color loss in charge density. On the left the charge density difference is integrated at the xy planes and plotted along the z direction.

charge density are visible between the copper atom and the cerium atoms, at the three cerium atoms closest to the copper atom and slightly on the oxygen atoms at the first and third atomic layer of ceria slab. The bond between the copper atom and one of the cerium atoms can also be observed.

The charge population analysis presented in Table 4.5 confirms the previous findings about the negative charging of the copper atom and the positive charge at the cerium level discovered during the bonding charge analysis. The occupation of the copper s states increased significantly with respect to the previous case where the copper adatom charged positively, which supports the negative charging of the copper atom adsorbed on the reduced ceria surface.

The charge population of the cerium atoms is presented in the first three lines of the table, where the charge population of the two formerly reduced cerium atoms and of one cerium atom from the deeper layer of ceria slab are displayed for comparison. The reduction apparent from the localisation of charge on one spin of the cerium f states was discovered on the exact cerium atom that was shown to form a bond with the copper atom. Since the reduction was discovered on just one of the two cerium atoms that had been previously reduced by the oxygen removal we assume, that the charge transported towards the copper atom originated mostly from the other cerium atom causing its reoxidation to Ce^{4+}. The occupation of the reoxidized cerium atom is presented in Table 4.5 as Ce

Table 4.5: **Charge population analysis of the system with the copper atom in the oxygen vacancy.** We display the charge population analysis for the atoms involved in the bonding of the copper atom in the vacancy as well as some of the other for comparison.

	Total	s	p	d	f
Ce reduced	10.9254	2.2732	5.9447	1.6028	1.1047 (1.0358-0.0689)
Ce unreduced	10.9724	2.2852	5.9363	1.9933	0.7577 (0.3934-0.3643)
Ce unbonded	10.8173	2.2722	5.9537	1.8636	0.7277 (0.3639-0.3638)
O 1st layer	6.5187	1.7030	4.8156	–	–
O 3rd layer	6.5454	1.7334	4.8119	–	–
O bulk	6.5272	1.7066	4.8206	–	–
Cu	11.3216	1.2551	0.2666	9.7999	–

unreduced. In comparison with the third Ce atom from the slab, the reoxidized Ce shows higher occupation especially at the d states.

Slightly more occupation was discovered in the s states of the oxygen atoms closest to the copper atom located in the third atomic layer compared to the rest of the oxygen atoms.

The DOS analysis of the atoms in the system is displayed in Fig. 4.10. As in the previous cases several effects can be observed on a curve of a total density of states of the system. The effect labeled "1" is a result of the sharp f peak of the up spin of the cerium atom which was confirmed to be reduced and to form a bond with the copper atom. The sharp peak of the copper d states is responsible for creating of the feature labelled "2". The sharp high peaks of copper and cerium suggest forming of a strong ionic bond. Slight covalent contributions to the bond are realized by the overlap of the copper s states, the lower peak of the Ce f orbitals and the concerned oxygen py orbital, but overall this bonding is mostly ionic.

The magnetisation of the system was calculated 1.24 μ_B resulting from the localized electron on the one reduced cerium atom, whereas from the self consistent calculation of the reduced ceria surface without the copper atom the two times higher magnetisation 2.63 μ_B was obtained. This confirms the finding that the oxidation of one of the two cerium atoms reduced upon creating the oxygen vacancy occurred during copper adsorption.

4.5 Discussion and summary

In this Chapter we studied the effects of copper adsorption on the reduced and stoichiometric ceria surface. Like it was reported in the cases of platinum, palladium and gold, also in the case of Cu the most stable adsorption site on the stoichiometric ceria surface is the bridge between two surface oxygen atoms. Similar effects were observed in the case of copper adatom as were reported for the case of gold adatom.

Apart from the bridge system, the bonding at the top system was more straightforward in form of more clear overlaps of well defined peaks, but overall

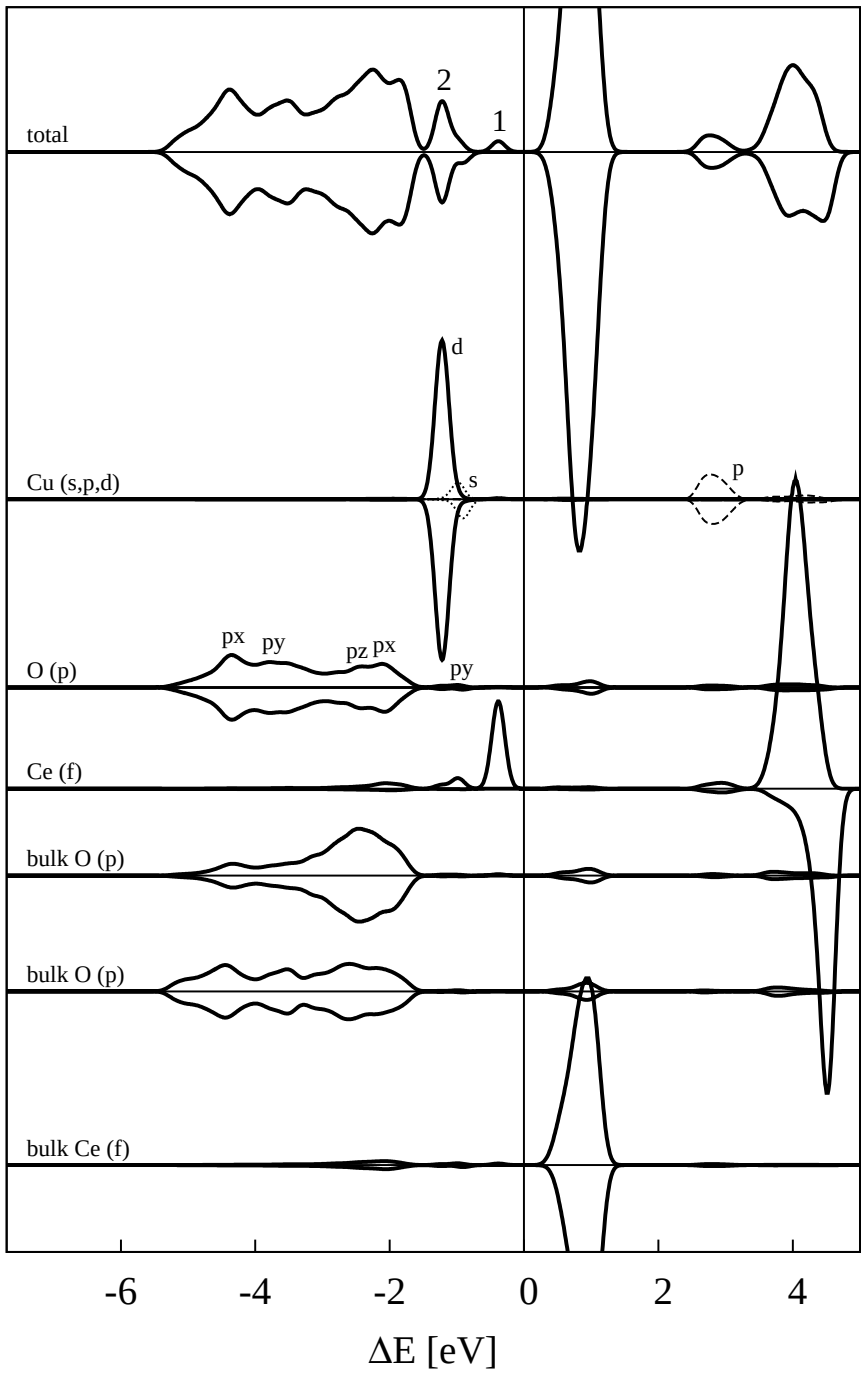

Figure 4.10: **The density of states of the system with the copper atom in the oxygen vacancy.** The density of states was projected on different atoms in the system. The total DOS is displayed at the top of the figure. Following curves represent orbitals of copper atom, oxygen atom from the third atomic layer which is involved in the bond, cerium atom from the underlying layer bonding with the copper atom, oxygen atoms from the surface layer and the fourth atomic layer and cerium atom from the fifth layer, describing from the upper curve to the bottom.

the bonding properties showed similar tendencies in both systems. The presence of the copper atom at the stoichiometric ceria surface caused the reduction of one cerium atom which was proved by the localisation of the charge in one spin of the Ce 4f states below the Fermi level apparent from DOS and charge population analysis. The oxidation of the copper adatom was observed slightly stronger in the top adsorption site than in the bridge adsorption site. The ionic contribution to the bonding was shown mostly from the transfer of the charge from the copper adatom to ceria slab at the integrated bonding charge curve, while the covalent contributions are apparent from the overlap of the copper d and oxygen p states at the DOS curves.

The adsorption at the oxygen vacancy on the reduced ceria surface showed different bonding properties than the adsorption on the stoichiometric ceria surface. As well as in the reported case of gold, the creation of the oxygen vacancy caused the reduction of two cerium atoms one of which was consequently reoxidized during copper adsorption. The copper adatom charged negatively opposite to the positive charging in case of adsorption on the unreduced surface due to the charge transfer from the reoxidizing cerium atom. The bonding of the adatom showed more ionic character on the reduced surface than on the stoichiometric.

The oxygen storage capacity of ceria, which is based on the reduction and oxidation of the cerium atoms, is supported by the ability of the copper adatom to induce the reduction of a cerium atom upon adsorption at ceria surface. Since the behaviour of the copper adatom showed similar effects as were reported for Pt, Pd and especially gold adatoms, we can expect, that as well the copper adatom increases the activity of the system and thus its catalytic ability.

Chapter 5

Interface Cu (111) / CeO_2 (111)

Several macroscopic properties of the materials often change in the presence of the microscopic interface, which is significant in the technological applications. Interfacial phenomena are relevant in many fields of applications, including electronics, electrochemical fuel cells, gas sensors, and thermal protective coatings [61]. In chemical applications the metal-oxide interfaces are often used as heterogeneous catalysts, whose theoretical understanding is the main subject of this thesis.

In the previous Chapter we studied the smallest possible Cu/CeO_2 interface of a copper cluster on ceria surface, the interface between the $CeO_2(111)$ surface and one Copper adatom. In this Chapter we consider the other extreme possibility, the $Cu(111)/CeO_2(111)$ interface inside of the large copper particle supported on ceria surface. In addition we study the properties of the interface of a thin copper film supported by ceria.

The most stable and commonly experimentally observed surfaces of both components, copper and ceria, are the (111) surfaces. Therefore we consider as a representative model structure the interface formed by the Cu(111) and $CeO_2(111)$ surfaces. Those surfaces have lattice parameters in convenient ratio 3:2 allowing formation of the coherent interface, which is confirmed by several experiments as for example reported in Ref. [7]. For this interface we will determine the exact local structure and the electronic rearrangement leading to bond formation. In addition, the calculations will allow us to estimate the decay of the interface effects into the bulk of the oxide material. We will also explore the interface bonding of an ultrathin copper film supported by ceria surface and compare it to the interface bonding discovered in the bulk-like case. For this purpose we set up several computational systems differing in the number of atomic layers and in the presence or absence of vacuum layer on top of the copper slab.

The studies of such interfaces are complicated especially when determining the most stable configuration of the interface, which include finding of the relative position of the Cu and CeO_2 crystals with respect to each other. Thus in order to speed up the calculation, we have explored the 3D energy landscape controlling this issue with increasing level of accuracy. First we performed a set of self-consistent calculations at the DFT level that allowed us to estimate the mutual position of the surfaces corresponding to the minimal energy in the plane

parallel to the interface and in the direction across the interface. These results were refined (and confirmed) afterwards by more precise calculations at the spin-polarized DFT+U level. The resulting minimum energy configuration was then fully relaxed. The comparison between the DFT and DFT+U shows a remarkable and unexpected *qualitative* difference in the metal-oxide bonding type predicted by the two levels of theory, showing once again the necessity for going "beyond-DFT" in the study of ceria-based systems.

In all the systems considered the calculations predict the electron transfer from the metal to the oxide surface leading to the formation of a monolayer of reduced ceria at the interface.

5.1 Previous Studies

Several experiments were conducted concerning systems where copper and ceria come in contact creating a copper (111) – ceria (111) interface. In particular in Ref. [7] the valence band states of copper loaded ceria powder consisting of submicrometer ceria particles covered with thin copper film were studied by the means of XPS and SRPES in order to determine its catalytic properties. The inverse model system consisting of two monolayers of ceria grown on copper crystal with (111) plane on top was used to study the interactions at the interface. It was shown, that in the presence of copper, ceria powder is partially reduced [17]. In Ref. [18] partial reduction of CeO_2 (111) surface was shown as well.

Theoretical studies were performed on different metal-ceramic interfaces. In Ref. [60] the systems composed of Pd and Pt on ZrO_2 and CeO_2 were explored by the standard DFT method. The influence of the electronic structure of the support material on the geometry of the interface was reported. The different chemical properties were discovered in the systems with different type of support. In the systems with ceria support the conduction band contained a contribution of the f states of the metal, while in the systems with the ZrO_2 support the band include the features which originated from the metal sp states. The CeO_2 interfaces were reported to show metallic behaviour while the ZrO_2 interfaces included a small band gap of 0.1 eV. The metal on the ZrO_2 surface was shown to straighten the Zr-O bonds, while the Ce-O bonds in the case of ceria support have weakened and the Ce-O distances have lengthened.

In Ref. [61] the interface of (0001) α-Al_2O_3 surface and (111) Ni surface was explored. The interaction between the surfaces was discovered weak in low temperature vacuum conditions in agreement with reported experiments [90]. The bonding was shown to be realized mostly by the Ni-Al interaction for α-Al_2O_3 thicker than one layer. The charge is reported to localize at the interface region, only a very small charge transfer occurred across the interface, which is in contrary with calculations reported in Ref. [62, 63].

In Ref. [64] the interfaces Ag/MgO and Nb/Al_2O_3 were studied by the means of DFT the former using the LMTO method while the latter the pseudopotential method. The bonding at the Ag/MgO interface is described in terms of the electrostatic attraction between the ions in the MgO and the polarisation that is induced in the metal, no charge transfer is reported opposite to the case of

Ti/MgO interface where the transfer of electrons from the Mg-O bonds to the Ti-O bonds was discovered. Larger overlap of full Ag d band with MgO valence band is shown compared to the lower overlap for the partially occupied Ti d band. The metallic gap states are reported at the interface. The bonding at the Nb/Al_2O_3 interface include the charge transfer from the metal to the oxide causing positive charging of the Nb atoms and creation of the negative O ions.

The Ag/Al_2O_3 interface is considered in Ref. [65], where the Al and O terminated surfaces of alumina are explored. Different bonding properties are discovered depending on the alumina surface. In the case of Al terminated alumina surface, negligible charge transfer is observed, which suggests physisorption as the interfacial bonding. The other case of O terminated surface, the charge transfer occurred towards the alumina causing chemical Ag-O bonding.

Many articles are devoted to the Cu/α-Al_2O_3 interface. Some explore the Al terminated alumina surface [66, 67, 68, 69, 70], some consider the oxygen terminated alumina surface [71, 70, 66]. In Ref. [69] the adhesive energies and the interfacial electronic structure of the Al terminated $Cu(111)/Al_2O_3(0001)$ interface were computed. The electronic structure analysis revealed the ionic component in the Al_2O_3 bonding, while it also showed covalent component not only to the Cu-O interfacial bonds but to the Al_2O_3 bonds as well. No bonding was discovered between the Cu-Al atoms, suggesting the bonding only via the covalent/metallic Cu-O bond. Positive charging of the copper atoms is reported.

On the contrary S. Tanaka et al in Ref. [66, 67] examine both the Al and O terminated α-Al_2O_3/Cu interfaces. Strong covalent and ionic interactions are reported for the oxygen terminated system, moreover in Ref. [71] Cu 3d – O 2p hybridization and electron transfer from Cu to the oxygen layer are discovered. Different results are presented for the case of the Al terminated system where the weak covalent and electrostatic image interaction is shown and Cu-Al hybridisation occurs. In Ref. [68] the charge transfer from Al_2O_3 to the copper is reported.

5.2 Calculation Details

As mentioned at the beginning of the Chapter, we investigated different systems composed of different number of layers of the components and with or without the vacuum layer on top of the copper slab. The systems were set up with a (3×3) copper slab four layers thick placed on top of the (2×2) ceria slab two and three layers thick. The lattice parameter used for the calculations was obtained from the results of the bulk systems in Chapter **2**. The calculations were performed with periodic boundary conditions for the supercells, the basic system is displayed in Fig. 5.1.

For the scf calculations we used a (4×4×2) set of k-points. The k-points were generated automatically as Monkhorst-Pack grid[78]. Energy cutoffs of E^{cut}_{rho} 300 Ry and E^{cut}_{wfc} 30 Ry were chosen.

Different levels of theory were used for the calculations. The initial search for the most stable relative position of the slabs via determining the 3D energy landscape was performed by means of the standard DFT approach. The results

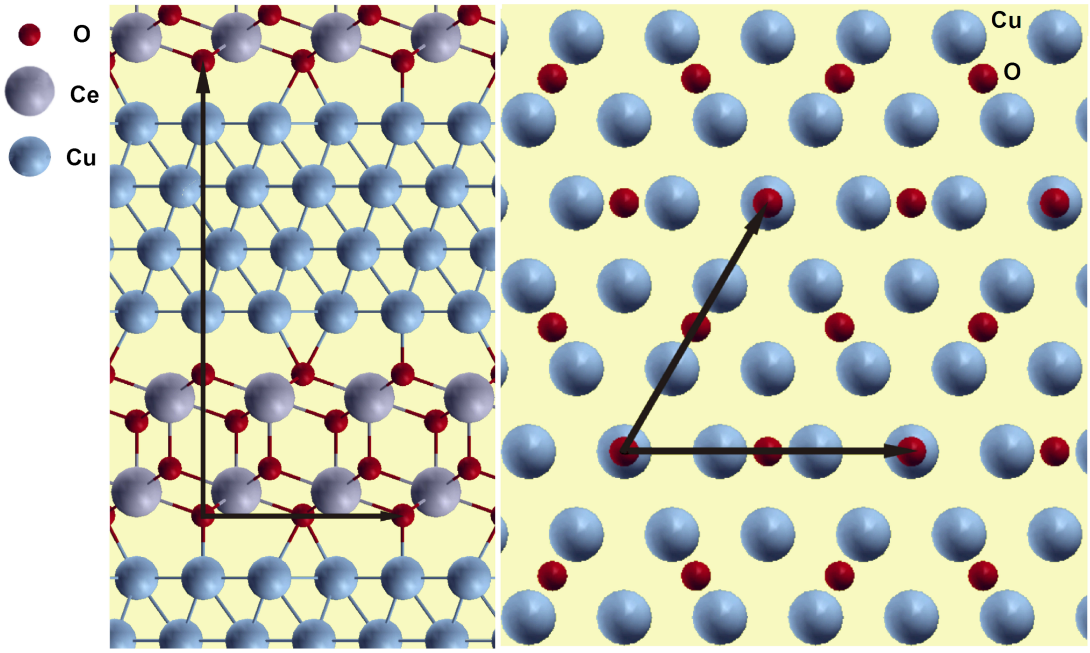

Figure 5.1: Supercell used in calculations, projection to x-z plane (left) and x-y plane (right). The interface is represented by 4-atom-layers thick slab of copper (111) planes and 2-molecule-layer of CeO_2 (111) planes in z direction and (2×2) ceria molecules placed on (3×3) copper atoms in x-y plane.

were then refined by including spin-polarization and the Hubbard U term in the energy functional. This study allowed to determine the local atomistic structure of the Cu/CeO2 interface and was performed with a supercell consisting of four Cu layers and two CeO2 tri-layers. This choice of thickness of the layers corresponds to the layer sequence periodically -Cu-Cu-Cu-Cu-O-Ce-O-O-Ce-O- (Fig 5.1) and allow to have the two interfaces arising from the periodic boundary conditions as similar as possible while keeping reasonable time and hardware requirements for the calculations.

Next, the interface structure with the lowest energy determined with the previous study (both at the DFT and DFT+U spin-polarized levels) was fully relaxed according to the calculated atomic forces. All atoms were allowed to relax except the two inner layers of copper atoms and the two inner layers of oxygen atoms that were fixed to their initial coordinates. The relaxation was stopped when the force acting on each relaxing atom was less than 0.035 eV/Å.

The analysis of the electronic structure and of the interface bonding were performed by a set of scf calculations with (4×4×2) k-point mesh consisting of 16 k-points and non scf calculation with a k-point mesh increased to (8×8×4) consisting of 20 k-points for all the set up systems in both DFT and DFT+U calculations.

The effect of the interface on the material extending towards the bulk was determined by increasing the thickness of the supercell to four layers of copper atoms and three trilayers of ceria molecules creating atomic sequence -Cu-Cu-Cu-Cu-O-Ce-O-O-Ce-O-O-Ce-O-. This calculation allowed for checking the convergence

of the predictions as a function of the number of layers and for establishing the decay of the interface electron states into the bulk material.

Another set of calculations was performed in order to investigate the properties of a thin Cu film on the Ceria surface. To this end a 14.12 Å thick layer of vacuum was added on top of the Cu slab in the supercell studied precedently and described above. These calculations were performed with the same computational parameters used in the other calculations as described before.

5.3 Local atomistic structure of the interface

5.3.1 Energy landscape of rigid-block Cu and CeO_2 slab translations

First we searched for the minimum energy position of ceria slab with respect to the copper slab. The calculations were performed in hierarchical order with increasing level of precision. First we fixed the distance at the interface to the value of 3.0 Å and performed several self-consistent calculations at the DFT level obtaining the 2D total energy landscape as a function of the rigid displacement of one slab with respect to the other in the plane of the interface. We used a grid of values for the displacement separated by approximately 0.05 Å mesh in x and y direction.

The resulting energy landscape allowed to identify a global energy minimum, whose configuration was used to determine the energy as a function of the distance between CeO_2 and Cu surfaces Δz. The results of these single-point self-consistent DFT calculations of the systems with variable Δz are displayed in Fig. 5.3.1. The configuration with the lowest energy consists of ceria and copper slabs separated by a distance of 2.1166 Å.

Then Δz was fixed at the correct value and the total energy as a function of displacement of one slab with respect to the other was explored again, with a result of providing the exact local atomistic structure at the interface. The symmetry of the system at the interface allowed us to reduce the area needed to explore. It can be demonstrated that the smallest area sufficient to represent the whole interface is a right triangle with a hypotenuse equal to 1/6 and one of the catheti equal to 1/12 supercell lattice parameter or equally a rhombus with a side equal to 1/12 supercell lattice parameter. The periodicity was verified numerically by considering several greater shifts in the whole supercell.

The left panel in Fig. 5.3 displays the energy map in two previously mentioned right triangles properly aligned to respect periodicity. The energy map is represented as energy differences from the configuration with lowest DFT total energy from spin unpolarised scf calculations which corresponds to dark blue color in the energy map. Therefore the most favourable position of (111) CeO_2 surface on (111) Cu surface was calculated to be the position, where one of the atoms in the bottom layer of copper is placed on top of one of the oxygen atoms in the top layer of ceria (Fig 5.3). The remaining three surface oxygen atoms are in the bridge position with respect to the copper atoms. This in fact is the most symmetrical alignment in the energy map.

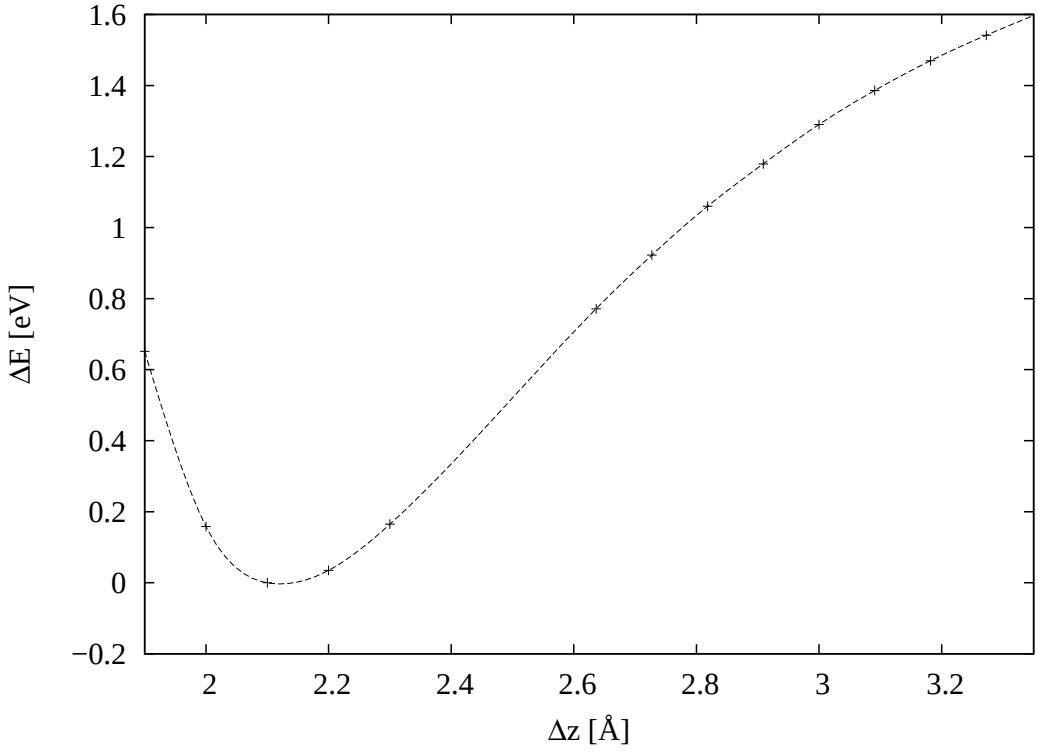

Figure 5.2: **Analysis of the distance between surfaces at the Cu(111)/CeO_2(111) interface.** Energy difference was displayed as a function of z distance. Zero energy corresponds to the minimal energy corresponding to Δz equal to 2.1166 Å.

The interface configurations corresponding to the minimum (the dark blue color in the energy map in the Fig. 5.3) and maximum DFT total energy (represented by the yellow color) were then recalculated at the spin-polarized DFT+U level. The calculated DFT and DFT+U total energies as well as their relative difference are compared in Table 5.1. The first column shows the result of the DFT calculations whereas the second column corresponds to the DFT+U level of theory. The DFT+U level of theory provided the same qualitative topology of the energy landscape, but with much higher corrugation, since the corrugation in the DFT case was in the order of the mRy, while it increased greatly in the DFT+U calculations. The difference was caused by the fact, that the two levels of theory predict a completely different electronic solution, one (the DFT) having a spin magnetization of $0\mu_B$ the other (DFT+U) being spin polarized with a magnetic moment of 8.32 μ_B, which correspond to 1.04 μ_B per Ce atom. Although the remarkable and unexpected difference in the interface bonding were caused by the different nature of the DFT and DFT+U self-consistent electron densities, the level of theory used has limited effect on the local structure as will be showed in following Section.

The interface obtained from the configuration calculations is displayed in Fig. 5.1 and 5.4. Two different types of environments appear in this interface configuration, both of them are showed in Fig. 5.4 and 5.5. The left subfigure of Fig. 5.5

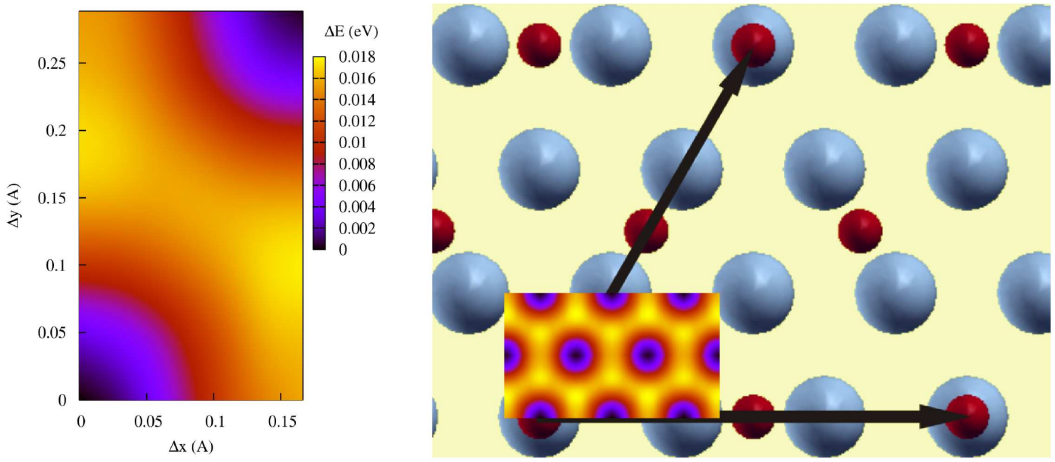

Figure 5.3: **Analysis of the configuration of the interface.** Energy map of possible shifts of ceria surface on copper surface is displayed as energy differences derived from configuration with minimal energy. The closer view to the energy map of the smallest periodically repeated area of the surface is shown on the left, while the position of the energy map on the surface is presented on the right. The dark blue color represents the interface configuration with the lowest energy. The system with one oxygen atom on top of the copper atom proved most favorable.

represents the environment that occurs once in one supercell as displayed in Fig. 5.4. It consists of a surface oxygen atom (O_T) on top of one copper (Cu_T) atom on the surface of the copper slab, therefore we call this environment the *top*. The three cerium atoms (Ce_T) in a layer underlying the surface oxygen layer which are concerned in the *top* environment create the three-fold hollow for both the oxygen and the copper atoms.

The environment in the right subfigure of Fig. 5.5 was called the *bridge*. It contains the surface oxygen atom (O_B) in the bridge position of the two surface copper atoms (Cu_{SB}). The other two surface copper atoms in the vicinity of the *bridge* environment (Cu_{LB1}, Cu_{LB2}) create the longer bridge perpendicular to the shorter bridge. One of the three concerned cerium atoms (Ce_{HT}) is placed right above one of the long-bridge copper atoms and all three of them create the three-fold hollow for the surface oxygen atom in the similar way as in the *top* environment. The Ce_H atoms in the *bridge* environment are equal to the Ce_T atoms in the *top* environment. Since the Cu_{LB1} and Ce_{HT} atoms are located at the same x-y coordinates, they have the shortest Cu-Ce distance at the interface, therefore the result of the mutual influence is the different relax behaviour from the other cerium and copper atoms. The *bridge* environment concerns the three remaining surface oxygen atoms thus appearing three times in the supercell. In the following calculations we investigate the relaxation and the bonding of the atoms in those two particular environments.

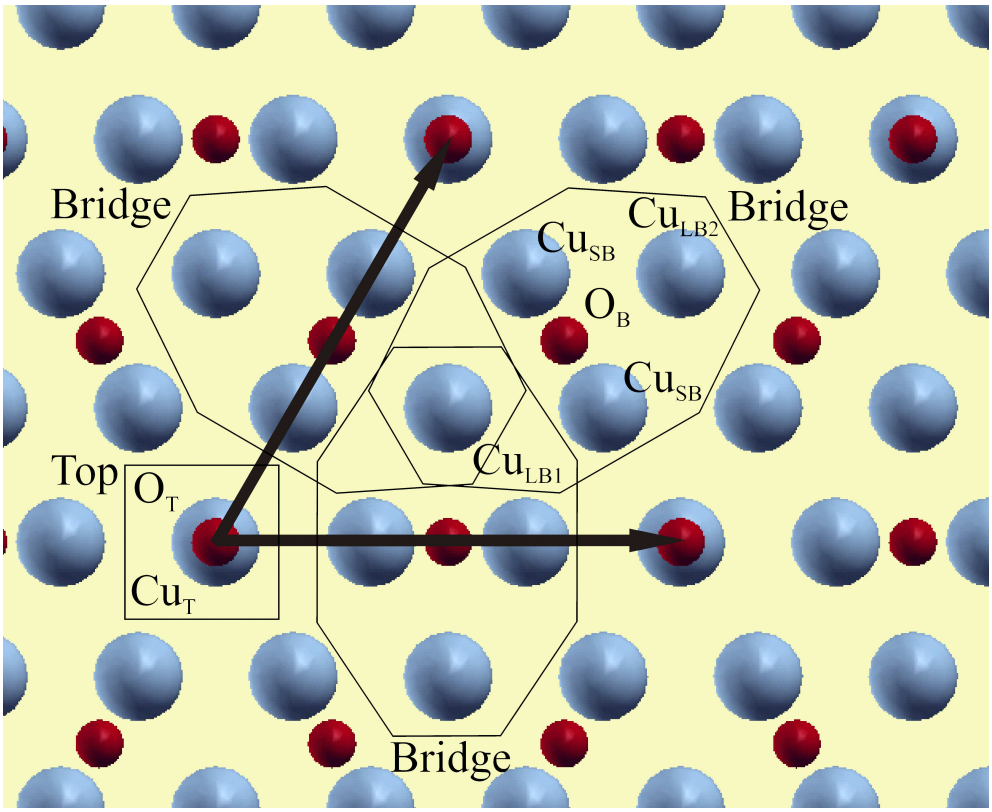

Figure 5.4: **The perpendicular view to the interface with the environments specified.** The small circles represent the oxygen atoms from the first ceria layer while the big circles show the positions of the copper atoms from the first copper layer. The arrows define the area of the supercell. The position of the characteristic environments is displayed together with the labels of the atoms.

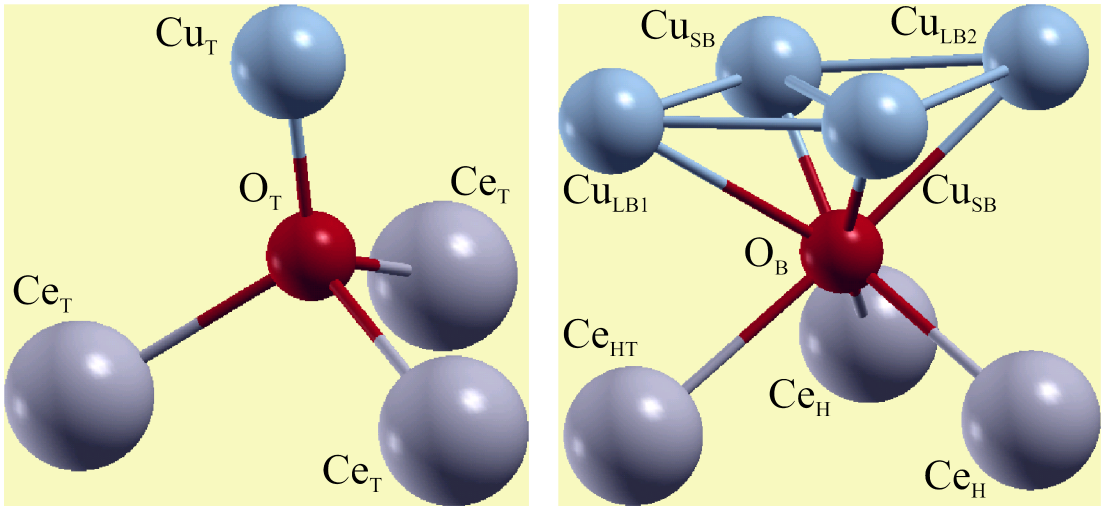

Figure 5.5: **The environments.** The closer view to the characteristic environments at the Cu(111)/CeO_2(111) interface is presented. The concerned atoms are labeled for the description of the relax and bonding behaviour. The atoms at the *top* environment are displayed left, while the right subfigure portrays the atoms belonging to the *bridge* environment.

Table 5.1: **Energies of the systems in DFT and DFT+U calculations.**

	DFT	DFT+U
E_{min} [Ry]	-6097.36771211	-6097.75122505
E_{max} [Ry]	-6097.36642213	-6097.73327452
ΔE [Ry]	0.00128998	0.01795053

Table 5.2: **The bond lengths of the significant interface bonds in different systems and calculations displayed in the units of Å.**

Top

		DFT	DFT+U			
	Original	2xCeO_2	2xCeO_2	2xCeO_2	Thin layer	3xCeO_2
Cu_T-O_T	2.12	2.00	1.89	1.89	1.89	1.90
O_T-Ce_T	2.39	2.40	2.48	2.49	2.49	2.48
Cu_T-Ce_T	3.68	3.62	3.72	3.73	3.73	3.72

Bridge

	Original	2xCeO_2	2xCeO_2	2xCeO_2	Thin layer	3xCeO_2
Cu_{SB}-O_B	2.48	2.37	2.03	2.03	2.04	2.04
Cu_{LB1}-O_B	3.09	3.13	2.89	2.89	2.88	2.89
Cu_{LB2}-O_B	3.09	3.08	2.70	2.69	2.77	2.75
O_B-Ce_H	2.39	2.47	2.66	2.65	2.65	2.65
O_B-Ce_{HT}	2.39	2.45	2.75	2.78	2.69	2.68
Cu_{SB}-Ce_H	3.19	3.26	3.29	3.30	3.29	3.28
Cu_{LB1}-Ce_{HT}	2.91	3.11	3.18	3.20	3.16	3.12
Cu_{LB2}-Ce_H	3.68	3.83	3.79	3.79	3.82	3.80

5.3.2 Fully relaxed local interface structure

DFT results

The relaxed local structures of the most stable interfaces determined above at the DFT and DFT+U level were examined in order to explore the effects appeared after the relaxation. The relaxed interface after the calculation performed with the DFT approach is displayed in the Fig. 5.6. The characteristic bond lengths for both previously described local environments before and after the relaxation are summarised in Table 5.2 for all the performed types of calculations. The bond lengths were explored on both the interfaces in the supercell to compare the symmetry of the interfaces. In the case of DFT calculations the interfaces proved locally identical in terms of the accuracy of calculated bond lengths, therefore only one set of distances is displayed in the table.

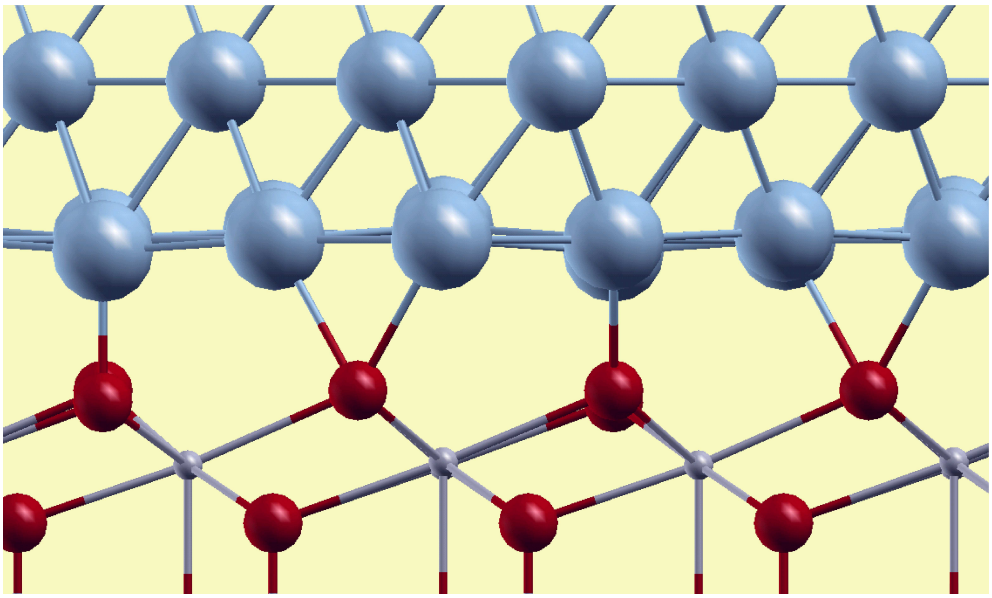

Figure 5.6: **The close view at the interface relaxed in DFT calculation.** The relaxation of the atoms in the *bridge* and the *top* environment is displayed.

At the *top* local environment site, the copper atom Cu_T moved during the relaxation towards the oxygen atom O_T decreasing the bond length for 0.12 Å. At the same time the three equivalent cerium atoms shifted away from the surface oxygen layer for 0.03 Å increasing the Ce-O_T bond lengths for 0.01 Å. The distance between copper atom Cu_T and the cerium atoms decreased for 0.07 Å.

Concerning the *bridge* environment site, the relaxation effects were different. During the relaxation the decrease of the short bridge bonds Cu_{SB}-O_B for 0.12 Å occurred as in the *top* environment, although in this case the shortening happened mainly through the shift of the oxygen atoms towards the copper slab. At the same time the copper atoms moved slightly towards the bulk copper, the Cu_{SB} atoms shifted for 0.04 Å, the Cu_{LB1} for 0.20 Åand Cu_{LB2} for 0.15 Å. Since the Ce_H atoms are equivalent to the Ce_T atoms from the *top* environment, their shift deeper to ceria slab together with the previously mentioned oxygen shift elongated the O-Ce bond for 0.07 Å. The Ce_{HT} atom having the same x-y co-

ordinates as the Cu_{LB1} shifted for 0.02 Å in the opposite direction towards the copper slab, thus lowering the increase of the concerned O-Ce bond for 0.06 Å. The distance between copper and ceria atoms increased.

DFT+U results

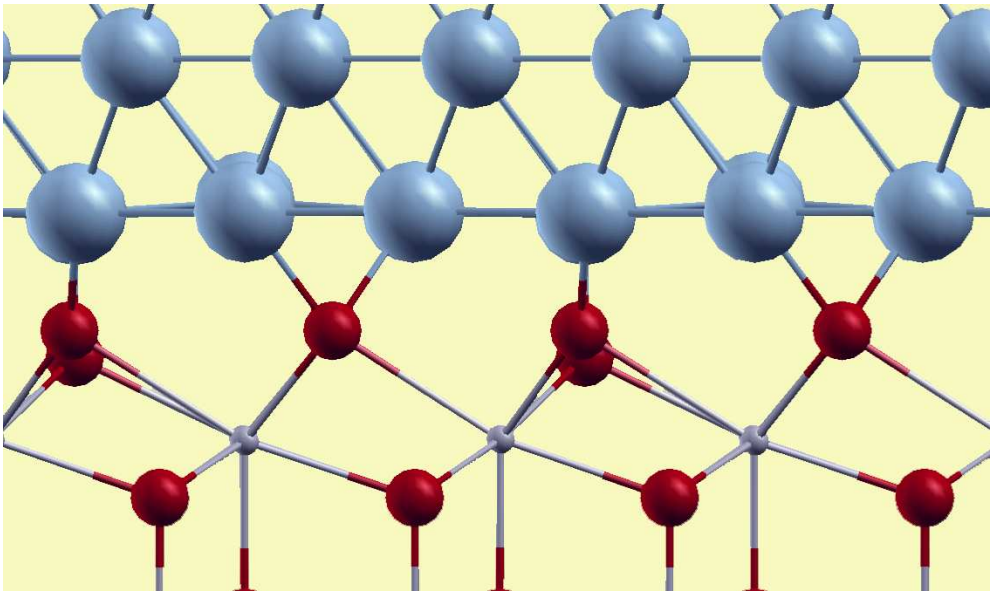

Figure 5.7: **The close view at the interface relaxed in DFT+U calculation.** The relaxation of the atoms in the *bridge* and the *top* environment is displayed.

The relaxation of the same system but with the spin polarisation of the system and the Hubbard U term included in the calculation resulted in quite different effect than the previous case to which we will compare the changes. The relaxed interface is displayed in Fig. 5.7 and the bond lengths at both interfaces present in the supercell are presented in Table 5.2.

In the *top* environment the Cu_T-O_T bond length decreased more significantly – for 0.23 Å. Unlike in the system calculated at the DFT level, the decrease has not been caused by the shift of the copper atom towards ceria slab, on the contrary the copper atom moved away from ceria slab into the copper slab for 0.05 Å. The decrease then was an effect of the movement of the oxygen atom for 0.28 Å towards the copper atom away from the cerium atoms. The cerium atoms moved for 0.02 Å into ceria slab which contributed to the increase of the Ce_T-O_T bond lengths for 0.08 Å. The distances between the Cu_T atom and Ce_T atoms grew for 0.08 Å.

Likewise, in the *bridge* environment the Cu_{SB}-O_B bonds decreased more significantly than in the spin unpolarised case – for 0.45 Å. The same effect was observed with the long-bridge bond length Cu_{LB1}-O_B, the other long-bridge bond Cu_{LB2}-O_B decreased which is in the contrary with the increase during the DFT relaxation. Although the copper atoms moved deeper into the copper slab away from the oxygen layer, the short bridge copper atoms Cu_{SB} for 0.08 Å, the long

bridge copper atoms Cu_{LB1} for 0.23 Å and Cu_{LB2} for 0.10 Å, which is mostly more than in the DFT case, the shift of the oxygen O_B atoms for 0.63 Å towards the copper slab was discovered responsible for the major decrease of the Cu-O bond lengths. The Ce_H-O_B bond length increased for 0.27 Å and the Ce_{HT}-O_B for 0.36 Å as a result of both the previously mentioned oxygen shift and the smaller shifts of the cerium atoms into ceria slabs, the Ce_{HT} atom for 0.04 Å and the Ce_H atoms for 0.02 Å). The change of the distances between the copper and cerium atoms showed a similar increasing trend as in the DFT case.

5.4 Metal-oxide bonding at the interface

5.4.1 DFT: spin unpolarized density and Cu-Ce covalent bonding

Fig. 5.8 displays the bonding charge analysis performed as described in the previous Chapter. The bonding charge was plotted at an isovalue of $|0.02|$ $e^-/Å^3$. In the figure, the blue color represents the depletion and the red color the accumulation in the charge density.

The forming of the Cu-Ce bond with covalent character is apparent from the changes in the charge density in the figure, since a directional pocket of charge accumulate along the Cu_{LB1}-Ce_{HT} bond and on the bond each of the Ce_H atoms form with the two nearest Cu_{SB} atoms. In addition, an ionic contribution appears between the Cu and O interfacial atoms (specifically Cu_T-O_T and Cu_{SB}-O_B), where the charge depletion occurs near the copper atoms being transferred to the closest O atom.

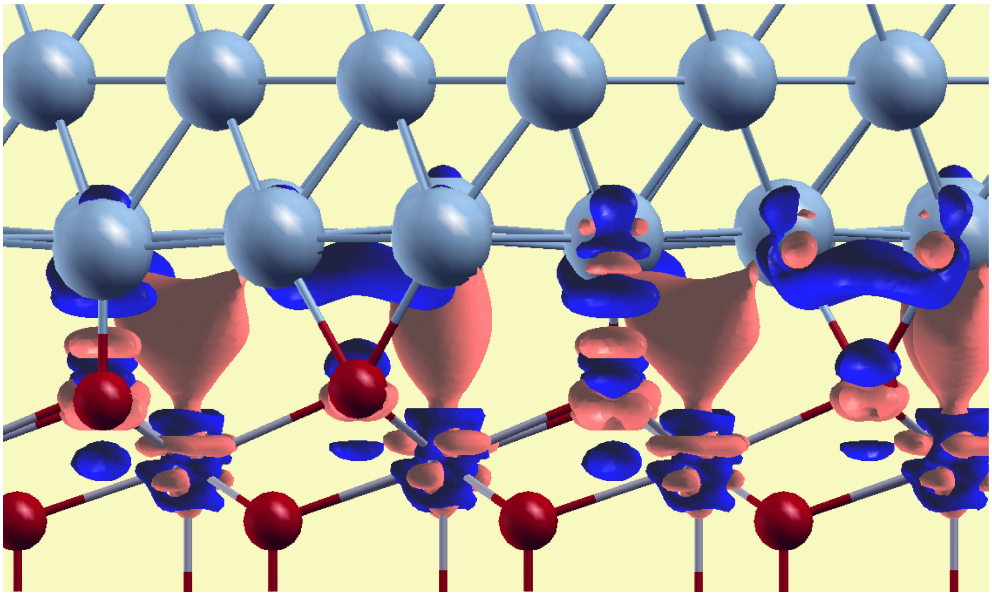

Figure 5.8: **The bonding charge at the interface from the calculation.** A side view at the system is presented with a charge density difference displayed at an isovalue of $|0.02|$ $e^-/Å^3$. The red color represents gain and the blue color loss in charge density.

Table 5.3: **Charge population analysis of the cerium atoms at the interface from DFT calculation.**

	Total	s	p	d	f
Ce_{HT}	10.8488	2.1938	5.9362	1.7352	0.9835
Ce_T	10.8994	2.1917	5.9354	1.7672	1.0050

The results of the charge population analysis are displayed in Table 5.3. The charge population of the cerium atoms show an increase of the occupation of the d an f states especially concerning the Ce_T atom. But differently from previous cases where the reduction of cerium atoms was observed, the occupation of the f states is not localized at one particular spin and at one particular f orbital thus the charge transferred at the interface does not fully occupy one Ce 4f state and no cerium reduction occurs.

The most important conclusion provided by the bonding charge and charge population analysis therefore is that the DFT calculations predict no reduction of the interface.

The density of states projected on different atoms in the supercell is displayed in Figure 5.9, the upper figure represents the atoms in the *top* environment, the bottom shows the DOS of the atoms in the *bridge* environment. In the *top* environment the Cu_T-O_T bond originates from the overlap of the copper dz2 orbital with the oxygen pz orbital and the other mostly sharp and high d orbitals (dx2-y2, dxy, dzx and dzy) with very broad and flat oxygen px and py orbitals. This suggests that the Cu-O bonding has ionic and covalent contributions. Cerium f orbitals have apart from the sharp high peak above the Fermi level in the unoccupied states also some states at the same energy as the copper d orbitals with which it overlaps creating a covalent bond. From the DOS it is apparent that no cerium reduction occurs since the Ce f states below the Fermi level have a very low occupation.

Similar effects can be observed in the *bridge* environment as well. The Cu_{SB}-O_B bond is determined by the overlaps of the copper dz2 orbital with the oxygen pz and px orbitals and the copper dzy and dzx orbitals with the oxygen py states. The broad Ce f states overlap with the copper d states forming a Cu_{SB}-Ce_H bond. The same effect can be observed also along the Cu_{LB1}-Ce_{HT} bond. The character of the bond is also covalent due to the broadness and flatness of the involved orbitals. As well as at the *top* environment no reduction of the cerium atoms was observed at the DFT level.

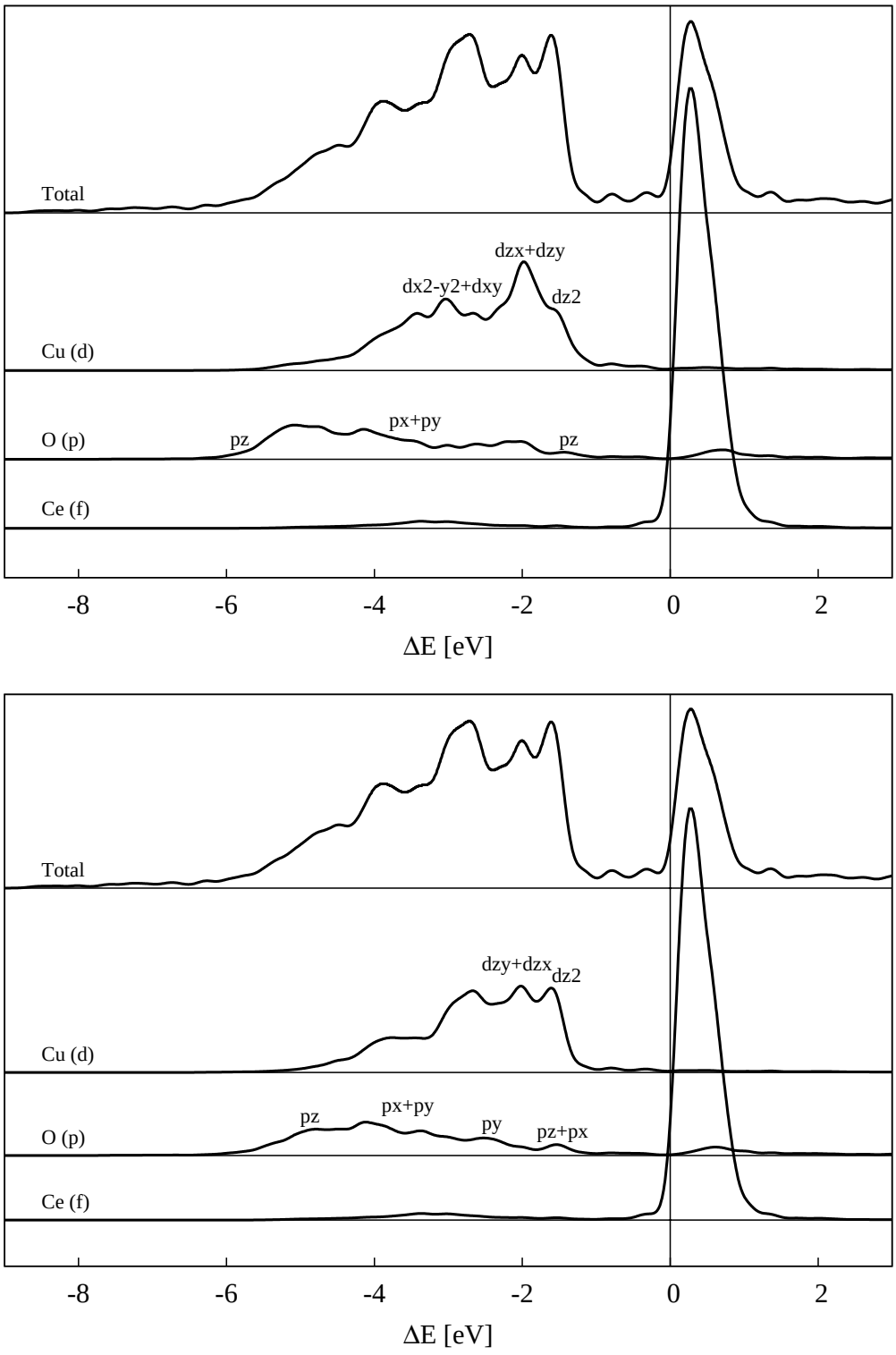

Figure 5.9: **The DOS analysis of the atoms at the interface calculated from DFT calculation.** The density of states of the atoms at the *top* environment is displayed in the upper subfigure (Cu_T, O_T and Ce_T) and the density of states of the atoms from the *bridge* environment is shown in the bottom subfigure (Cu_{SB}, O_B and Ce_H).

5.4.2 DFT+U: spin-polarized density, Cu-O covalent bonding and interface reduction

In the following Section we describe the bonding analysis corresponding to the most stable structure predicted by the DFT+U level of theory. We note once again that *this* is the most appropriate method for studying ceria-based compounds and hence its predictions are more accurate than those obtained at the previously described DFT level. We therefore emphasize that, among the different interfacial bonding predicted by the two approximations, the DFT+U one should be regarded as the more accurate and therefore closest to the experimental observations.

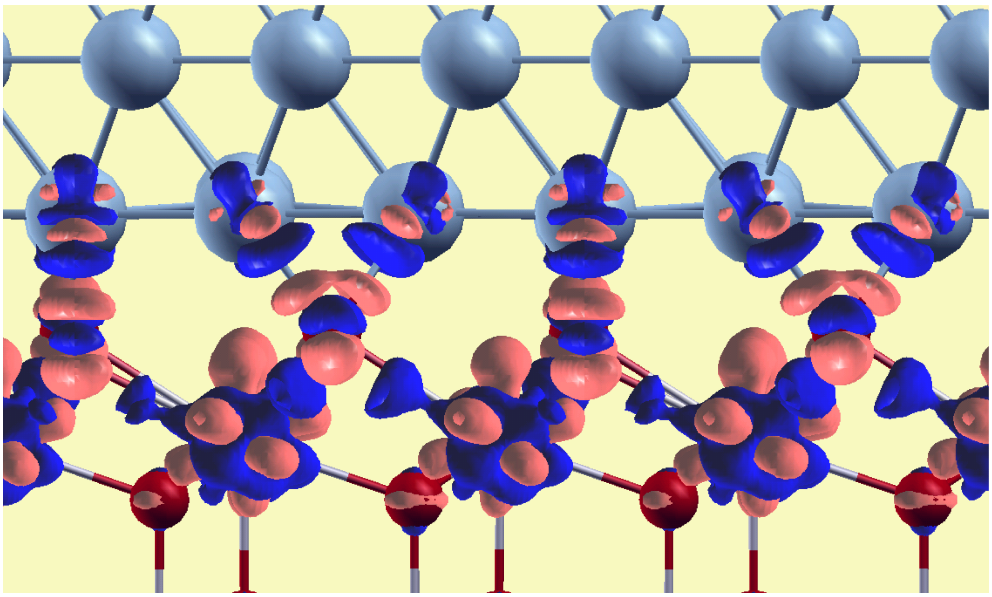

Figure 5.10: **The bonding charge at the interface from DFT+U calculation.** A side view at the system is presented with a charge density difference displayed at an isovalue of |0.04| $e^-/Å^3$. The red color represents gain and the blue color loss in charge density.

The bonding charge of the interface predicted by the DFT+U calculations is presented in Fig. 5.10. The charge difference is displayed for an isovalue of |0.04| $e^-/Å^3$. In this case in contrast with the DFT results no Ce-Cu covalent bond is discovered. The bonding charge is mostly localized along the Cu-O bonds and, to a lesser extent, also along the Ce-O bonds suggesting that the character of the interface bonding is realized mostly by Cu-O bonds. Most importantly a sizable charge changes are apparent at the interfacial Ce sites, that we suspect to lead to interface reduction, which will be shown in the following charge population analysis. The rearrangement of the charge is present on all four of the Ce atoms at the Cu/CeO_2 interface.

The charge population analysis of the cerium atoms at the interface is presented in Table 5.4. Instead of 10 e^- in the valence band of the metal cerium the cerium atoms in the supercell have nearly 11 e^-, where the excess charge localized mostly on one spin of the cerium f states while the other spin remained unoccu-

Table 5.4: **Charge population analysis of the cerium atoms at the interface from DFT+U calculation.**

	Total	s	p	d	f
Ce_{HT}	10.8707	2.1989	5.9281	1.6410	1.1027 (1.0354-0.0673)
Ce_T	10.9021	2.1945	5.9332	1.6716	1.1027 (1.0263-0.0764)

pied which is a sign of a reduction of Ce^{4+} atoms to Ce^{3+}. All the four Ce ions at the Cu/CeO2 interface exhibited the same charge population characteristics corresponding to the change of valency from 4+ to 3+. Due to the charge in the up spin of each cerium atom in the supercell, the magnetisation is consistently predicted to be 8.32 μ_B, which account to 1.04 μ_B per Ce atom.

The important finding is thus that all the cerium atoms are predicted to undergo the $Ce^{4+} \rightarrow Ce^{3+}$ transformation, hence the whole interface is reduced.

The DOS analysis was been performed and is presented in Fig. 5.11. The DOS of the same atoms as in the case of DFT calculation was analysed to compare the results. In the spin polarised case, for the bond at the interface only the Cu-O bonding is responsible. The Cu_T-O_T bond involves overlap of the copper dz2 orbital with the oxygen pz orbitals and the copper dzy and dzx orbitals with px and py orbitals. The overlap suggests that the type of the bond was covalent. Similarly the Cu_{SB}-O_B covalent bond is caused by the overlap of the copper d orbitals and the oxygen p orbitals particularly the dz2 and dzx orbitals with the px orbital and the dxy, dx2-y2 and dzy with py orbital. The cerium f orbitals are located below the Fermi level occupied in one spin which confirms the reduction. The high sharp cerium f peaks in both environments overlap with small oxygen pz orbital creating the covalent contribution to the Ce-O bond. Since the charge transfer occurred and from the character of the orbitals especially the sharper cerium f peak we suspect also the ionic contribution to the bonding.

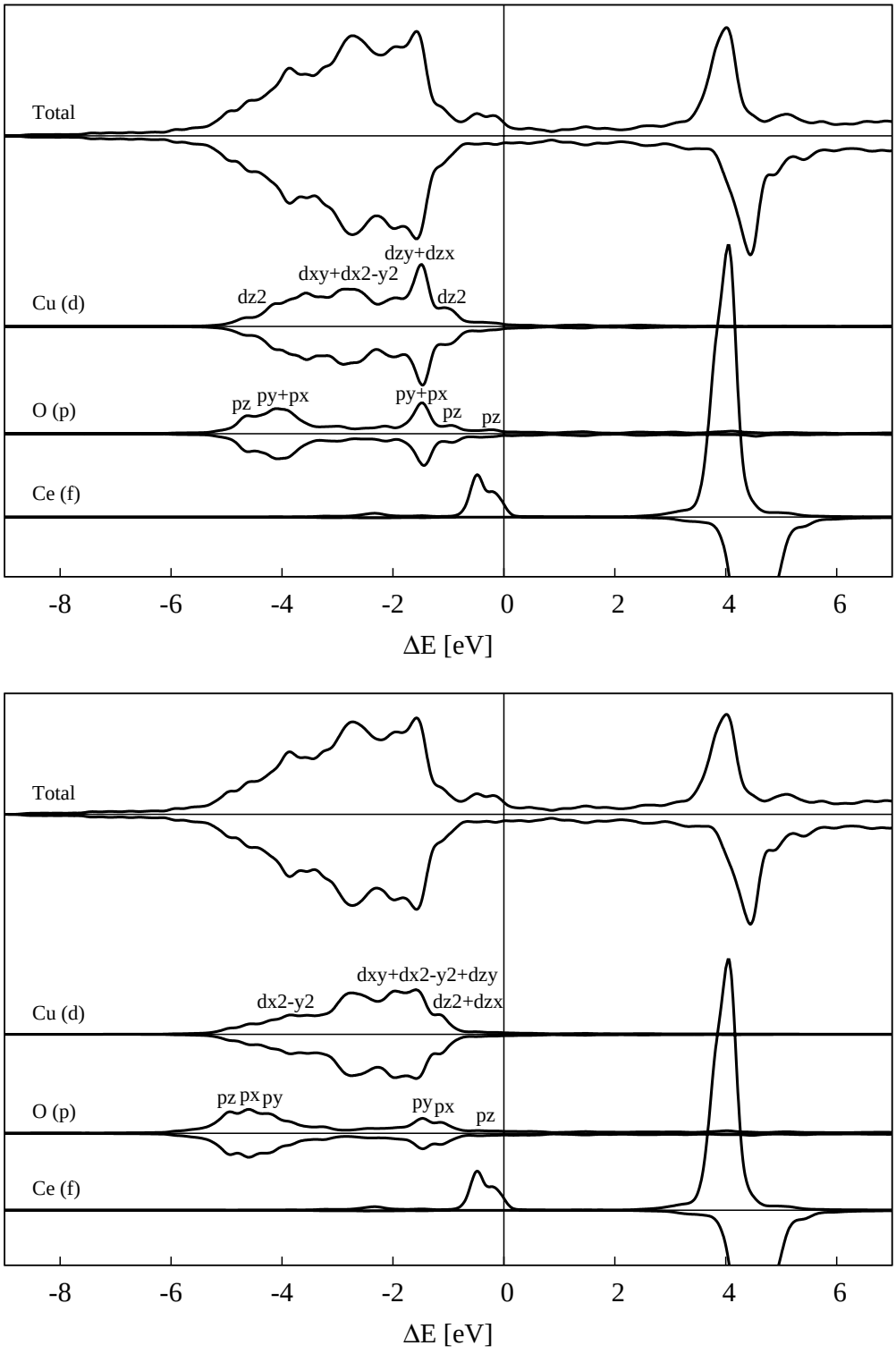

Figure 5.11: **The DOS analysis of the atoms at the interface calculated from DFT+U calculation.** The density of states of the atoms at the *top* environment is displayed in the upper subfigure (Cu_T, O_T and Ce_T) and the density of states of the atoms from the *bridge* environment is shown in the bottom subfigure (Cu_{SB}, O_B and Ce_H).

System with thicker ceria layer

The system with the thickness of ceria slab increased to three trilayers was examined at the DFT+U level. The relaxation was performed with the two interfacial ceria trilayers relaxing and the central bulklike ceria trilayer was fixed at the initial coordinates. The relaxation effects on the bond lengths (displayed in Table 5.2) were qualitatively and in most cases within 0.01 Å also quantitatively the same as in the DFT+U calculation of system with thinner ceria layer.

In this case we are interested in the behaviour of the oxygen atoms in the third subsurface atomic layer, since in this case they were allowed to relax. The observed effect of the relaxation of those oxygen atoms was their shift towards the interface for 0.04 Å. The corresponding Ce-O bond lengths thus as a result of previously mentioned shifts of cerium atoms into the slab remained the same or decreased for the maximum value of 0.02 Å.

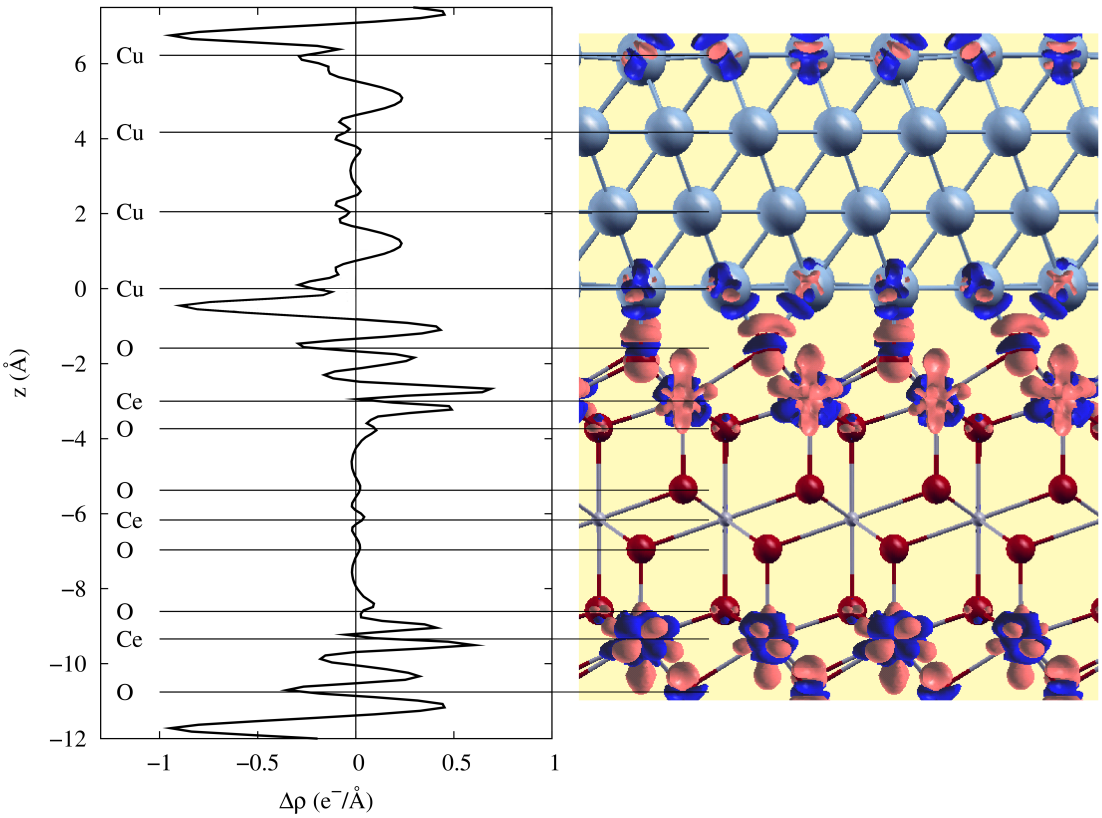

Figure 5.12: **The bonding charge at the interface from DFT+U calculation of the system with thicker ceria layer.** A side view at the system with a charge density difference in equipotential planes at the value $|0.04|$ $e^-/Å^3$ is displayed on the right. The red color represents gain and the blue color loss in charge density. On the left the charge density difference is integrated at the xy planes and plotted along the z direction.

Also the bonding character at the interface remained the same, which is apparent in the right panel of Fig. 5.12. From the left panel of the figure, displaying the bonding charge integrated in planes parallel to the interface, we can observe, that the charge redistribution at the level of the middle ceria layer occurs within

0.4 $e^-/Å$. It is confirmed by no apparent charge differences in the right panel of the figure. Also the DOS analysis, displayed in Fig. 5.13, provided results equal to those obtained with the thinner system.

The similarity of the relaxation and bonding properties of the thicker and thinner system suggest, that to achieve converged results for the Cu/CeO_2 system, two trilayers of ceria in the supercell suffice.

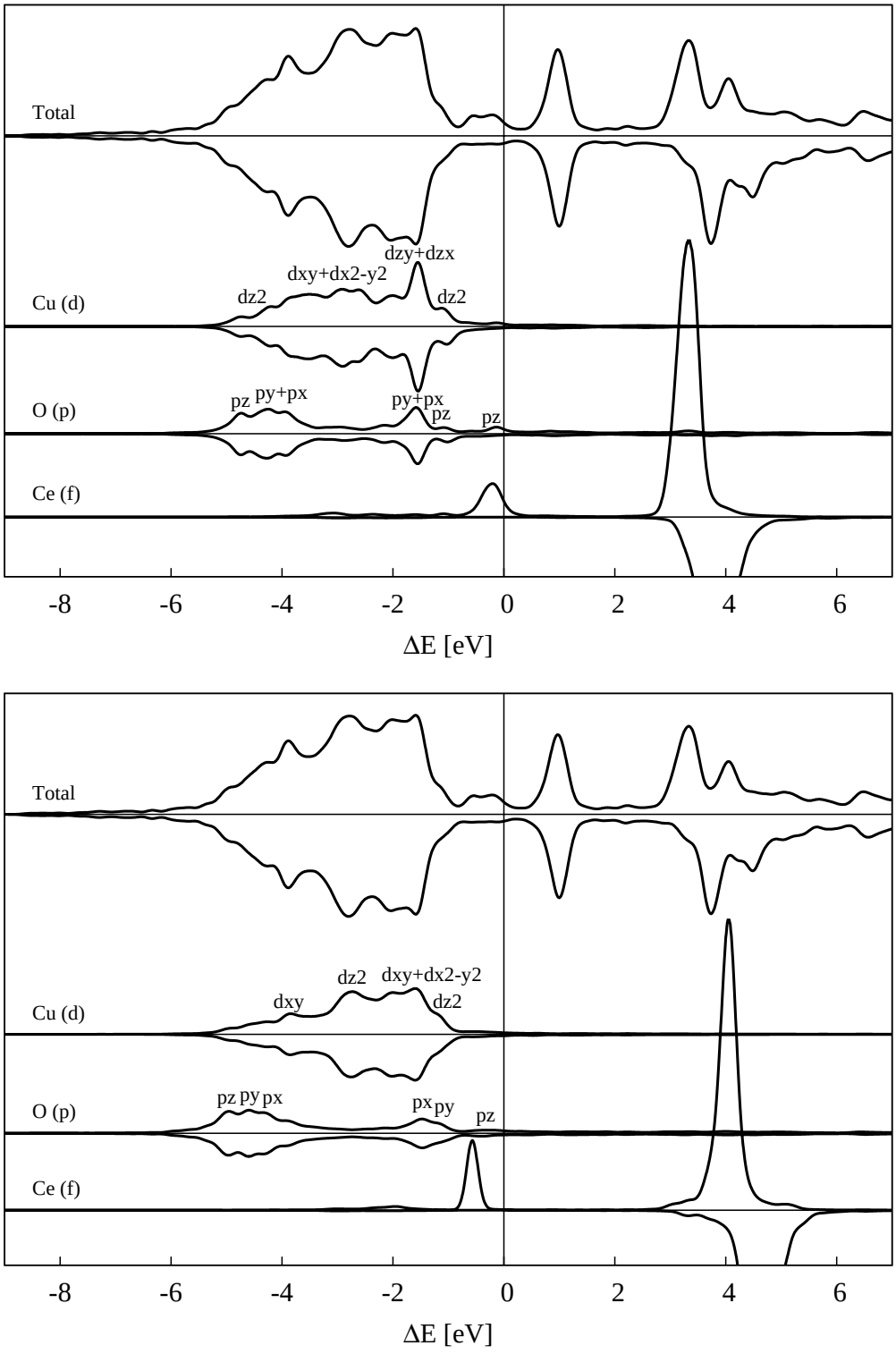

Figure 5.13: **The DOS analysis of the atoms at the interface calculated from DFT+U calculation of the system with thicker ceria layer.** The density of states of the atoms at the *top* environment is displayed in the upper subfigure (Cu_T, O_T and Ce_T) and the density of states of the atoms from the *bridge* environment is shown in the bottom subfigure (Cu_{SB}, O_B and Ce_H).

5.5 Cu thin films supported by ceria

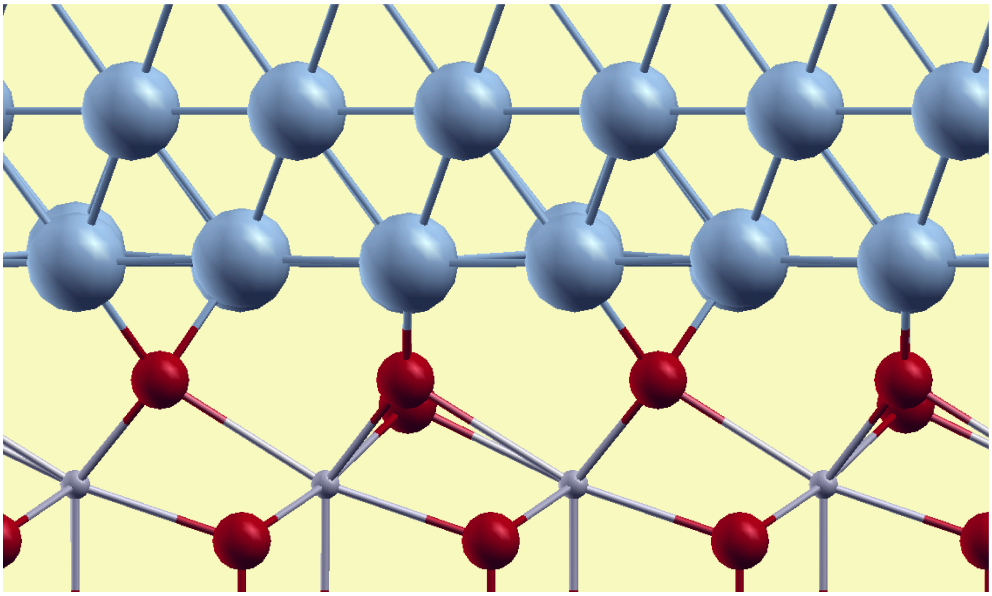

Figure 5.14: **The close view at the interface relaxed in DFT+U calculation of a system of thin copper film.** The relaxation of the atoms in the *bridge* and the *top* environment is displayed.

From the previous calculations we established, that the DFT+U level of theory provides the most reliable results for the analysed systems. This method was therefore used to study the interface between the four layer thick copper thin film and the support formed by ceria surface. We focus on finding out, whether the presence of a free copper surface in the distance of four atomic layers from the actual interface change the properties of the interface with respect to the properties determined in the previous calculations of the interfaces.

5.5.1 Local structure

The relaxed structure of the interface calculated at the DFT+U level is displayed in the Fig. 5.14. From the following description of the structural changes it is apparent, that the relaxed interface in the supercell with the vacuum layer exhibits very similar local geometry to the one without the vacuum layer. The shifts of the interface atoms showed similar relaxation patterns and tendencies, but with slightly smaller values than the previous case. The differences in the bond lengths turned out to be smaller than 0.01 eV.

In the *top* environment while the Cu_T atom shifted into the copper slab for 0.04 Å, the O_T atom moved in the same direction for 0.26 Å therefore the Cu_T-O_T bond length decreased for 0.22 Å, which is 0.01 Å less than at the interfaces in the system without the vacuum layer. As well in the *bridge* environment the decrease of the Cu_{SB}-O_B bonds for 0.44 Å was 0.01 Å smaller than in the previous system. Similar changes as in the system without the vacuum occurred also with the concerned atoms in the system with the vacuum – the O_B atoms shifted

away from the cerium layer for 0.59 Å while the Cu_{SB} atoms moved in the same direction for 0.07 Å. The rest of the copper atoms closed to the copper slab for 0.13 (Cu_{LB2}) and 0.22 (Cu_{LB1}) Å, where the former moved 0.03 Å more and the latter 0.01 Å less than in the previous case.

The Ce_T-O_T bond increased for 0.10 Å which is 0.02 Å longer than in the previous system. In the *bridge* environment the O_B-Ce_H bond increased for 0.26 Å, which is practically the same as in the system without vacuum, while the O_B-Ce_{HT} increased for 0.30 Å, 0.05 Å less. All of the cerium atoms moved into ceria slab for 0.03 Å contributing to the increase of the Cu-Ce bonds in a similar manner as in the system without the vacuum layer.

5.5.2 Interface bonding

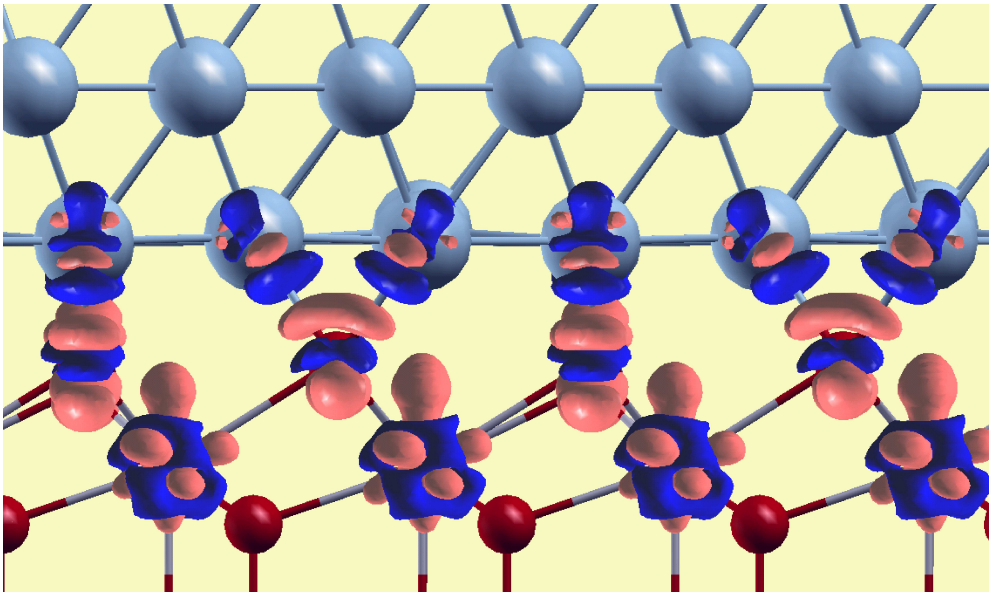

Figure 5.15: **The close view to the bonding charge at the interface from DFT+U calculation of a system of thin copper film.**

The bonding charge density is shown in Fig. 5.15 and 5.16 (right) plotted for the isovalue corresponding to $|0.04|$ $e^-/Å^3$. The comparison with the same bonding analysis calculated for the supercell without vacuum and displayed in Fig.5.10 show that also the bonding character is little affected by the presence of a free surface 4 layers away from the metal/oxide interface. The small effect of the free surface is also confirmed by the integrated curve on the left side of figure that was obtained by integrating the charge difference along x-y planes parallel to the interface. The important finding is that the bonding charge (the region in which the charge is perturbed by the presence of the interface) decayed very quickly, in within the first 4 Å, and no apparent changes occurred at any of the two present free surfaces in the supercell.

As in the previous case the bonds are visible along the Cu_T-O_T and Cu_{SB}-O_B bonds but unlike in the case of the first interface in the previous case there were no charge changes apparent along the Ce-O bonds. As in the previous case we

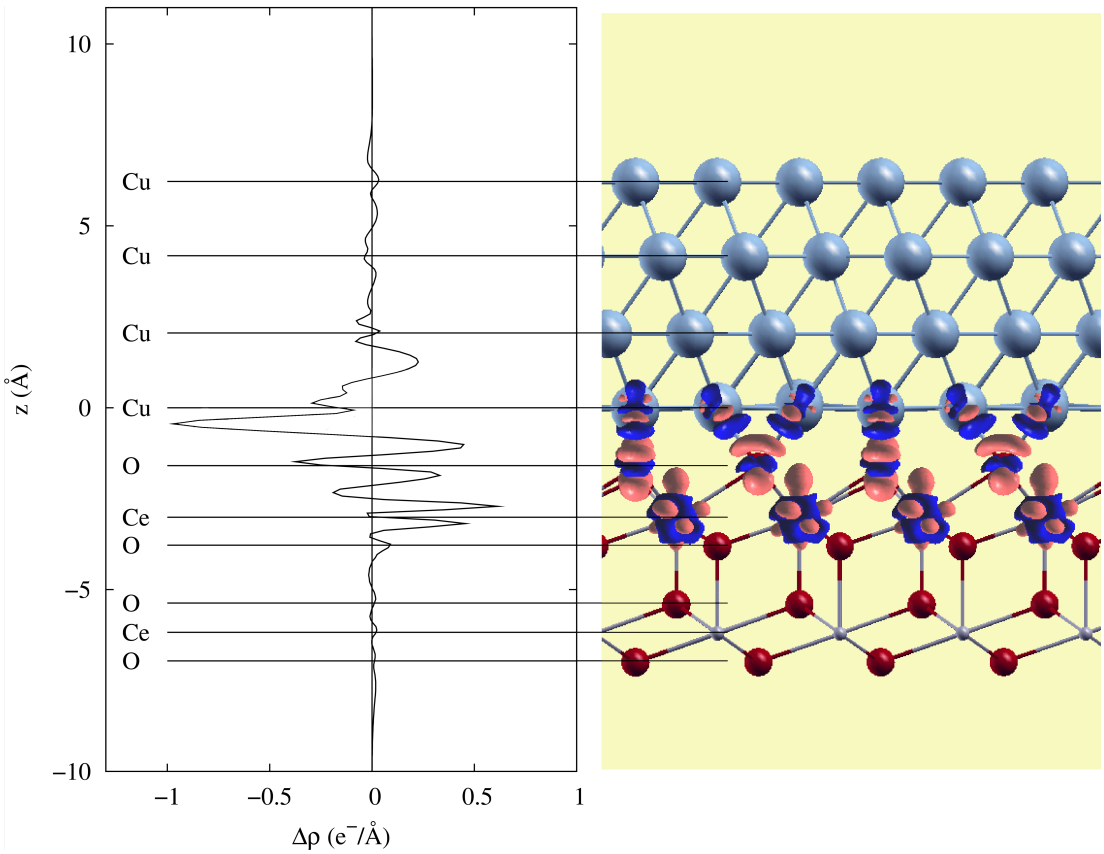

Figure 5.16: **The bonding charge at the interface from DFT+U calculation of a system of thin copper film with the vacuum layer.** A side view at the system with a charge density difference in equipotential planes at the value $|0.04|$ $e^-/Å^3$ is displayed on the right. The red color represents gain and the blue color loss in charge density. On the left the charge density difference is integrated at the xy planes and plotted along the z direction.

expect the cerium atoms to reduce due to the transferred charge and the copper atoms to charge positively. The effect of the reduction was observed only on the interface cerium atoms and not on the other four.

Since there is one layer of unreduced cerium atoms in the supercell, the charge population of reduced and unreduced cerium atoms can be compared. In Table 5.5 the charge population of the different types of interface cerium atoms is presented together with the unreduced cerium atom. Compared to the unreduced cerium atom the interface atoms are more occupied at the f states and little less at the d states. Moreover as in all the previous cases of reduced cerium atoms the charge in the f states is localized only in one spin, the other is very little populated. Those results confirm the reduction of the four interface cerium atoms. The localisation of the charge mostly in one spin of the f states contributes to the total magnetisation of the system equal to 4.72 μ_B, leading to 1.18 μ_B per Ce atom. The total magnetisation is by an overall factor of two smaller than in the case of the system with two interfaces which is in agreement with the theory that the presence of the copper surface cause the reduction of the nearest layer of the cerium atoms, while the next layer remains unreduced.

Table 5.5: **Charge population analysis of the cerium atoms at the interface from DFT+U calculation of a system of thin copper film.**

	Total	s	p	d	f
Ce_{HT}	10.8501	2.2006	5.9321	1.6646	1.0527 (0.9789-0.0738)
Ce_T	10.8649	2.1992	5.9354	1.7112	1.0191 (0.9324-0.0866)
Ce unreduced	10.8100	2.2707	5.9548	1.8537	0.7307 (0.3755-0.3552)

The DOS analysis of the atoms in the system with added vacuum layer proved nearly the same as the DOS of the atoms in the previous system. The Cu_T-O_T bond is again caused by the overlap of the copper dz2 orbital with the oxygen pz orbital and the overlap of the copper dzy and dzx orbitals with the oxygen py and px orbitals, while the Cu_{SB}-O_B originated from the overlap of the copper dz2 and dzx orbitals with the oxygen px orbital and the copper dxy, dx2-y2 and dzy orbitals with the oxygen py orbital. The form of those bonds is considered covalent. The ionic part of the bond derives from the sharper cerium f peak below the Fermi level which also covalently overlaps with oxygen pz orbital suggesting that although it is not apparent in bonding charge analysis figure, the bond occurs as in the system without the vacuum layer.

5.6 Discussion

The most important findings described in this Chapter are summarized in this Section.

Concerning the local geometry at the interface, the two levels of theory provide the same qualitative description of the local interface structure, except that in the spin polarised DFT+U case, some of the significant structural effects observed in the spin unpolarised case were amplified. The most relevant of the relaxation effects are the decrease of the Cu-O bonds, the increase of the Ce-O bonds, and the larger shift of the interface oxygen atoms away from the cerium layer towards the copper slab.

Prediction of correct electronic structure at the interface is instead much more delicate and sensitive on the precise theoretical treatment of the self-interaction correction, which the standard DFT functionals does not capture appropriately. Therefore very different qualitative descriptions were discovered at the DFT level (which tend to delocalize the excess charge in the interface region along the Cu-Ce bond) and at the DFT+U level (which tend to convey this excess charge transferred from the Cu atoms deeper into the oxide layers, localizing it on the first available Ce sites, thus driving their reduction).

In particular, at the DFT level, it was discovered, that the density is spin unpolarized, that the bonding at the interface has a covalent character along the Ce-Cu bonds and that no Ce atom undergoes reduction. The Ce 4f states were slightly occupied providing the interface a metallic character (the Fermi level crossed the sharp f-like band). This partial occupation is not correctly dealt with by the DFT-GGA functional and was the cause for introducing the DFT+U into the calculation.

In case of DFT+U calculations, the charge transfer between the slabs and the reduction of the cerium atoms was present in the spin polarised while absent in the spin unpolarised case, where just a charge redistribution at the interface region occurred. Moreover more ionic contribution was found to the bonding in the spin polarised case.

A further proof of the actual accuracy of the prediction of the spin-polarized DFT+U method is given by the total energy. The total energy of the spin polarised DFT+U calculation is lower (by 5 eV) than the total energy of the corresponding spin unpolarised DFT+U calculation, the latter providing the same description of the unpolarized DFT calculation.

The study of the system with the vacuum layer added in the place of one of the interfaces in the supercell provide a direct proof that the effect of reducing the cerium atoms is induced by the presence of copper close to the interface since the reduction occurred only on the side of ceria slab, where it was in contact with copper. This comparison also allow us to conclude that the charge transfer leading to the interface bonding is very short ranged, it involve only the first CeO_2 trilayer in the oxide side and the first 1-2 atomic layers on the Cu side. The bonding was found out the same as in the previous system, containing both covalent and ionic contributions.

The reduction of the cerium atoms in the presence of copper leads to an important implication for the real Cu particles deposited on ceria surface. The significant outcome is that the whole interface located below a Cu particle supported on CeO2 is predicted to be reduced.

In comparison with the theoretical calculations reported on other metal-oxide systems presented in the beginning of this Chapter, the Cu/CeO_2 system exhibits different bonding properties. In the related case of Pd (or Pt)/CeO_2 a presence of a metallic interface was concluded by a DFT calculation as reported in Ref. [60]. This conclusion is likely to be an artifact of the inappropriate level of theory used in that work, since the same effect is obtained in our calculations performed on the interface with the DFT level of theory. Although there are similarities in the local geometry such as the increase of the Ce-O bond lengths, it was determined before, that the geometry is less dependent on the level of theory used (DFT or DFT+U).

In the case of non-reducible support such as Cu/α-Al_2O_3, the interface bonding is reported to be realized by strong covalent and ionic interactions and the charge transfer from the metal layer is reported to localize on the oxygen layer, which is at difference to the bonding at the Cu/CeO_2 interface, where the charge transferred from copper localizes on and reduces the cerium ions. In this case the different predictions from our DFT+U calculation concerning the Cu/CeO_2 interface and the reported DFT calculation of the Cu/α-Al_2O_3 are physical. This is because the different methods were used each on the appropriate system and therefore the findings for the non-reducible oxide are solid.

The decrease of Cu-O distances at the interface during the relaxation to 1.9 Å which is close to the Cu-O bond length in copper oxide Cu_2O 1.84 Å[89] suggests the tendency to locally form a copper oxide at the interface. This finding supports the hypothesis proposed by Matolín et al [7]. In this work based on photo emission spectroscopy, the authors propose the formation of a mixed Cu-

Ce-O oxide at the interface. The reduction of the cerium atoms observed on the photo emission spectra of ceria systems with copper is also confirmed by the calculations, which showed that the reduction was caused by the presence of copper. The metallic states found out in the experiment were confirmed by the presented calculations as well, since in all cases the cerium states crossed the Fermi energy showing metallic character of the interface.

The reduction of the cerium atoms in the presence of copper was shown in the calculations and observed in the experiments. The Ce^{3+} states are supposed to be the most active sites of the catalyst [7], therefore the reduction caused by the presence of copper increase the ability of ceria to catalyse CO.

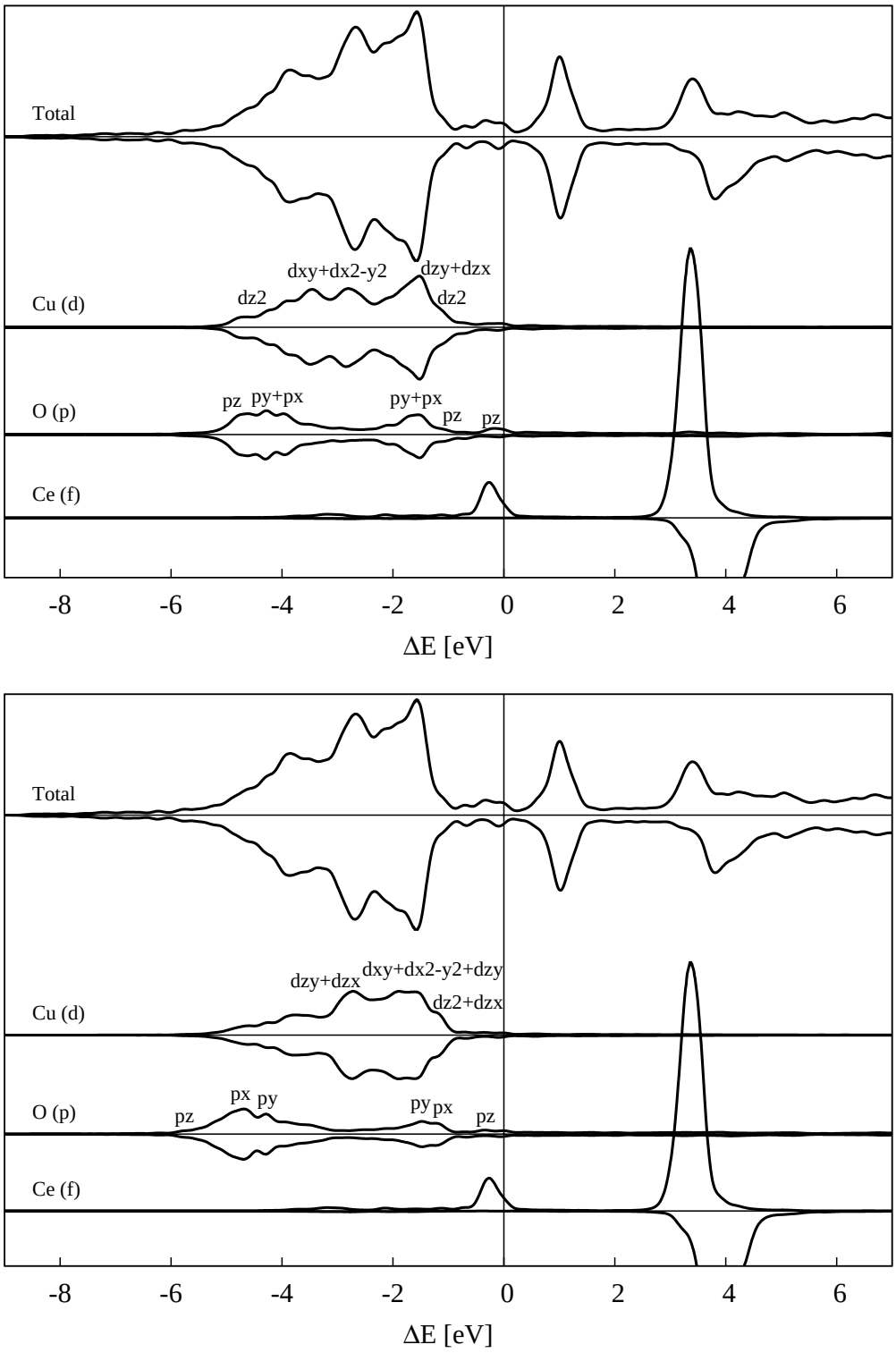

Figure 5.17: **The DOS analysis of the atoms at the interface calculated from DFT+U calculation of a system of thin copper film.** The density of states of the atoms at the *top* environment is displayed in the upper subfigure (Cu_T, O_T and Ce_T) and the density of states of the atoms from the *bridge* environment is shown in the bottom subfigure (Cu_{SB}, O_B and Ce_H).

Chapter 6

Conclusions

In the present work we studied the Cu/CeO_2 systems with the goal of determining some key structural and electronic properties controlling the catalytic activity. In particular we focused on three model systems, summarised in Fig. 1.1, by which we captured *i*) the bulk and surfaces of copper and ceria, *ii*) the atomic contact formed by Cu adatoms supported by ceria and *iii*) the $Cu(111)/CeO_2(111)$ interface.

First we calculated bulk and surface properties of the individual components in the system. We concentrated on finding the sufficient computational parameters to achieve convergent results, which we used to calculate the lattice parameter, bulk modulus, surface energies and relaxations of both copper and ceria. This was the subject of the third Chapter of the thesis.

In the fourth Chapter we explored the bonding of a small copper cluster composed of one copper adatom deposited on reduced and stoichiometric oxygen-terminated ceria surfaces. We found two possible adsorption sites on the stoichiometric surface, the adsorption site on top on surface oxygen atom and the bridge between two surface oxygen atoms. The bridge adsorption site was found most favorable, but with similar bonding properties to the less favorable top adsorption site. The character of the bonding was predicted to be partly ionic (from the charge transfer observed from the copper adatom to ceria) and partly covalent (from the shape and position of DOS peaks). In both cases the observed charge transfer caused oxidation of the copper adatom and most importantly reduction of cerium ion in the surface ceria trilayer.

The adsorption on the reduced ceria surface was considered above the oxygen vacancy. The bonding displayed completely different character, exhibiting charge transfer from ceria surface to the adatom. The transfer of the charge caused re-oxidation of one of the reduced cerium atoms on the reduced ceria surface. The bonding overall showed more ionic character than in the case of adsorption on unreduced ceria surface. The findings of this Chapter are in agreement with the recently reported calculations performed on the system of gold particles on ceria.

The fifth chapter dealt with more complex system, the $Cu(111)/CeO_2(111)$ interface. The interface was explored with respect to the local structure and bonding properties in the DFT and DFT+U level of theory. Concerning the local

structure at the interface, the results were similar in both types of calculations. The Cu-O bonds were observed to decrease and the Ce-O bonds to increase mostly by a shift of the surface oxygen atoms towards the copper slab. Those effect appeared stronger in the case of DFT+U calculation.

Very different bonding properties were acquired from the calculations in the DFT level of theory from the DFT+U calculations. In the case of DFT calculation, the bonding was realised by covalent Cu-Ce bonds and no reduction of cerium ions occurred. In the other case, the bonding was observed along the Cu-O bonds and the whole layer of cerium atoms close to the interface reduced. On the basis of previous studies, providing evidence that strongly correlated oxides like ceria require going beyond DFT and are correctly modeled by DFT+U methods, we conclude that the interface bonding predicted by the latter method is the most physical. This conclusion is further supported by energetic consideration and by the description of the bonding compatible with experimental observation.

The system with thicker ceria slab was explored to determine the convergence of the results for the number of ceria trilayers. It was shown that the bonding properties obtained from the thicker system were practically same as those of the thinner slab. By calculation of thin copper film on ceria surface we determined, that the effect of the interface is very local, since the reduction of the cerium ions occurred only in ceria layer most close to the interface. The bonding properties of the thin copper layer were the same as in the cases discussed before.

The most important implication of the thesis is that in the presence of copper, the surface cerium atoms reduce. We can thus predict, that either at the interface under some large copper particle deposited on ceria surface or at the interface between a thin copper layer supported by ceria, the whole area of ceria will be reduced. The cerium reduction is very important component of the catalytic ability of ceria based catalysts. By predicting the reduction of cerium ions in the presence of copper, we assume, that the Cu/CeO_2 systems will have important applications in the catalytic technology.

Appendix A

CD-ROM

The CD-ROM attached to the thesis contains the thesis in pdf format and the data calculated during the convergence tests in Chapter **3**. The data are divided to the files, the file cu_data contains the results of the convergence tests performed for copper, while the file ceo2_data contains the results of the convergence tests performed for ceria. The program in C language is added for creating files plottable by gnuplot. The program can be compiled on linux distributions by command "gcc -lm". The outputs created by the program are of two types, the first is the output for plotting 2D graphs which is able to plot the total energy, bulk modulus or lattice parameter as a function of k-point mesh, E_{rho}^{cut} or E_{wfc}^{cut}, while the second creates output for 3D graphs of total energy, bulk modulus and lattice parameter as the function of two from the three computational parameters (k-point mesh, E_{rho}^{cut} and E_{wfc}^{cut}).

Bibliography

[1] Xiao, W., Guo, Q., and Wang, E. G. (2003): Transformation of $CeO_2(111)$ to $Ce_2O_3(0001)$ films. *Chem. Phys. Let.*, **368**, 527–531.

[2] Mullins, D. R., Overbury, S. H., and Huntley, D. R. (1998): Electron spectroscopy of single crystal and polycrystalline cerium oxide surfaces. *Surf. Sci.*, **409**, 307.

[3] Schierbaum, K. (1998): Ordered ultra-thin cerium oxide overlayers on Pt(111) single crystal surfaces studied by LEED and XPS. *Surf. Sci.*, **399**, 29.

[4] Berner, U. and Schierbaum, K. (2002): Cerium oxides and cerium-platinum surface alloys on Pt(111) single-crystal surfaces studied by scanning tunneling microscopy. *Phys. Rev. B*, **65**, 235404.

[5] Zhao, X., S. Ma, J. H., and Rodriguez, J. A. (2007): Reaction of water with Ce-Au(1 1 1) and CeO_x/Au(1 1 1) surfaces: Photoemission and STM studies. *Surf. Sci.*, **601**, 2445.

[6] Siokou, A. and Nix, R. M. (1999): Interaction of methanol with well-defined ceria surfaces: Reflection/absorption infrared spectroscopy, X-ray photoelectron spectroscopy, and temperature-programmed desorption study. *J. Phys. Chem. B*, **103**, 6984.

[7] Matolín, V., Sedláček, L., Matolínová, I., Šutara, F., Skála, T., Šmid, B., Libra, J., Nehasil, V., and Prince, K. C. (2008): Photoemission spectroscopy study of Cu/CeO_2 systems: Cu/CeO_2 nanosized catalyst and $CeO_2(111)$/Cu(111) inverse model catalyst. *J. Phys. Chem. C*, **112**, 3751–3758.

[8] Šutara, F., Cabala, M., Sedláček, L., Skála, T., Škoda, M., Matolín, V., Prince, K. C., and Cháb, V. (2008): Epitaxial growth of continuous $CeO_2(111)$ ultra-thin films on Cu(111). *Thin Solid Films*, **516**, 6120–6124.

[9] Matolín, V., Libra, J., Matolínová, I., Nehasil, V., Sedláček, L., and Šutara, F. (2007): Growth of ultra-thin cerium oxide layers on Cu(111). *Applied Surface Science*, **254**, 153–155.

[10] Shimada, K., Kobayashi, K., Narimura, T., Baltzer, P., Namatame, H., Taniguchi, M., Suemitsu, T., Sasakawa, T., and Takabatake, T. (2002): Direct observation of the Ce 4f states in the kondo semiconductor CeRhAs and

related compounds: A high-resolution resonant photoemission study. *Phys. Rev. B*, **66**, 155202.

[11] Iwasaki, T., Suga, S., Imada, S., Sekyiama, A., Matsuma, K., Kotsugi, M., An, K.-S., Muro, T., Ueda, S., and Matsushita, T. (2000): Bulk and surface electronic structures of CePdX(X=As,Sb) studied by 3d-4f resonance photoemission. *Phys. Rev. B*, **61**, 4621.

[12] Iwasaki, T., et al. (2002): High-resolution resonance photoemission study of CeMX (M=Pt, Pd; X=P, As, Sb). *Phys. Rev. B*, **65**, 195109.

[13] Witkowski, N., Bertran, F., Gourieux, T., Kierren, B., Malterre, D., and Panaccione, G. (1997): Resonant photoemission study of the 4f spectral function of cerium in Ce/Fe(100) interfaces. *Phys. Rev. B*, **56**, 12054.

[14] Kucherenko, Y., Molodtsov, S. L., Herber, M., Laubschat, C., Malterre, D., and Panaccione, G. (2002): 4f-derived electronic structure at the surface and in the bulk of α-Ce metal. *Phys. Rev. B*, **66**, 155116.

[15] Tanuma, S., Powell, C. J., and Penn, D. R. (1994): Calculations of electron inelastic mean free paths. *Surf. Interface Anal.*, **21**, 165.

[16] Hüfner, S. (2003): Photoelectron spectroscopy, principles and applications. Springer-Verlag Berlin, Heidelberg.

[17] Wang, X., Rodriguez, J. A., Hanson, J. C., Gamarra, D., Martínez-Arias, A., and Fernández-García, M. (2006): In situ studies of the active sites for the water gas shift reaction over Cu-CeO2 catalysts: Complex interaction between metallic copper and oxygen vacancies of ceria. *J. Phys. Chem. B*, **110**, 428.

[18] Rodriguez, J. A., Liu, P., Hrbek, J., Evans, J., and Pérez, M. (2007): Water gas shift reaction on Cu and Au nanoparticles supported on CeO2(111) and ZnO(000(1)over-bar): Intrinsic activity and importance of support interactions. *Angew. Chem. Int. Ed.*, **46**, 1329.

[19] Skorodumova, N. V., Simak, S. I., Lundqvist, B. I., Abrikosov, I. A., and Johansson, B. (2002): Quantum origin of the oxygen storage capability of ceria. *Phys. Rev. Let.*, **89**, 166601.

[20] Skorodumova, N. V., Ahuja, R., Simak, S. I., Abrikosov, I. A., Johansson, B., and Lundquist, B. I. (2001): Electronic, bonding and optical properties of CeO_2 and Ce_2O_3 from first principles. *Phys. Rev. B*, **64**, 115108.

[21] Skorodumova, N. V., Baudin, M., and Hermansson, K. (2004): Surface properties of CeO_2 from first principles. *Phys. Rev. B*, **69**, 075401.

[22] Gennard, S., Corá, F., and Catlow, C. R. A. (1999): Comparison of the bulk and surface properties of ceria and zirconia by ab initio investigations. *J. Phys. Chem. B*, **103**, 10158.

[23] Yang, Z., Woo, T. K., Baudin, M., and Hermansson, K. (2004): Atomic and electronic structure of unreduced and reduced CeO_2 surfaces: A first-principles study. *Journal of Chemical Physics*, **120**, 7741.

[24] Conesa, J. C. (2003): Computer modeling of local level structures in (Ce, Zr) mixed oxide. *J. Phys. Chem. B*, **107**, 8840.

[25] Andersson, D. A., Simak, S. I., Johansson, B., Abrikosov, I. A., and Skorodumova, N. V. (2007): Modeling of CeO_2, Ce_2O_3 and CeO_{2-x} in the LDA+U formalism. *Phys. Rev. B*, **75**, 035109.

[26] Fabris, S., de Gironcoli, S., Baroni, S., Vicario, G., and Balducci, G. (2005): Taming multiple valency with density functionals: A case study of defective ceria. *Phys. Rev. B*, **71**, 041102.

[27] Koelling, D. D., Boring, A. M., and Wood, J. H. (1983): The electronic-structure of CeO_2 and PrO_2. *Solid State Commun.*, **47**, 227.

[28] Landrum, G. A., Dronskowski, R., Niewa, R., and DiSalvo, F. J. (1999): Electronic structure and bonding in cerium (nitride) compounds: Trivalent versus tetravalent cerium. *Chem. Eur. J.*, **5**, 5515.

[29] Gerward, L., Olsen, J. S., Petit, L., Vaitheeswaran, G., Kanchana, V., and Svanee, A. (2005): Bulk modulus of CeO_2 and PrO_2-an experimental and theoretical study. *Journal of Alloys and Compounds*, **400**, 56–61.

[30] Gerward, L. and Olsen, J. (1993): Powder diffraction analysis of cerium dioxide at high pressure. *Powder Diffr.*, **8**, 127.

[31] Duclos, S., Vohra, Y., Ruoff, A., Jayaraman, A., and Espinosa, G. (1988): High-pressure x-ray diffraction study of CeO_2 to 70 GPa and pressure-induced phase transformation from the fluorite structure. *Phys. Rev. B*, **38**, 7755.

[32] Hill, S. and Catlow, C. (1993): A Hartree-Fock periodic study of bulk ceria. *J. Phys. Chem. Solids*, **54**, 411.

[33] Perdew, J. P., Chevary, J. A., Vosko, S. H., Jackson, K. A., Pederson, M. R., Singh, D. J., and Fiolhais, C. (1992): Atoms, molecules, solids, and surfaces: Applications of the generalized gradient approximation for exchange and correlation. *Phys. Rev. B*, **46**, 6671.

[34] Nakajima, A., Yoshihara, A., and Ishigame, M. (1994): Defect-induced raman spectra in doped CeO_2. *Phys. Rev. B*, **50**, 13297.

[35] Conesa, J. C. (1995): Computer modeling of surfaces and defects on cerium dioxide. *Surface Science*, **339**, 337–352.

[36] Andrés, J. and Beltrán, A. (1994): An ab initio perturbed ion study of bulk ceria. *Chemical Physics Letters*, **221**, 249–254.

[37] Nolan, M., Grigoleit, S., Sayle, D. C., Parker, S. C., and Watson, G. W. (2005): Density functional theory studies of the structure and electronic structure of pure and defective low index surfaces of ceria. *Surface Science*, **576**, 217–229.

[38] Parker, S. C., Sayle, T. X. T., and Catlow, C. R. A. (1993): The role of oxygen vacancies on ceria surfaces in the oxidation of carbon monoxide. *Surf. Sci.*, **316**, 329.

[39] Tasker, P. W. (1979): Structure and properties of fluorite crystal surfaces. *J. Phys.*, **C6**, 488.

[40] Conesa, J. C. (1995): Computer modeling of surfaces and defects on cerium dioxide. *Surf. Sci.*, **339**, 337.

[41] Vyas, S., Grimes, R. W., Gay, D. H., and Rohl, A. L. (1998): Structure, stability and morphology of stoichiometric ceria crystallites. *J. Chem. Soc.*, **94**, 427.

[42] Baudin, M., Wojcik, M., and Hermansson, K. (2000): Dynamics, structure and energetics of the (111), (011) and (001) surfaces of ceria. *Surf. Sci.*, **468**, 51.

[43] Fabris, S., Vicario, G., Balducci, G., de Gironcoli, S., and Baroni, S. (2005): Electronic and atomistic structures of clean and reduced ceria surfaces. *J. Phys. Chem. B*, **109**, 22860–22867.

[44] Ž. Crljen, Šokčević, D., Brako, R., and P, L. (2003): DFT calculations of (111) surfaces of Au, Cu, and Pt: stability and reconstruction. *Vacuum*, **71**, 101–106.

[45] Xiong, Z., Shi, S., Ouyang, C., Lei, M., Hu, L., Ji, Y., Wang, Z., and Chen, L. (2005): Ab initio investigation of the surface properties of Cu(111) and Li diffusion in Cu thin film. *Physics Letters A*, **337**, 247–255.

[46] Doll, K. and Harrison, N. M. (2000): Chlorine adsorption on the Cu(111) surface. *Chemical Physics Letters*, **317**, 282–289.

[47] Neef, M. and Doll, K. (2006): CO adsorption on the Cu(111) surface: A density functional study. *Surface Science*, **600**, 1085–1092.

[48] Doll, K. (2001): Density functional study of the adsorption of K on the Cu(111) surface. *Eur. Phys. J. B*, **22**, 389–393.

[49] de Boer, F., Boom, R., Mattens, W., Miedema, A., and Niessen, A. (1988): Cohesion in Metals. North-Holland, Amsterdam.

[50] Doll, K. and Harrison, N. M. (2001): Theoretical study of chlorine adsorption on the Ag(111) surface. *Phys. Rev. B*, **63**, 165410.

[51] Domain, C. and Becquart, C. S. (2001): Ab initio calculations of defects in Fe and dilute Fe-Cu alloys. *Phys. Rev. B*, **65**, 024103.

[52] Bae, C. S., Freeman, D. L., Doll, J. D., Kresse, G., and Hafner, J. (2000): Energetics of hydrogen chemisorbed on Cu(110): A first principles calculations study. *J. Chem. Phys.*, **113**, 6926.

[53] Trovarelli, A. (2002): Catalysis by Ceria and Related Materials. Imperial College Press, London.

[54] Trovarelli, A. (1996): Inhomogeneous electron gas. *Catal. Rev.-Sci. Eng.*, **38**, 439.

[55] Yang, Z., an Gaixia Luo, Z. L., and Hermansson, K. (2007): Oxygen vacancy formation energy at the $Pd/CeO_2(111)$ interface. *Physics Letters A*, **369**, 132–139.

[56] Yang, Z., Lu, Z., and Luo, G. (2007): First-principles study of the $Pt/CeO_2(111)$ interface. *Physical Review B*, **76**, 075421.

[57] Zhang, C., Michaelides, A., King, D., and Jenkis, S. J. (2008): Structure of gold atoms on stoichiometric and defective ceria surfaces. *J. Chem. Phys.*, **129**, 194708.

[58] Zhang, C., Michaelides, A., King, D., and Jenkis, S. J. (2009): Anchoring sites for initial Au nucleation on CeO2(111): O vacancy versus Ce vacancy. *J. Chem. Phys.*, **113**, 6411.

[59] Farnesi, M. and Fabris, S. (submitted 2009): Reaction mechanisms for the co oxidation on Au/CeO_2 catalysts: Activity of substitutional Au3+ cations and deactivation of supported Au+ adatoms. *Journal of the American Chemical Society*.

[60] Richard, C., Catlow, A., French, S. A., Sokol, A. A., Alfredsson, M., and Bromley, S. T. (2003): Understanding the interface between oxides and metals. *Faraday Discuss*, **124**, 185–203.

[61] Jarvis, E. A. A., Christensen, A., and Carter, E. A. (2001): Weak bonding of alumina coatings on Ni(111). *Surface Science*, **487**, 55–76.

[62] Zdetsis, A. D. and Kuntz, A. B. (1985): Ab initio cluster study of Ni adsorption on alumina. *Phys. Rev. B*, **32**, 6358.

[63] Pacchioni, G. and Rosh, N. (1994): Modeling of supported metal clusters: a density functional study of CO chemisorption on Ni clusters deposited on alumina. *Surf. Sci*, **306**, 169.

[64] Finnis, M. W., Kruse, C., and Schönberger, U. (1995): Ab initio calculations of metal/ceramic interfaces: What have we learned, what can we learn? *NanoStructured Materials*, **0**, 145–155.

[65] Zhukovskii1, Y., Kotomin, E., Herschend, B., Hermansson, K., and Jacobs, P. (2001): A first-principles study of the $Ag/\alpha\text{-}Al_2O_3(0001)$ interface. *Int. J. Mol. Sci.*, **2**, 271–280.

[66] Tanaka, S., Yang, R., Kohyama, M., Sasaki, T., Matsunaga, K., and Ikuhara, Y. (2004): First-principles characterization of atomic structure of Al_2O_3(0001)/Cu nano-hetero interface. *Materials Transactions*, **45**, 1973–1977.

[67] Yang, R., Tanaka, S., and Kohyama, M. (2005): First-principles study on the tensile strength and fracture of the Al-terminated stoichiometric α-Al_2O_3(0001)/Cu(111) interface. *Journal Philosophical Magazine*, **85**, 2961–2976.

[68] Yang, R., Tanaka, S., and Kohyama, M. (2004): Chemical bonding at the Al-terminated stoichiometric α-Al_2O_3(0001)/Cu(111) interface. *Journal Philosophical Magazine Letters*, **84**, 425–434.

[69] Zhao, G. L., Smith, J. R., Raynolds, J., and Srolovitz, D. J. (1996): First-principles study of the α-Al_2O_3(0001)/Cu(111) interface. *Interface Science*, **3**, 289–302.

[70] Hashibon, A., Elsässer, C., and Rühle, M. (2007): Ab initio study of electronic densities of states at copper-alumina interfaces. *Acta Materialia*, **55**, 1657–1665.

[71] Tanaka, S., Yang, R., and Kohyama, M. (2006): First-principles study of the adhesive and mechanical properties of the O-terminated α-Al_2O_3(0001)/Cu(111) interfaces. *Journal Philosophical Magazine*, **86**, 5123–5135.

[72] Martin, R. M. (2004): Electronic Structure. Cambridge University Press, Cambridge.

[73] Giannozzi, P. Corso di Laurea in Fisica Computazionale.

[74] Hohenberg, P. and Kohn, W. (1964): Inhomogeneous electron gas. *Phys. Rev.*, **136**, B864.

[75] Kohn, W. and Sham, L. J. (1965): Self-consistent equations including exchange and correlation effects. *Phys. Rev.*, **140**, A1133.

[76] Cococcioni, M. (2002): A LDA+U study of selected iron compounds. *Diploma thesis*.

[77] Perdew, J. P., Burke, K., and Ernzherof, M. (1996): Generalized gradient approximation made simple. *Phys. Rev. Lett*, **77**, 3865.

[78] Monkhorst, H. J. and Pack, J. D. (1976): Special points for Brillouin-zone integrations. *Phys. Rev. B*, **13**, 5188.

[79] de Gironcoli, S. (1995): Lattice dynamics of metals from density-functional perturbation theory. *Phys. Rev. B*, **51**, 6773.

[80] Fu, C. L. and Ho, K. M. (1983): First-principles calculation of the equilibrium ground-state properties of transition metals: Applications to Nb and Mo. *Phys. Rev. B*, **28**, 5480.

[81] Marzari, N., Vanderbilt, D., Vita, A. D., and Payne, M. C. (1999): Thermal contraction and disordering of the Al(110) surface. *Phys. Rev. Lett.*, **82**, 3296.

[82] Methfessel, M. and Paxton, A. T. (1989): High-precision sampling for Brillouin-zone integration in metals. *Phys. Rev. B*, **40**, 3616.

[83] Vanderbilt, D. (1990): Soft self-consistent pseudopotentials in a generalized eigenvalue formalism. *Phys. Rev. B*, **41**, 7892.

[84] Fabris, S., Vicario, G., Balducci, G., de Gironcoli, S., and Baroni, S. (2005): Electronic and atomistic structures of clean and reduced ceria surfaces. *J. Phys. Chem. B*, **109**, 22860.

[85] `http://www.pwscf.org`.

[86] `http://www.xcrysden.org`.

[87] Kittel, C. (1996): Introduction to solid state physics. Wiley, New York.

[88] Wyckoff, R. W. G. (1961): Crystal Structures. Wiley-Interscience, New York.

[89] Soon, A., Todorova, M., Delley, B., and Stampfl, C. (2006): Oxygen adsorption and stability of surface oxides on Cu(111): A first-principles investigation. *Physical Review B*, **73**, 165424.

[90] Zhong, Q. and Ohuchi, F. S. (1990): Surface science studies on the Ni/Al2o3 interface. *J. Vac. Sci. Technol. A*, **8**, 2107.